

Slovak University of Technology, Bratislava

Faculty of Electrical Engineering and Information Technology
Department of Radio and Electronics

**HIGH CW POWER, PHASE AND AMPLITUDE
MODULATOR REALIZED WITH FAST
FERRITE PHASE-SHIFTERS**

Dissertation thesis

Ing. Daniel Valúch

Scientific discipline: 26-13-9 Electronics

Project supervisor: Dipl. Phys. Joachim Tückmantel
Educational supervisor: Doc. Ing. Peter Hajach, PhD.

CERN, Geneva, Switzerland, September 2004

Annotation:

Superconducting cavity resonators are suffering from detuning effects caused by high internal electromagnetic fields (Lorentz force detuning). For classical resonators working with continuous wave signals, this detuning is static and compensated by the slow mechanical tuning system. However, pulsing of superconducting cavities, an operational mode only recently considered, results in dynamic detuning effects. New ways to handle this effect have to be found and worked out.

A way to supply several superconducting cavities in the particle accelerator by one large transmitter while keeping the possibility of controlling the field in each individual cavity is shown. By introducing a fast phase and amplitude modulator into each cavity feeder line, the individual deviations of each cavity with respect to the average can be compensated in order to equalize their behaviour for the main control loop, which will compensate the global detuning of all cavities.

Several types of phase and amplitude modulators suitable for high power RF application, as well as different types of the fast variable phase-shifters for use in the modulator are analysed. The results of the work are foreseen to be applied in the field of particle accelerators but are certainly also interesting for other high power RF domains e.g. tuning devices for industrial microwave heating, plasma applications or nuclear fusion reactors.

I would like to give my sincere thanks

- *To my CERN supervisor Joachim Tückmantel for his excellent guidance in the field of accelerator RF technology and the very valuable ideas that he proposed during my doctoral studies at CERN*
- *To my university supervisor Peter Hajach for the excellent management of all university related issues during my doctoral studies*
- *To my friend Oliver Holme for his kindness and patience with the language consultations and corrections*
- *To Carsten Weil and the AFT company for valuable consultations and collaboration during the development of the phase-shifter devices*
- *To all members of the AB-RF group who have helped me with my work*

Contents

1. Introduction	1
2. Particle accelerator technology	3
3. Accelerator related RF systems.....	6
3.1 A resonant circuit as an accelerating structure.....	6
3.2 Ferrite loaded accelerating cavities	9
3.3 Electromagnetic resonator as an accelerating structure	10
3.4 The rectangular resonant cavity	10
3.5 The cylindrical resonant cavity	14
3.6 Excitation of the cavity resonators	16
3.7 “R/Q” ...a figure of merit for the cavity resonators.....	18
4. Current state of the problem.....	21
4.1 Operation of superconducting cavities in pulsed mode	21
4.2 Small perturbation theory	23
4.3 Cavity shape and volume perturbations, Slater’s theorem.....	24
4.4 Accelerator RF system topologies	27
4.5 Proposal of the RF system of the SPL accelerator	29
4.6 A transmission controlling device – the phase and amplitude modulator	30
5. Detailed objectives for this work	33
6. Phase and amplitude modulators.....	35
6.1 Definition of components.....	35
6.1.1 Quadrature (90°) hybrid	35
6.1.2 The 180° hybrid.....	37
6.1.3 Phase shifters.....	38
6.1.4 Loads	39
6.2. Phase and amplitude modulator using a single 3dB hybrid	40
6.2.1 Modulator with single Magic Tee working with an arbitrary load	40
6.2.2 Modulator with a single Magic Tee working with a matched load.....	42
6.2.3 Operation of the modulator with $\varphi_1=\varphi_2$	44
6.2.4 Modulator with a single quadrature hybrid working into an arbitrary load.....	44

6.2.5	Modulator with a single quadrature hybrid working with matched load	46
6.2.6	Operation of the modulator with $\varphi_1=\varphi_2$	47
6.3.	Phase and amplitude modulator using two 3dB hybrids	48
6.3.1	Modulator with two Magic Tees working into an arbitrary load	49
6.3.2	Modulator with two quadrature hybrids working into an arbitrary load.....	51
6.4	Transmission controlling capabilities	52
6.5	Summary of the analysed modulators	54
7.	High frequency and microwave phase shifting devices	56
7.1	Introduction to the phase-shifters and basic terms	56
7.2	Ferrite phase-shifters	58
8.	Coaxial ferrite phase-shifter working above ferrite's gyromagnetic resonance	63
8.1	Strip transmission lines	63
8.2	Impedance of the general transmission line	64
8.3	Impedance of the ideal strip-line transmission line.....	65
8.4	Impedance of the shielded strip-line (rectangular coaxial line).....	66
8.5	Impedance of the ferrite loaded strip-line	67
8.6	Externally controlled, variable impedance ferrite loaded strip-line.....	69
8.7	Reflection coefficient of the shorted line connected to an unmatched port – coaxial phase-shifter type one.....	74
8.7.1	Definition of the terms	74
8.7.2	Analysis of the shorted line connected to an unmatched port.....	76
8.7.3	Influence of the transmission line impedance and length on the $\Delta\varphi$	79
8.7.4.	Influence of the port impedance on the $\Delta\varphi$	80
8.7.5	Influence of the frequency to the $\Delta\varphi$	81
8.7.6	Voltage distribution along the phase-shifting structure	82
8.8	Reflection coefficient of the two serially connected transmission lines with an unmatched port – coaxial phase-shifter type two	84
8.9	Ferrite loaded transmission line in the transmission mode – coaxial phase-shifter type three.....	88
8.9.1	Impedance mismatch of the transmission type phase-shifter.....	89
8.10	Thermal load of the phase-shifting structure	91
9.	Phase tuning speed, the CERN high power, fast ferrite phase-shifter	94
9.1	Phase tuning speed	94
9.2	Power requirements for phase tuning.....	98
9.3	Technical specifications of the CERN fast ferrite phase-shifter	100

10. First results with the phase and amplitude modulator that has been built	103
11. Conclusions and outcomes from the dissertation thesis.....	104
12. References	111
Appendices	i
A. The ferrite material parameters	ii
B. Calculated transmission line parameters for the ferrite loaded line	iv
C. The rectangular resonant cavity.....	viii
D. The cylindrical resonant cavity	x
E. Photos of the phase-shifter that has been built	xiv
F. Photos of the phase and power modulator that has been built.....	xvi
G. Measured transmission controlling capabilities	xviii

Used symbols

+	Forward propagation
–	Backward (reflected) propagation
a	Acceleration scalar (m.s^{-2})
a	Transmission line dimension (m)
a	Acceleration vector (m.s^{-2})
α	Attenuation constant (Np/m)
β	Relativistic factor (v/c)
β	Phase constant (rad/m)
b	Transmission line dimension (m)
B	Vector of the magnetic induction (T)
B	Scalar value of the magnetic induction (T)*
β_{mnp}	Propagation constant for the m,n,p mode
C	Capacity (F)
C_0	Distributed capacity of the transmission line (F/m)
c	Speed of light (m.s^{-1})
d	Distance (m), or waveguide mode index
$\Delta\phi$, DP	Differential phase-shift ($^\circ$)
E	Vector of the intensity of the electric field (V/m)
e^-	Symbol of the electron
ϵ	Permittivity (F.m^{-1})
E_0	Magnitude of the electric field vector (V/m)
ϵ_r	Relative permittivity (F.m^{-1})
E_x, E_y, E_z	Components of the electric field vector (rect. coordinate system) (V/m)
Φ	Reflection coefficient of the reflective type of phase-shifter (–)
Φ	Transmission coefficient of the transmission type of phase-shifter (–)
F	Magnitude of the reflection/transmission coefficient Φ (–)

* When working with lower field inductions, unit Tesla becomes uncomfortable. Hence the older unit Gauss is often used in the industry. $1 \text{ T} = 10.000 \text{ Gauss}$

φ	Phase of the reflection/transmission coefficient Φ ($^{\circ}$)
\mathbf{F}_E	Electric component of the Lorentz force (N)
\mathbf{F}_L	Vector of the Lorentz force (N)
\mathbf{F}_M	Magnetic component of the Lorentz force (N)
FM	Figure of merit for the phase-shifter devices ($^{\circ}/\text{dB}$)
f	Frequency (Hz)
f_{mnp}	Resonant frequency of the m,n,p-th mode (Hz)
Γ	Voltage reflection coefficient (–)
G	Magnitude of the voltage reflection coefficient Γ (–)
G	Distributed conductance of the transmission line (S/m)
γ	Phase of the voltage reflection coefficient Γ ($^{\circ}$)
h	Strip-line center conductor height (m)
H_0	DC biasing field (A/m)
H_{RES}	Gyromagnetic resonance DC biasing field (A/m)
$\mathbf{i}, \mathbf{j}, \mathbf{k}$	Unity vectors
i	Instantaneous current (A)
k	Wave number
k_f	Thermal conductivity of the ferrite material ($\text{W}\cdot\text{m}^{-1}\cdot\text{K}^{-1}$)
k	Off-diagonal component of permeability tensor [μ]
L	Length (m)
ℓ	Length (m)
L	Inductance (H)
L_0	Distributed inductance of the transmission line (H/m)
λ	Wavelength (m);
λ_0	Wavelength in the vacuum (m)
m	Mass (kg)
m, n, p	The mode indexes in the cavity resonator
m_0	Quiescent mass (kg)
μ	Permeability ($\text{H}\cdot\text{m}^{-1}$)
μ'	Real component of permeability
μ''	Imaginary component of permeability
μ_i	Diagonal component of permeability tensor [μ]

μ_e	Scalar effective permeability
μ_r	Relative permeability
P	Electromagnetic pressure ($N.m^{-2}$)
\mathbf{p}	Momentum vector ($kg.m.s^{-1}$)
P_L	Losses in the cavity walls (W)
q	Charge of the particle (C)
\dot{q}	Source term in the equation governing energy balance ($W.m^{-3}$)
Q	Quality factor of the resonant circuit (general)
Q_0	Initial unloaded quality of the resonant circuit
Q_{ext}	Quality factor determined only by an external load of resonant circuit
Q_L	Quality factor of the loaded resonant circuit
r	Radius (m)
R	Resistance (Ohm)
R	Distributed resistance of the transmission line (Ohm/m)
r, ϕ, z	Coordinates in the cylindric coordinate system
R/Q	Cavity geometry parameter
R_s	RF surface resistance of the conductor
R_s	Shunt resistance of parallel resonant circuit (Ohm)
S_{ij}	ij -th component of the scattering matrix
σ	Conductivity of the material ($S.m^{-1}$)
σ	Normalized ferrite biasing field (-)
t	Time (s)
Θ	Angle ($^\circ$)
U	Energy (J)
v	Velocity scalar ($m.s^{-1}$)
v	Instantaneous voltage (V)
\mathbf{v}	Velocity vector ($m.s^{-1}$)
V	Voltage (V)
V	Volume (m^3)
V^+	Voltage of the forward wave (V)
V^-	Voltage of the reflected wave (V)
w	Strip line central conductor width (m)
ω	Angular frequency ($rad.s^{-1}$)

ω_0	Resonant angular frequency (rad.s ⁻¹)
X	Reactance (Ohm)
Z	Complex impedance (Ohm)
Z_0, Z_{LINE}	Characteristic impedance of the transmission line (Ohm)
∇	Hamilton operator $\nabla = \frac{\partial}{\partial x} + \frac{\partial}{\partial y} + \frac{\partial}{\partial z}$

Abbreviations

Cavity	Electromagnetic cavity resonator used in particle accelerator
CERN	European Laboratory for Nuclear Research
CLIC	Compact Linear Collider
CW	Continuous wave
DP	Differential phase-shift
EM	Electromagnetic
HOM	Higher Order Mode
HV	High voltage
LEP	Large Electron Positron Collider
LHC	Large Hardron Collider
Linac	Linear accelerator
MT	Magic Tee
QH	Quadrature hybrid
RF	Radio frequency
SC	Superconducting
SPL	Superconducting Proton Linac
TCD	Transmission Controlling Device
TE	Transverse Electric
TM	Transverse Magnetic

1

Introduction

The field of particle accelerator technology has evolved remarkably over the years. Nowadays, in order to explore the deep structure of matter, more and more powerful machines have to be built. In fact, modern particle accelerators are among the biggest scientific instruments in the whole world. The field of accelerator technology draws knowledge and expertise from a wide range of scientific disciplines. These include mathematics, physics, electronics, computing, magnet technology, microwave technology, cryogenics, special materials, mechanical engineering and civil engineering, to name just a few.

RF and microwave technology is a crucial part of the particle accelerator, because the acceleration itself and a lot of other operations on the particle beam are carried out using RF fields. The present work is dedicated to the high power microwave technology used for particle acceleration. As an introduction to particle accelerator technology there is a summary of the fundamentals of microwave technology used in particle accelerators with focus on the microwave cavity resonators. Techniques to determine the fields inside cavities are given and a method to calculate the change in resonant frequency caused by a mechanical deformation of the cavity is shown.

A brief introduction to the properties and behavior of superconducting cavities is given, focusing on the Lorentz force detuning phenomenon and operation of the superconducting cavity in pulsed mode.

Nevertheless, the problem of pulsing of superconducting cavities is relatively recent and we enter a new field.

The aim of this work – especially for needs of the new linear accelerator, SPL, being studied at CERN – is to study the possibility of operating multiple superconducting cavities driven by a single transmitter, while maintaining the possibility of individual field control in each

cavity. A proposal for a device, the phase and amplitude modulator¹, which will allow such operation is given. Several possible topologies of the modulator are mathematically analysed. A mathematical analysis of different types of fast phase-shifters, part of the modulator, is given.

Lastly, one design of the phase and amplitude modulator was chosen and built in collaboration with industry. The first measured results using this device are presented.

¹ Sometimes also called “The transmission controlling device”, TCD

2

Particle accelerator technology

High energy physics research focuses on the fundamental particles and forces in the universe. These particles are the leptons, like the electron and muon, and the quarks from which the strongly interacting particles are composed (such as the protons and neutrons). Today, there are estimated to be around 10 000 particle accelerators in the world. Over half of them are used in medicine and only a few for fundamental research. For the fundamental research, extremely high collision energies are required to get enough resolution to study the interactions between the particles. Since these scientific particle accelerators and detectors are complex and very expensive devices, experiments are usually performed at the level of national or more commonly international laboratories [1].

Some of the world's biggest accelerator laboratories are:

- CERN – European Organisation for Nuclear Research, Switzerland [2]
- DESY – Deutsches Elektronen-Synchrotron, Germany [3]
- Fermilab – Fermi National Accelerator Laboratory, USA [4]
- SLAC – Stanford Linear Accelerator Center, USA [5]
- KEK – High Energy Accelerator Research Organization, Japan [6]

Example applications of accelerator technology:

Lower energies

- Medical treatment e.g. cancer therapy
- Medical imaging e.g. Positron Emission Tomography (PET)
- Synchrotron radiation sources (geology, chemistry etc.)
- Mass spectrometry
- Semiconductor industry
- Basic material research
- Surface treatment
- Sterilization

- Nuclear waste disposal

High energies

- Fundamental research on the structure of matter

For high energy physics experiments, a variety of particles with a very wide spread of energies are required. For the experiments to study new particle generation, lighter particles such as electrons or protons are used. The result of the collisions of these particles is the creation of new particles. These are observed in the particle detectors and further analyzed at a later date by the physicists. In a collision of an energetic particle with a static particle energy is lost in the kinetic energy of the created particles (due to the momentum conservation). Therefore the latest generation of high-energy machines are so-called colliders, where two counter-rotating particles are interacting. In most cases both particles have the same mass.

In the CERN's former largest accelerator LEP (Large Electron-Positron Collider), electrons and their antiparticles positrons were collided. These particles have the same mass, but inverse electric charge. This allowed the same beam tube and bending dipole magnets to be used for both beams. A similar configuration for protons and anti-protons was used in the Sp \bar{p} S machine (CERN) and Tevatron machine (Fermilab, USA).

Electrons and positrons are true elementary particles (until further notice) and their collisions are pure without debris of the target particles. However, electrons are light particles and in a circular machine emit synchrotron radiation [7]. Energy loss due to synchrotron radiation was the final limitation to the maximal achievable energy in the LEP machine. Therefore CERN's new machine, LHC (Large Hadron Collider), will use protons, allowing much higher energies reusing the same underground tunnel. The maximal achievable energy will now be limited by the bending magnetic field provided by the superconducting dipole magnets [8].

In the Sp \bar{p} S antiprotons were used as the second beam in the same beam pipe. Nevertheless the number of collisions (so called integrated luminosity) was limited by the production rate of antiprotons. Therefore in the LHC both beams are protons. This requires a double beam pipe (vacuum chambers) with opposite magnetic fields and dedicated crossing regions.

Protons are not elementary, but composed of smaller particles. Therefore at each collision a proton does not collide with a proton, but one constituent of one with one constituent of the other. These collisions create a large number of particles in which the desired reaction is

hidden. Therefore a very large number of collisions have to be recorded for statistically significant signals asking for very high luminosity.

On the other hand, for experiments studying the nuclear reactions, heavier particles and ions at lower energies are usually used.

By RF fields, it is only possible to accelerate the electrically charged particles. Most common particles used for high energy experiments and their basic properties are listed in the Table 2.1.

Particle	Electric charge *	Mass (kg)	Mass (MeV/c ²)
electron	-1	9.10×10^{-31}	0.511
positron	+1	9.10×10^{-31}	0.511
proton	+1	1.673×10^{-27}	938
anti-proton	-1	1.673×10^{-27}	938
heavy ions	very wide variety of ions		

* relative to elementary charge of 1.602×10^{-19} C

Table 2.1: Types of particles used in the high energy experiments

3

Accelerator related RF systems

In this chapter a brief introduction to particle accelerator related RF systems is given. A brief review of the parallel resonant circuit as a model for the basic accelerating structure is followed by its realisation for lower frequencies (ferrite loaded cavities) and higher frequencies (microwave cavity resonators). The excitation methods of cavity resonators are listed and basic quantities like quality factor or R/Q of the cavity resonators are introduced.

3.1 A resonant circuit as an accelerating structure

Because a large part of this work is directly related to the resonant circuits and later to superconducting resonators a brief summary from the linear circuit theory [13] will be useful. Assume a R-L-C structure as shown in Fig. 3.1. L represents the inductance (a lumped element, or its distributed equivalent in the cavity resonator), C represents the capacity (again a lumped element, or its distributed equivalent in the cavity resonator) and R represents the losses in the circuit (non-perfect inductor or capacitor, or the wall losses of the cavity resonator).

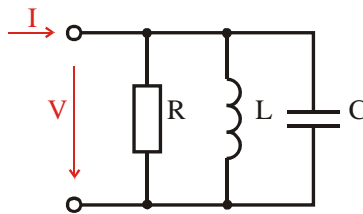


Fig. 3.1: The parallel resonant circuit

Now using the well known formulas 3.1a and 3.1b

$$X_L = j\omega L \tag{3.1a}$$

$$X_C = \frac{1}{j\omega C} \tag{3.1b}$$

we can write for the impedance of the resonant circuit:

$$\mathbf{Z}_{\text{IN}} = \frac{1}{\frac{1}{R} + \frac{1}{j\omega L} + j\omega C} \quad (3.2)$$

Resonance occurs at the frequency ω_0 where both of the reactive components have same magnitude and are compensating each other.

An important parameter specifying frequency selectivity and performance of the resonant circuit is the quality factor Q. A very general definition of the Q factor, applicable to all resonant systems is 3.3

$$Q = 2\pi \frac{\text{Total stored energy at resonant frequency}}{\text{Energy dissipated at one period of this frequency}} \quad (3.3)$$

In the case of the parallel resonant circuit, the formula 3.3 becomes

$$Q = \omega RC = \frac{R}{\omega L} \quad (3.4)$$

In the vicinity of resonance (at the angular frequency of $\omega = \omega_0 + \Delta\omega$), and using the approximation 3.5 the input impedance can be expressed in the more convenient form 3.6.

$$\frac{1}{\omega_0 + \Delta\omega} \approx \frac{1}{\omega_0} \left(1 - \frac{\Delta\omega}{\omega_0} \right) \quad (3.5)$$

$$\mathbf{Z}_{\text{IN}} = \frac{1}{\frac{1}{R} + \frac{1}{j\omega L} + j\omega C} = \frac{1}{\frac{1}{R} + j\omega_0 C + j\Delta\omega C + \frac{1}{j\omega_0 L} \left(1 - \frac{\Delta\omega}{\omega_0} \right)} \quad (3.6)$$

Since at the resonance $j\omega_0 C + \frac{1}{j\omega_0 L} = 0$, we obtain:

$$\mathbf{Z}_{\text{IN}} = \frac{\omega_0^2 RL}{\omega_0^2 L + j2R\Delta\omega} = \frac{R}{1 + j2Q \frac{\Delta\omega}{\omega_0}} \quad (3.7)$$

A plot of \mathbf{Z}_{IN} as a function of $\Delta\omega/\omega_0$ is given in Fig. 3.2. This represents a typical resonance curve. The peak value of the impedance corresponds to the value of the loss resistor and when the $|\mathbf{Z}_{\text{IN}}|$ falls to $1/\sqrt{2}$ of its maximum, its phase is $+45^\circ$ (below the resonance) or -45° (above the resonance) respectively. Later, the phase of \mathbf{Z}_{IN} is used to measure the tune state of the cavity resonator.

The two $1/\sqrt{2} R$ (or -3dB) points define the circuit bandwidth. Using 3.7 the corresponding value of $\Delta\omega$ can be found.

$$\Delta\omega = \frac{\omega_0}{2Q} \quad (3.8)$$

The fractional bandwidth between the $1/\sqrt{2} R$ points is double this value. Hence for the quality of the resonant circuit we can write

$$Q_0 = \frac{\omega_0}{2\Delta\omega} = \frac{\omega_0}{\text{BW}} \quad (3.9)$$

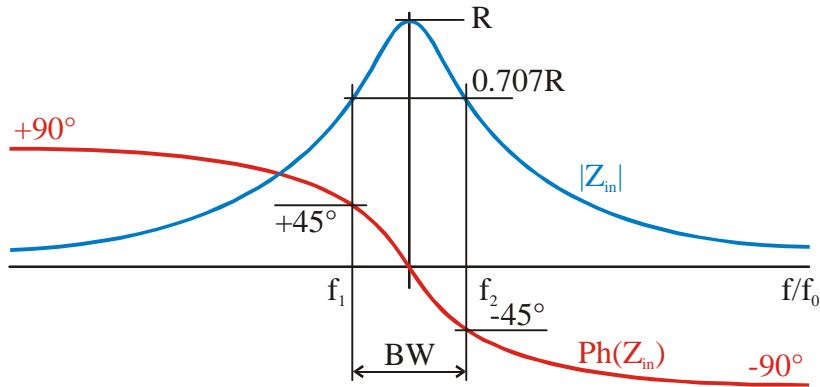


Fig. 3.2: Typical resonance curve

All previous calculations and formulas are valid only for the “stand-alone” resonant circuit. The Q factor obtained from 3.4 is then called the “unloaded Q ”, Q_0 . When such a circuit is coupled with some external circuit, a part of the energy is absorbed there. This additional loading effect is represented by an additional resistor R_L connected in parallel with the “main” loss resistor R . As the total loading resistance of the resonant circuit is lower, the Q factor will be lower as well. The new factor, the “loaded Q ” is defined as

$$Q_L = \frac{R R_L}{R + R_L} \omega L \quad (3.10)$$

An additional Q factor – the external Q_{EXT} – is defined to be the Q if the resonant circuit is lossless and only the loading by the external load is present ($R=0$).

$$Q_{\text{EXT}} = \frac{R_L}{\omega L} \quad (3.11)$$

When using these definitions we can write:

$$\frac{1}{Q_L} = \frac{1}{Q_{EXT}} + \frac{1}{Q_0} \quad (3.12)$$

The Q_{EXT} is usually used when talking about superconducting resonators, when Q_0 of the resonator is very high (easily more than 10^9), and Q of such a system is essentially determined by the coupling factor to the driver.

3.2 Ferrite loaded accelerating cavities

In the smaller accelerators, where the RF frequency is relatively low (from ones to few tens of megahertz), the resonant circuits are formed out of lumped elements. Two parallel plates in the vacuum chamber form the capacitor. The inductor is usually an external lumped element. In order to maintain high performance and a high Q resonant circuit, it must be a high quality and high linearity type.

In the case of non-relativistic particle acceleration (velocity is still increasing during the acceleration), the frequency of the accelerating field must be adapted to the revolution frequency of the beam. This brings about a requirement for a tunable resonant circuit. Since capacitor plates are a fixed part of the vacuum chamber, the only convenient way to change the resonant frequency of the accelerating resonator by significant amounts is to tune its inductance.

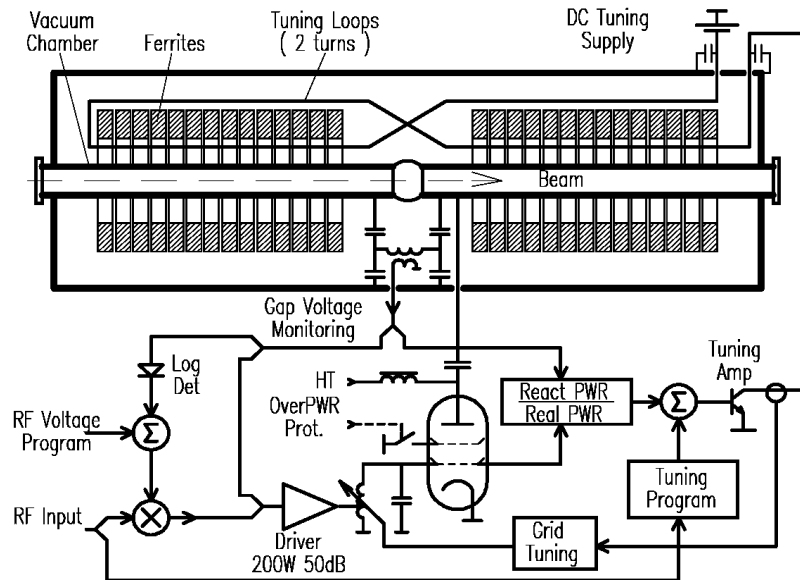


Fig. 3.3: Ferrite loaded cavity – the low frequency accelerating structure

One example of a practically realized system is shown in Fig. 3.3 [14]. The operating frequency of this particular system is from 1.9 to 3.9MHz and a quality factor of the resonator

90-190. With RF power of 20kW, a nominal gap voltage of 10kV can be achieved. The ferrite tuning currents have values up to 2800A.

3.3 Electromagnetic resonator as an accelerating structure

When the particles become relativistic, their speed is very close to the speed of light, and increases only little with energy. Then the frequency of the accelerating field becomes practically constant. Resonators operating at constant frequency are easier to build and they can be optimized to obtain very high values of the Q-factor. Operating frequency is usually lying in the range of 50MHz to 3000MHz, where classical cavity resonators become reasonable in dimensions to build.

A cavity can be considered as a volume enclosed by the conducting surface, within which an electromagnetic field can be excited [37]. The finite conductivity walls cause the power losses and thus are equivalent to the parallel loss resistance. The field in the cavity can be excited by means of probes (E fields), loops (H fields), or might be coupled to a waveguides or other cavities using apertures in the wall (see chapter 3.6). The next paragraphs provide a brief introduction to the cavity issues, such as the field solutions, the coupling techniques and some useful techniques.

3.4 The rectangular resonant cavity

The field solutions are derived from waveguide theory [38]. Assume a rectangular cavity of width a , height b and length d shown in Fig. 3.4. It might be considered as a section of the rectangular waveguide short-circuited at the positions $z=0$ and $z=d$. Since both TE and TM modes exist in the rectangular waveguide, we can expect the TE and TM modes in the rectangular resonator as well. However, the designation of TM and TE modes in the resonator is not unique, because we are free to choose x , y or z as the direction of propagation (there is no unique longitudinal direction of propagation). For example a TE mode with respect to the z axis could be a TM mode with respect to the y axis. For the purpose the z axis is chosen as a reference to the direction of propagation.

In contrast to the waveguide, the existence of the conducting walls at $z=0$ and $z=d$ positions cause multiple reflections and builds a standing wave inside the structure. To describe the field inside the resonator a three-symbol subscript in form of “mnp” for the TE and TM modes is needed.

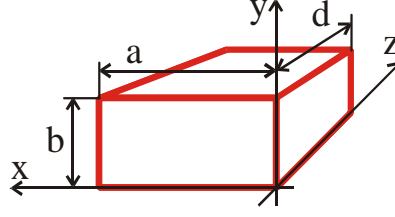


Fig. 3.4: Rectangular resonant cavity (the coordinate system)

Calculation of the field components can be done by various mathematical techniques, and can be found easily in the literature (e.g. [15]). The field components of the resonant modes are listed in the Appendix C.

Resonators for particle acceleration purposes are designed such, to operate at the lowest order mode possible. In the case when only the fundamental TM_{110} mode is excited in the cavity (see Fig. 3.5), and the beam is passing the cavity through its electrical center ($x=a/2$ and $y=b/2$; in an ideal case it is also the geometric center), the fields seen by the beam are:

$$E_z(a/2, b/2, z) = E_0 \quad (3.13)$$

$$H_x(a/2, b/2, z) = 0 \quad (3.14)$$

$$H_y(a/2, b/2, z) = 0 \quad (3.15)$$

As we can see from the 3.13, 3.14 and 3.15, the beam is only accelerated by the electric field and its trajectory is not changed by any of the magnetic or electric fields. However, this is not valid for the higher order modes (HOM) anymore. The electric and magnetic field components are not zero in the center of the cavity so higher order modes disturb the beam and can lead to beam instabilities.

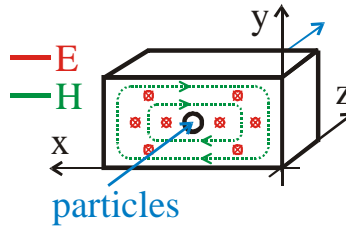


Fig. 3.5: Acceleration of the beam by the rectangular cavity, TM_{110} mode

The shape of the resonant cavities is optimized to shift the frequencies of the higher order modes as far as possible from the beam spectral lines. To prevent building up the high HOM fields inside the cavity, HOM dampers are used [39]. HOM dampers are realised by sophisticated types of E or H field couplers, to couple as much HOM power as possible, but not to couple to the fundamental mode.

Photographs of the 50MHz, (almost) rectangular cavity, built in the Paul Scherrer Institut (PSI, Switzerland) are shown in Fig. 3.6. The cavities are normal conducting, tuned to the resonant frequency of 50.1MHz, nominal input power of 500kW produces an accelerating gradient of 1MV. The Q factor obtained by the copper version is about 45.000.

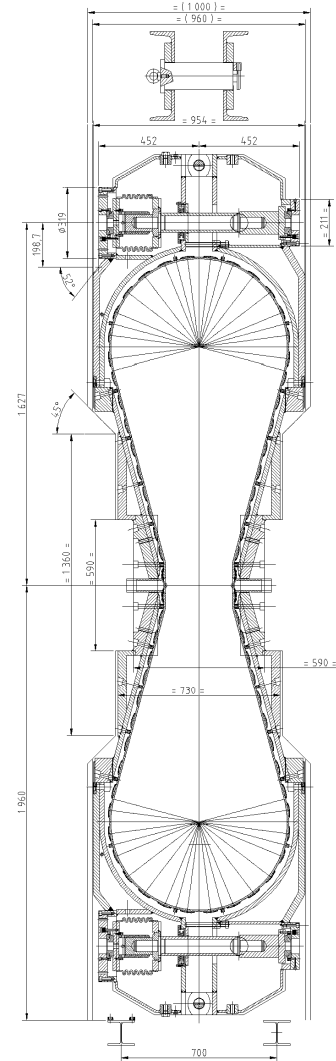
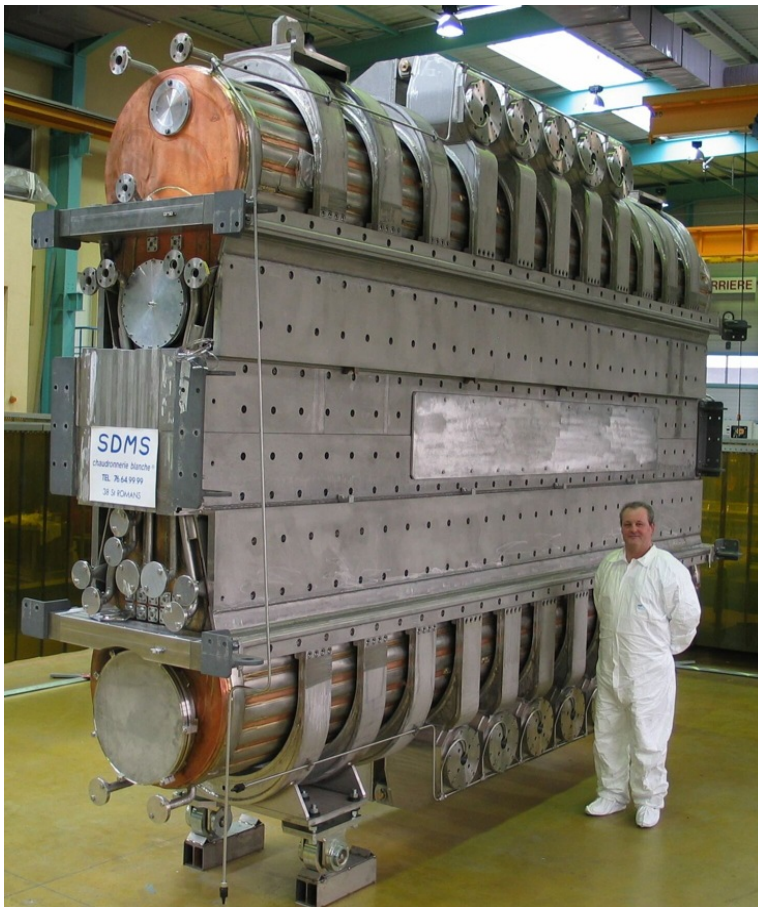


Fig. 3.6: 50MHz normal conducting cavity (courtesy of PSI Switzerland)

Quality of the rectangular resonator

As it was mentioned in section 3.1, the general formula 3.3 is valid for any resonant structure, therefore the calculation of the resonator quality factor is straight forward [40]. Let the time-average stored energy at resonance be U , and the energy dissipated at one period of the resonant frequency be P_L . Further calculation will be done with respect to the fundamental mode TM_{110} .

The stored energy in the electric field of the resonator is:

$$U_E = \frac{\varepsilon_0}{4} \iiint_{\text{resonator volume}} |\vec{E}|^2 dv = \frac{\varepsilon_0}{4} \iiint_{\text{resonator volume}} |E_z|^2 dv \quad (3.16)$$

and for the stored energy in the magnetic field:

$$U_M = \frac{\mu_0}{4} \iiint_{\text{resonator volume}} |\vec{H}|^2 dv = \frac{\mu_0}{4} \iiint_{\text{resonator volume}} \left(|H_x|^2 + |H_y|^2 \right) dv \quad (3.17)$$

At resonance, the total stored energy is $U=U_M=U_E$. To find the total losses, dielectric losses in the resonator are neglected (cavity is under high vacuum) and losses caused by the finite conductivity of the cavity walls are evaluated. For small losses, the surface currents are essentially those associated with the loss-free field solutions, so we can write:

$$P_L = \oint_{\text{walls surface}} \frac{1}{2} |J_s|^2 R_s ds = \oint_{\text{walls surface}} \frac{1}{2} |H_t|^2 R_s ds \quad (3.18)$$

General formula for the quality factor calculation is:

$$Q = \frac{\omega_0 U}{P_L} \quad (3.19)$$

By plugging the results of the 3.16 (or 3.17) and 3.18 in general formula 3.19, the quality factor for any mode can be calculated.

R_s in (3.18) is the surface resistance of the wall conductor as function of frequency due to the skin depth:

$$R_s = \sqrt{\frac{\pi f \mu_{\text{conductor}}}{\sigma_{\text{conductor}}}} \quad (3.20)$$

Usual values of the Q factor of the cavity resonators are in the order of tens of thousands for the normal conducting resonators, and of the orders of 10^9 for the superconducting resonators.

3.5 The cylindrical resonant cavity

In the same way, as we have constructed the rectangular cavity out of the rectangular waveguide the cylindrical cavity can be constructed out of a cylindrical waveguide. The ends of the cylindrical waveguide are shorted by conductive plates at positions $z=0$ and $z=d$. All principles explained in the section about the rectangular cavity are applicable for the cylindrical cavity as well.

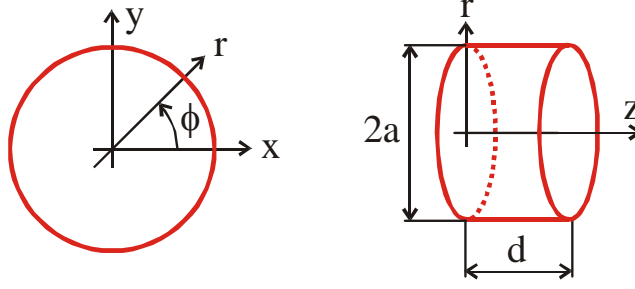


Fig. 3.7: Cylindrical resonant cavity (the coordinate system)

More detailed description of the cavity resonant modes is given the Appendix D. The TM_{010} mode has very favorable properties for the particle acceleration purposes. Consequently in accelerators this mode is nearly exclusively used. In a pure pill-box cavity², there are only two field components of the TM_{010} mode inside the cavity [41]:

$$E_z = E_0 J_0\left(\frac{2.405}{a} r\right) \quad (3.21)$$

$$H_\phi = -j \frac{E_0}{Z_0} J_1\left(\frac{2.405}{a} r\right) \quad (3.22)$$

A cavity with rounded shape has an E_r component in the TM_{010} like mode. Since mode number $l=0$, the resonant frequency is independent of the longitudinal dimensions of the resonant cavity. It is not possible to tune such a cylindrical resonator by changing its length³. A cavity operating with the TM_{010} mode can be tuned by introducing an obstacle into the cavity (small conductive or dielectric entity). This technique is called small perturbation theory (see section 4.3).

² Pill-box cavity name for the exact cylindrically shaped cavity (rectangular longitudinal cross-section).

³ Real cylindrical accelerating cavities do not have a rectangular pill-box cross-section, but are rounded. Resonant frequency is then sensitive to the longitudinal dimension of the cavity.

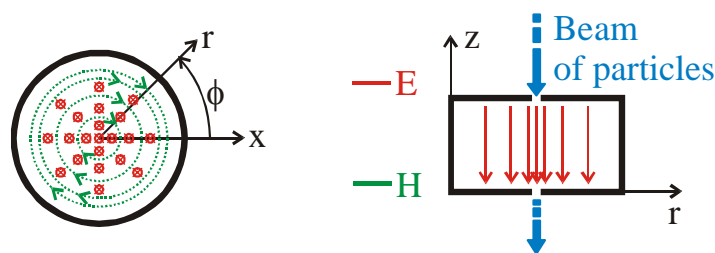


Fig. 3.8: Acceleration in the cylindrical cavity

Quality of the cylindric cavity resonator

The quality of the cylindrical resonator can be calculated in the same way as for the rectangular resonator. Comparison of the quality factors for different modes is in figure D.2. An example of its value for the TM_{010} mode inside the vacuum filled cavity is given by the formula 3.23.

$$Q_{TM_{010}} = \frac{Z_0}{2R_s} \frac{P_{01}}{1 + \frac{a}{d}} \quad (3.23)$$

The quality factor of the standard normal conducting copper resonators, operating below 1GHz is in range of 10.000-50.000 [42].

A photo of the 352MHz, four cell, superconducting cavity used in the CERN's LEP II accelerator is shown in Fig. 3.9. With 125kW of input power, an accelerating voltage of 10MV was achieved. A photo of the one cell of the 30GHz normal conducting, cavity, which will be used in the future CLIC accelerator in CERN is shown in Fig. 3.10.

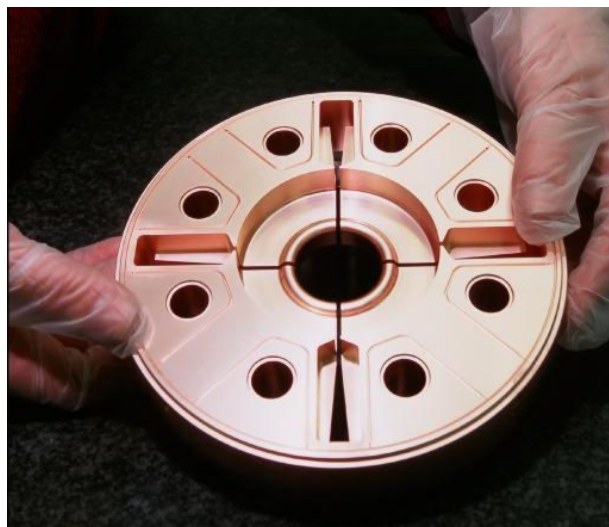


Fig. 3.9: The LEP superconducting cavity Fig. 3.10: The CLIC normal conducting cavity

3.6 Excitation of the cavity resonators

There are several methods for coupling the cavity to the external circuits. The coupling structure must excite the electric and/or magnetic component of the desired resonant mode. Four types of excitations are common:

- a. Magnetic (current) loops
- b. Electric field probes – antennas
- c. Coupling apertures
- d. Excitation by a beam of charged particles

Example of structures a,b and c are shown in Fig. 3.11.

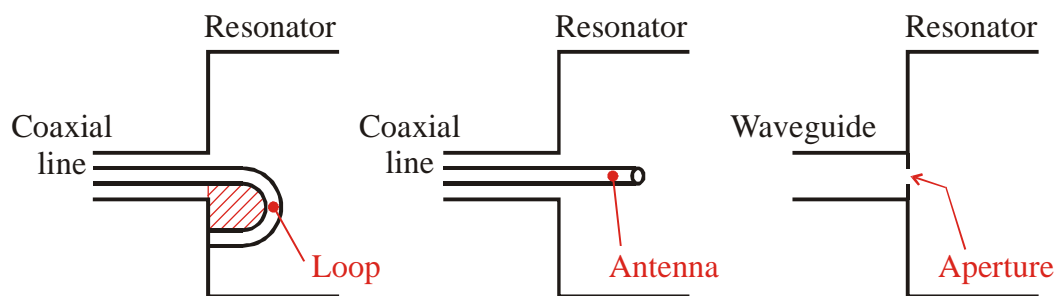


Fig. 3.11: Cavity excitation structures

Magnetic loop coupling

A loop coupling is used when the magnetic component of the resonant mode has to be excited [43]. A current flowing in the conductive loop generates the magnetic field perpendicular to the loop area. The loop then couples to all possible modes, which have a magnetic field component crossing the loop and are fulfilling the resonant conditions (frequency etc.). The excitation may be optimized to excite the mode with maximal efficiency – then the loop must be placed in the maximum of magnetic field of the desired mode. Excitation might be chosen in such a way to exclude coupling to a family of particular modes. This is achieved when the loop is placed parallel to the magnetic field of modes to be excluded. This principle is used for the higher order modes couplers in the particle accelerator cavities. HOM couplers are optimized to couple as much to the HOMs as possible, while keeping coupling to the main resonant mode as low as possible.

Electric field coupling

An antenna, looking into the cavity, is coupling to all modes which have electric field at the coupler location. As with the magnetic coupling, maximum excitation can be achieved if the

antenna is located in the maximum of the electric field of the desired mode. Modes having electric field zeroes at the probe location will not be excited.

Loop and antenna couplers are used mainly to couple to coaxial or strip-line transmission lines [17].

Aperture coupling

The cavity might be coupled to the source by slots, irises, or any arbitrary openings in the cavity walls [44]. Aperture coupling is mainly used to couple the cavity to waveguide transmission lines, or to other cavities. The fields in the cavity and in the transmission line must have the same direction. For calculation of the coupling coefficient, small apertures may be described in terms of their equivalent electric or magnetic dipoles. The positioning of the openings again allows excitation of selected modes inside the cavity.

Beam of charged particles

Charged particles traveling inside a closed metallic structure – as beam pipe, or cavity – carry a corresponding image charge on the surrounding metallic structure with them. Therefore all diameter changes of the beam pipe (e.g. as a cavity) deviate the image current which in turn, excite electromagnetic fields. These can be expressed as excited modes. The coupling between the particle beam and the cavity is used in electron tubes to amplify or generate the powerful microwave signals e.g. like in klystrons or magnetrons [18].

Generally, for high-power applications where a fixed position of the coupler is sufficient, it is simpler to use loop couplers. For the applications where a modification of coupling strength is necessary, the electric field antenna couplers are more convenient to use. Also if the magnetic field is comparatively low – as on the cut-off tubes of superconducting cavities – antenna couplers are preferred. An example of the tunable antenna coupler for CERN's superconducting LHC cavities is shown in figure 0.14. Its operating frequency is 400.8MHz, forward power of 300kW, coupling is variable to achieve Q_{ext} in range from 20.000 to 200.000 [45].

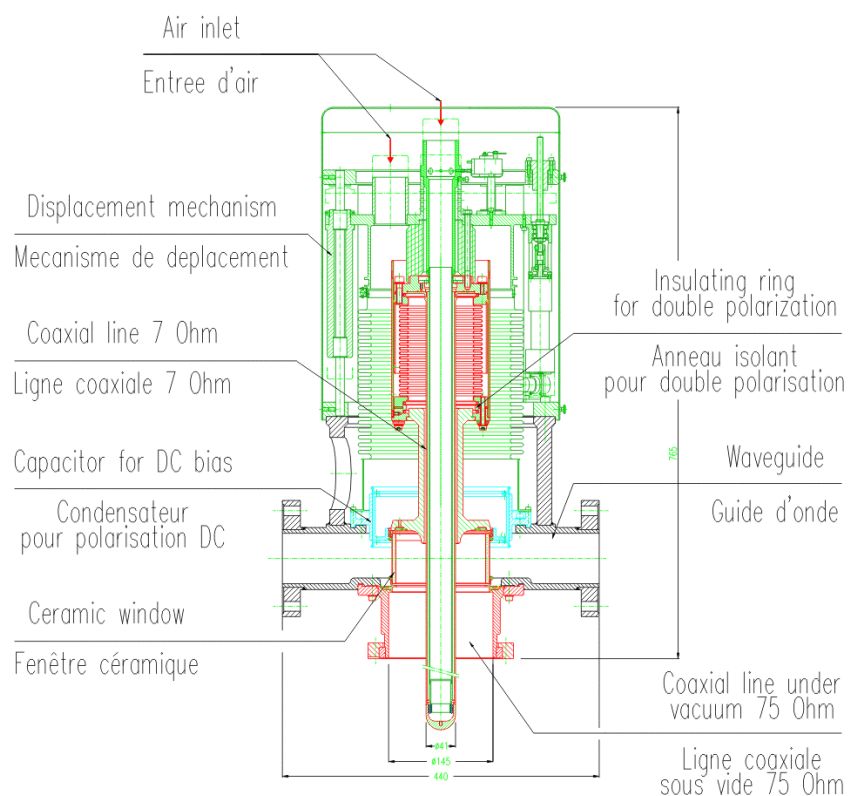


Fig. 3.12: The CERN's LHC superconducting cavity coupler (courtesy of CERN)

3.7 “R/Q” ...a figure of merit for the cavity resonators

Resonant cavities, used in the particle accelerator technology are optimized to achieve a high accelerating voltage while keeping wall losses P_L at the lowest possible level. Therefore a first figure of merit was defined to characterize the cavity performance – the so-called shunt impedance R_s ⁴

$$R_s = \frac{1}{2} \frac{V^2}{P_L} \quad (3.24)$$

Since P_L is proportional to the square of the excitation voltage, the shunt impedance R_s is independent of the field inside the cavity. However, when changing the cavity material a geometrically identical cavity will have different losses P_L .

Together with the quality factor Q of any resonator, defined as

⁴ Historically the factor 1/2 was not included but to be better consistent with the circuit theory, the definition was changed and this factor is generally included nowadays. However, older publications or conservative authors may still apply the initial definition.

$$Q = \frac{\omega U_{st}}{P_L} \quad (3.25)$$

the ratio of R_s and Q defines a new figure of merit (R/Q), pronounced “R over Q”.

$$\left(\frac{R}{Q}\right) = \frac{1}{2} \frac{V^2}{P_L Q} = \frac{1}{2} \frac{V^2}{\omega U_{st}} \quad (3.26)$$

(R/Q) which is independent of the cavity material, is determined by the pure cavity geometry. This constant is very important in a more general context as shown later. (R/Q) can be calculated by computer simulation programs as MAFIA [19] or SUPERFISH [20]. These programs calculate a field map for a selected mode and from it determine the accelerating voltage and the stored energy in the cavity.

Once the calculated value of (R/Q) is known, it is the key to determine the accelerating voltage in the real cavity (measurements on built system). The Q -value of the cavity can be determined from measured bandwidth of the normal conducting cavities or of the decay time for the superconducting cavities. It is important to consider the influence of the coupler in this context and correct for its contribution. The Q value can also be calculated (as shown in chapter 3.4) if the conductivity of the cavity material is reasonably well known (which is not the case for superconducting cavities). Then a measurement of the power dissipated in the cavity (e.g. difference of incident and reflected RF power) results in the knowledge of the cavity voltage.

Even more important is the role of (R/Q) as the coupling constant between the cavity and the beam. These relations can be determined using energy conservation. If a charge q is passing through the cavity at optimum RF phase, it is accelerated and takes the energy ΔU from the cavity, which lowers its voltage by ΔV . Due to the superposition of fields, this can also be seen as an induced decelerating voltage $-\Delta V$ by the charge passing through. The charge is accelerated by the cavity voltage V but sees also the unknown fraction α of its own induced decelerating voltage. The charge then gains the energy

$$\Delta U_{charge} = q(V - \alpha \Delta V) \quad (3.27)$$

Transforming the definition of (R/Q) we have

$$U_{st} = \frac{1}{2} \frac{V^2}{\omega (R/Q)} \quad (3.28)$$

and hence the energy lost from the cavity can be expressed by

$$\Delta U_{\text{st}} = \frac{1}{2} \frac{V^2 - (V - \Delta V)^2}{\omega (R/Q)} = \frac{1}{2} \frac{2V\Delta V - \Delta V^2}{\omega (R/Q)} \quad (3.29)$$

The total energy must be conserved, so both ΔU 's must be equal yielding

$$\left(V - \frac{1}{2}\Delta V\right)\Delta V = q \omega (R/Q) (V - \alpha \Delta V) \quad (3.30)$$

This relation has to be valid for any V and ΔV which can only be true if

$$\alpha = \frac{1}{2} \quad (3.31a)$$

$$\text{and } \Delta V = q \omega (R/Q) \quad (3.31b)$$

This means that a charge passing a cavity feels half of its own induced voltage (first stated by P. Wilson [21]) and the induced voltage by a passing charge is given by (3.31b). A comparison of different cavity shapes with their respective R/Q 's is given in Table 3.1.

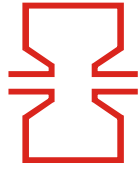
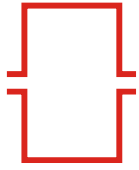
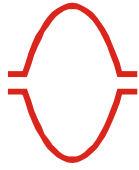
			
R/Q	higher	middle	lower
R_s	highest	middle	lowest

Table 3.1: Comparison of cavity geometries

4

Current state of the problem

Chapter 4 gives an introduction to the problem of the detuning of a superconducting resonator due to its internal electromagnetic fields, using the small perturbation theory and Slater's theorem. It introduces the problems related with the pulsed operation of the SC cavities. The basic topologies of accelerator RF systems are shown and characterised with respect to the planned SPL accelerator. The transmission controlling device is proposed as a potential solution to compensate the detuning effect, maintaining control of the field in each individual cavity while keeping the cost of the whole system reasonable.

4.1 Operation of superconducting cavities in pulsed mode

In the past, when normal conducting copper cavities were used exclusively, the effects of the internal electromagnetic forces were negligible. Copper cavities are usually built out of a massive block of copper with rather thick walls [46]. The use of superconductors for building resonant cavities caused a change in the cavity technology. Compared to the classical copper cavities, superconducting cavities can have – today several ten times – higher CW field levels and have considerably lower RF losses, even when taking into account that these losses are dissipated at cryogenic temperatures. Therefore they were used in the machines in CW mode as in storage rings (e.g. CERN's LEP [27]) or constant beam machines (e.g. Jefferson Lab's CEBAF [28]).

Pulsed linacs⁵ were the exclusive domain of copper cavities where even higher field levels were obtained but only for very short pulses (micro seconds) and at very low duty cycles [47].

As the superconducting technology progressed, obtained field levels in these cavities make the construction of a superconducting linac competitive to copper one. Field levels are still lower than for pulsed copper cavities but superconducting cavities can reach these fields at much lower frequency with correspondingly larger cavities.

⁵ Linac – Linear accelerator

This considerably reduces the problems of transversal wake-fields (causing the beam break-up) and machine alignment. TESLA [29] is the first such machine, but it is not approved yet. However, the high field levels increase also the cryogenic losses considerably (losses are rising more than with square of the field). Therefore it is envisaged to run this machine not at 100% duty-cycle but in a slow pulsed mode. Beam pulses of a few milliseconds with a repetition rate of about ten of Hertz, are giving the cryogenic supply enough time to compensate the average thermal loss. Other machines tend to follow the same way, e.g. the SPL [30] at CERN.

Superconducting cavities are built from a few millimetres thick metal sheet [48] for better heat transfer between the superconducting RF surface and the liquid helium (LHe). In the case of the bulk niobium cavities, the walls of the cavity are thin also for cost reasons [49]. Therefore these cavities are much softer than classical copper cavities generally made out of solid metal blocks. Hence they are much more sensitive to the Lorentz force detuning⁶. Furthermore, since the system bandwidth of the superconducting cavities is generally smaller in comparison to pulsed copper cavities, the effect of the same absolute detuning appears as a larger change in phase and amplitude of the cavity field. Therefore the Lorentz detuning phenomenon has been studied intensively at many laboratories, especially those of the TESLA collaboration [50]. An example of cavity detuning when driven by the pulsed RF signal is shown in Fig. 4.1.

Using Slater's theorem (see section 4.3), which gives the change in frequency due to small perturbation in the cavity shape, and the mechanical parameters of the cavity, the sensitivity to the mechanical stresses can be determined. In order to realize a stable accelerating field, both the stiffness of the cavity and the proper RF control system are needed.

⁶ Lorentz force detuning – mechanical deformation of the cavity shape caused by its internal electromagnetic fields

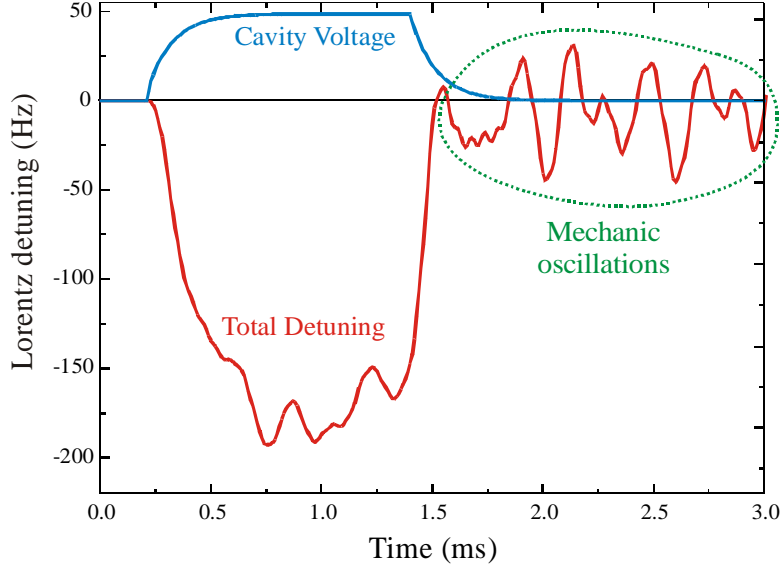


Fig. 4.1: Dynamic detuning of the cavity, when driven by pulsed RF signal (KEK Japan)

4.2 Small perturbation theory

The resonant frequency of the cavity can be varied over a small range by inserting a small perturbing object into a cavity. In some cases, the effect of such perturbation on the cavity performance can be calculated exactly, but often in real cases some level of approximations must be used. One useful technique for doing this is called the small perturbation theory.

Detailed mathematical analysis of the problem can be found in the literature (e.g. [13], [16]). To show the principle, only the initial assumptions and the final results are shown. The small perturbation theory is assuming, that electromagnetic fields inside the cavity with the small disturbing object inserted are not very different from fields without it.

Assume \mathbf{E}_0 and \mathbf{H}_0 to be original fields inside the cavity and \mathbf{E} and \mathbf{H} to be fields of the perturbed cavity. Then Maxwell's equations for the unperturbed cavity are

$$\nabla \times \mathbf{E}_0 = -j\omega_0 \mu \mathbf{H}_0 \quad (4.1)$$

$$\nabla \times \mathbf{H}_0 = j\omega_0 \varepsilon \mathbf{E}_0 \quad (4.2)$$

And for the perturbed cavity:

$$\nabla \times \mathbf{E} = -j\omega(\mu + \Delta\mu)\mathbf{H} \quad (4.3)$$

$$\nabla \times \mathbf{H} = j\omega(\varepsilon + \Delta\varepsilon)\mathbf{E} \quad (4.4)$$

where ω_0 is the resonant frequency of the original cavity and ω is the resonant frequency of the perturbed cavity (see Fig. 4.2).

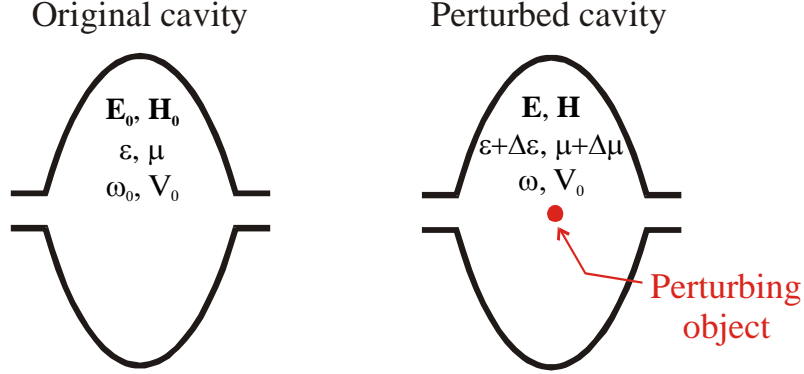


Fig. 4.2: Quantities in the unperturbed and perturbed cavity

Then following the calculations and simplifications in [15] we obtain:

$$\frac{\omega - \omega_0}{\omega} \approx \frac{1}{2} \frac{- \int_V (\Delta\epsilon |E_0|^2 + \Delta\mu |H_0|^2) dv}{\int_V (\epsilon |E_0|^2 + \mu |H_0|^2) dv} \quad (4.5)$$

Since outside of the perturbing object $\Delta\epsilon$ and $\Delta\mu$ is zero, we can rewrite 4.5 as:

$$\frac{\omega - \omega_0}{\omega} \approx \frac{1}{2} \frac{- \int_{V_{\text{object}}} (\Delta\epsilon |E_0|^2 + \Delta\mu |H_0|^2) dv}{\int_V (\epsilon |E_0|^2 + \mu |H_0|^2) dv} \quad (4.6)$$

which proves, that any increase of ϵ or μ in the cavity yields to a lowering of the cavity's resonant frequency.

Applications of the small perturbation theory are fine cavity tuning, measurement of the electric or magnetic field distribution inside the cavity, or measurement of the permittivity or permeability of the objects inserted into a cavity. If the object inserted is lossy, then by the change of resonator Q factor, the loss factor of the inserted dielectric or magnetic material can be determined.

4.3 Cavity shape and volume perturbations, Slater's theorem

Another type of cavity perturbation is mechanical deformation of the cavity's boundaries. This can be caused for example by the outside pressure, but also by the electromagnetic

forces from the inside of the cavity. Following the cavity volume variations the resonant frequency is changing as well. A theory worked out by Slater [22], analyses the detuning caused by the boundary changes.

Let us start with the calculation of the electromagnetic stress on the conducting boundary (see Fig. 4.3). The force density of the electromagnetic field is given by Lorentz's formula:

$$\mathbf{f} = \rho\mathbf{E} + \mathbf{j} \times \mathbf{B} \quad (4.7)$$

By calculations, shown step by step in [23], we will obtain the electromagnetic pressure on the surface oriented perpendicularly to the x direction (see Fig. 4.3):

$$P_{x,\text{general}} = \frac{1}{2} \left[\epsilon_0 \left(E^2 - 2E_x^2 \right) + \mu_0 \left(H^2 - 2H_x^2 \right) \right] \quad (4.8)$$

where $E^2 = E_x^2 + E_y^2 + E_z^2$ is the magnitude of the E vector, and E_x^2 is magnitude of its x component.

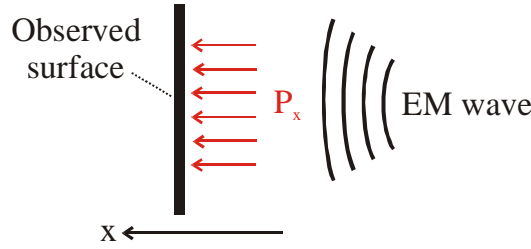


Fig. 4.3: Pressure of the electromagnetic wave on the surface

For example if a travelling wave is hitting an absorber (flat, perpendicular to the wave propagation direction), components $E_x=0$ and $H_x=0$. From 4.8 we obtain the well known radiation pressure on the absorber wall:

$$P_{x,\text{absorbed wave}} = \frac{1}{2} \left(\epsilon_0 E^2 + \mu_0 H^2 \right) \quad (4.9)$$

When using general formula 4.8 for the standing wave, components $E=E_x$ and $H_x=0$, and we obtain:

$$P_{x,\text{standing wave}} = \frac{1}{2} \left(\mu_0 H^2 - \epsilon_0 E^2 \right) \quad (4.10)$$

Since P is proportional to the square of the fields ($P_{\text{instantaneous}} \sim \cos^2(\omega t)$), the cavity surface cannot follow this pressure and feels only the time averaged action. Therefore when using H and E as peak values, both components must be multiplied by a factor of 1/2.

$$\langle P_{x,\text{standing wave}} \rangle = \frac{1}{4} (\mu_0 H_{pk}^2 - \epsilon_0 E_{pk}^2) \quad (4.11)$$

As we can see, forces caused by the electric fields are oriented inwards (as with the attracting plates of a plate capacitor), so the cavity wall will be pulled-in. Since the maximum of the electric field is in the region of iris, maximal inward deformation will take place there as well. In contrast, the maximum of the magnetic field is around the cavity equator, yielding highest outward deformation there – see Fig. 4.4. Effect of cavity detuning by its internal fields is called Lorentz force detuning [24].

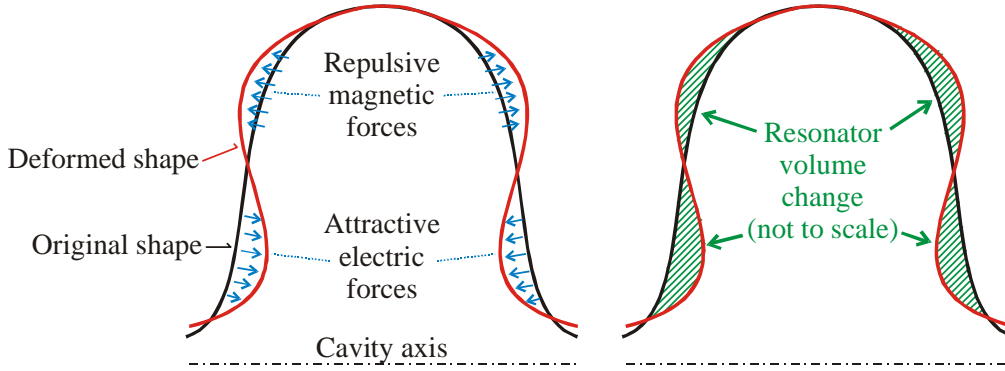


Fig. 4.4: Cavity deformation due to the internal electromagnetic forces

Now, using principles of momentum conservation and the adiabatic invariance we are able to calculate the shift in resonant frequency caused by the wall deformation. Let us assume the excited cavity is resonating with one mode at frequency ω and with energy stored in the cavity U .

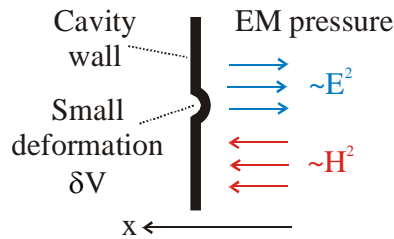


Fig. 4.5: Small deformation of the cavity wall

Now by slow small inward displacement of the cavity wall (Fig. 4.5) we are doing work on the excited mode [25] [26]:

$$\delta U = \int P dS \delta \xi \quad (4.12)$$

where P is the electromagnetic field pressure at the wall (see formula 4.10), $dS \delta \xi$ is characterising the amount of the deformation.

As we apply the displacement $\delta\xi$ we are perturbing a harmonic oscillator. In case of slow changes, we have an adiabatic invariant:

$$\delta\left(\frac{U}{\omega}\right) = 0 \quad (4.13)$$

Adiabatic invariance determines the shift in mode frequency due to the perturbation of the boundary – *Slater's theorem*:

$$\frac{\delta\omega}{\omega} = \frac{1}{2} \frac{\delta U}{U} = -\frac{1}{2U} \int (\mu_0 H^2 - \epsilon_0 E^2) \delta V \quad (4.14)$$

The integral extends over the volume excluded from the cavity by the perturbation. Pushing inwards onto the cavity wall where E is dominant performs negative work – lowers the energy, and therefore the frequency (note: pushing inwards means lowering the volume, so δV is negative). Pushing inwards where the H field is dominant requires work to be done, hence it raises the energy and therefore the frequency.

Unfortunately, formulas 4.11 and 4.14 have the same dependence on E and H, hence the cavity frequency will always be in any case only lowered. It is not possible to build a cavity where the Lorentz force effects will compensate each other.

4.4 Accelerator RF system topologies

To accelerate charged particles, an RF system is used. As was described earlier, such a system consists of the RF power amplifiers, accelerating cavities and the control and feedback system. The number of accelerating structures depends on the accelerator size. The way in which these structures (cavities) are supplied with the RF power will be described in this section.

The topology “one klystron per cavity²” is shown in Fig. 4.6. Each accelerating cavity is equipped by its power amplifier, circulator and control system. This topology offers full control of the field in each individual cavity, but requires a complete set of relatively expensive components for each cavity. The RF system of the CEBAF accelerator [73] is an example of such a topology. To supply the 320 superconducting cavities, it uses 320 klystrons 6kW/1.5GHz, one per cavity.

² In general it is valid for any transmitter, or amplifier. However at power levels discussed in this work, exclusively klystrons are used.

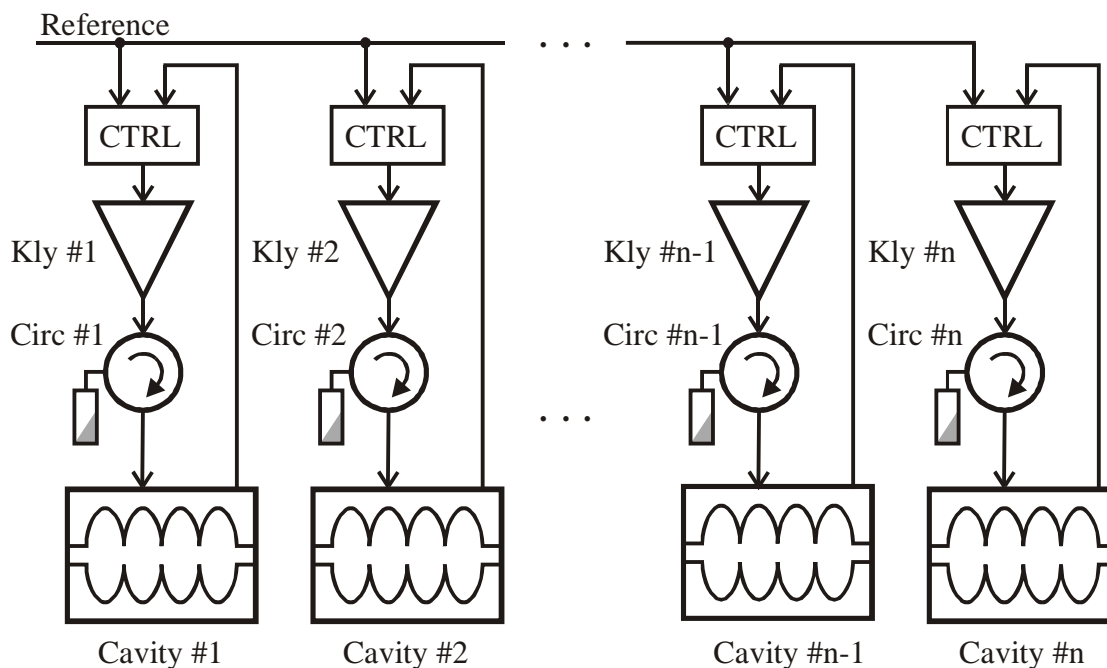


Fig. 4.6: One cavity per klystron configuration (Kly – klystron, Circ – circulator, CTRL – controller and feedback system)

The topology “multiple cavities per klystron” is shown in Fig. 4.7. One more powerful transmitter supplies many accelerating cavities using power splitters. In accelerators, usually 4, 8 or 16 cavities per transmitter are used. This choice is more economical, because the price of the transmitters is not rising proportionally to the output power, and the number of expensive components can be reduced. However, such a system does not allow individual control of the field in each cavity and only the overall sum of voltages from each cavity can be stabilized by the feedback system. So, if by any perturbation, the tune state of any cavity is changed, the voltage and phase of the cavity field will change and will not be controlled anymore.

Such a topology was used, for example, in the former LEP2 storage ring, where one 1MW klystron was feeding eight superconducting cavities [31]. The LEP2 RF system was operated in continuous mode and problems related to the cavity dynamics (detuning, low frequency vibrations etc.) were compensated by relatively slow tuners (bandwidth $\approx 100\text{Hz}$) [32].

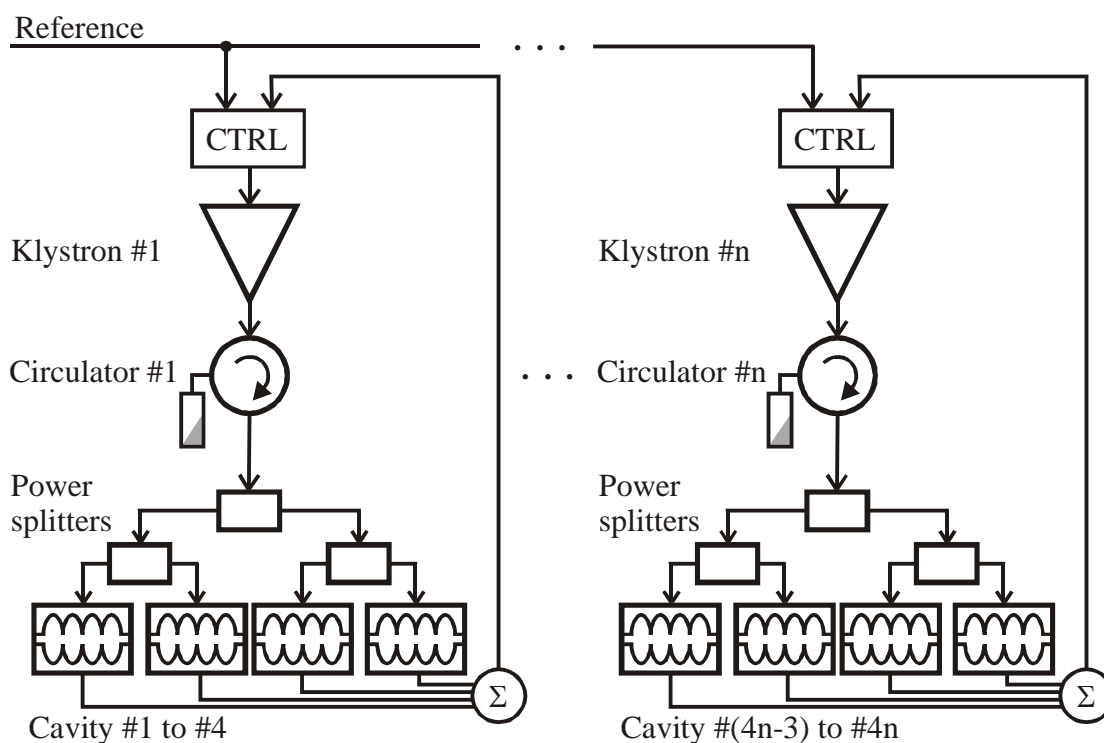


Fig. 4.7: Multiple cavities per klystron configuration (in this case 4)

4.5 Proposal of the RF system of the SPL accelerator

SPL – the Superconducting Proton Linac [30] – is a linear accelerator proposal being studied at CERN. It should deliver an H^- beam⁸ with an energy of 2.2 GeV and a beam power of 4 MW. To use most of the superconducting RF cavities and RF systems available after the decommissioning of the LEP collider, it was planned to operate at 352 MHz and to deliver 10^{16} protons per second, in 2.2 ms bursts with a repetition rate of 50 Hz. In conjunction with an accumulator and a compressor, it is designed to be the proton driver of a neutrino factory at CERN. At an early stage, it will upgrade the performance of the CERN's PS complex by replacing the Linac2 and the PS Booster. Some parameters of the RF subsystems planned for the SPL accelerator are given in the Table 4.1.

⁸ Negatively charged hydrogen ions (H^-) instead of protons (H^+) are accelerated, charge exchange injected into a following synchrotron, to minimize the injection losses

Section	Input energy (MeV)	Output energy (MeV)	Number of cavities	Peak RF power (MW)	Number of klystrons	Number of tetrodes	Length (m)
Source, LEPT	–	0.045	–	–	–	–	3
RF quadrupoles 1	0.045	3	1	0.4	1	–	3
Chopperline	3	3	5	0.3	–	5	6
RF quadrupoles 2	3	7	1	0.5	1	–	4
DTL	7	120	100	8.7	11	–	78
Superconducting cavities – reduced β	120	1080	122	10.6	12	74	334
Superconducting cavities – ex LEP	1080	2200	108	12.3	18	–	345
Debunching	2200	2200	8	–	1	–	26
Total			345	32.8	44	79	799

Table 4.1: Parameters of the SPL's RF installations

4.6 A transmission controlling device – the phase and amplitude modulator

For the SPL accelerator, a pulsed operation of the RF system is foreseen. Each cavity with its ancillary equipment is also a mechanical resonator and the Lorentz forces linked to the pulsed RF fields will excite the mechanical modes of this object. The excited amplitudes may become large when a multiple of the pulsing frequency is close to a mechanical resonance. A vector-sum will add the voltages from all the cavities fed by one klystron, resulting in a signal which is equivalent to what the beam sees from this group of cavities. This signal is fed back to the klystron to stabilise the total field. If there is more than one cavity connected to a klystron, the system is not completely defined. The vector-sum feedback stabilises only the sum of the voltage, but not the voltage in each individual cavity. For low excitation the practically identical cavities behave identically and the cavity voltages are equally distributed between the cavities. But as discovered by numerical simulations [33], above a certain threshold, this is not the case anymore. The cavities can behave differently, some delivering more voltage, some less. A mathematical analysis [34] showed that this is a real effect and not a simulation artefact. To avoid this problem, a control for each individual cavity voltage is necessary. A solution keeping a common large power source with power splitters was proposed in [35].

If a fast phase and amplitude modulator, to be inserted into each cavity feeder line, can be built at reasonable cost, it could provide the necessary individual cavity control capabilities (see Fig. 4.8).

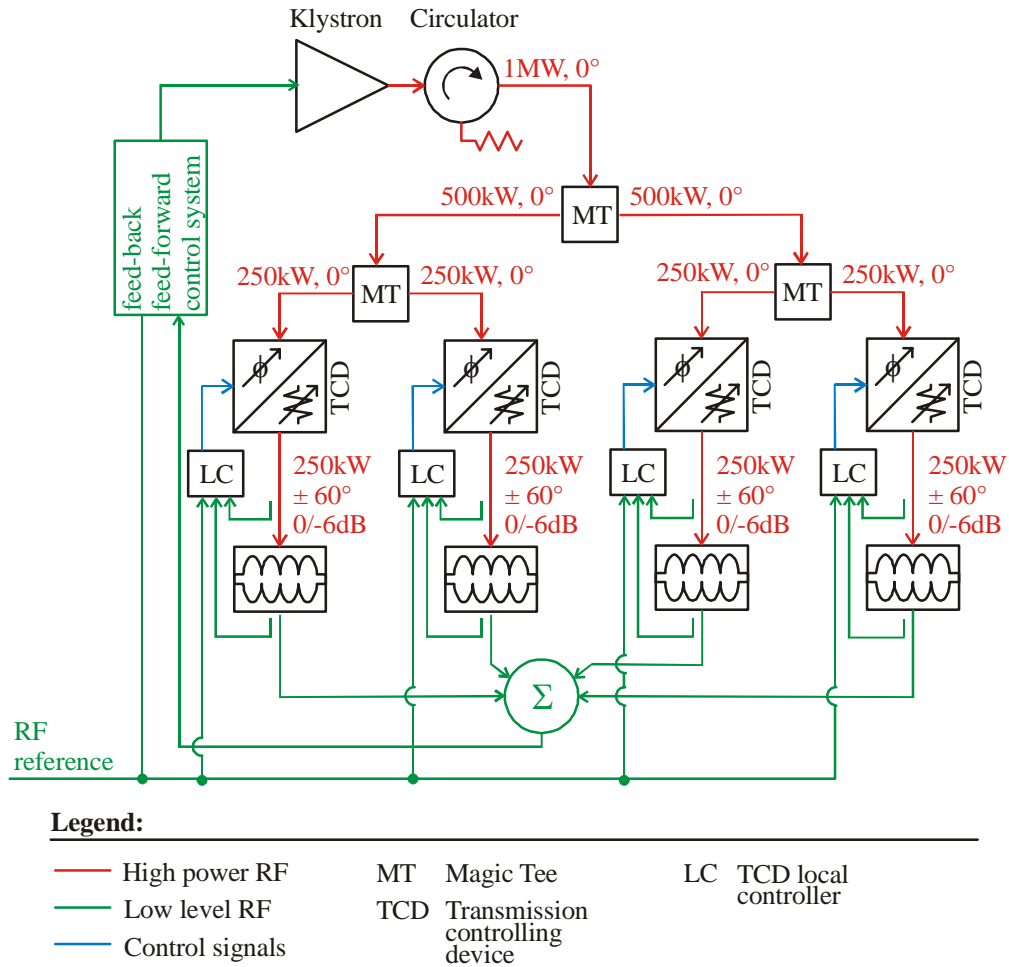


Fig. 4.8: Use of transmission controlling devices as proposed by H. Frischholz [35]

To keep the cavity field constant, we need a device capable of independently changing both the phase and amplitude of the cavity incident wave. A simple phase modulator represents only one degree of freedom – changing the phase of the wave. By combining two phase modulators using one or more RF hybrids, both phase and amplitude of the incident wave can be controlled. The fast phase and amplitude modulator, or “Transmission Controlling Device (TCD)” must be able to compensate individual deviations of each cavity to equalize their behaviour with respect to the RF reference signal. In the proposed configuration the local controller of each TCD compares the phase and amplitude of the field in each cavity with the reference signal, and tries to set its transmission such that it compensates the individual deviations from the RF reference set value [36].

Since the Lorentz force detuning phenomenon is related to mechanical oscillations of the cavity RF wise it is a relatively slow process. The mechanical mode with the strongest detuning effect in the LEP cavities is around 100Hz. The higher mechanical modes have

amplitudes less and less disturbing to the RF performance of the cavity. The modes above 1kHz are considered to be negligible.

The Lorentz force is not the only source of detuning and disturbances. Since the cavity is surrounded by liquid helium, it is also sensitive to pressure changes caused by compressor pulsing, bubbles in the liquid or cryogenic regulation variations for example. Mechanical noises propagating on the beam pipes, cavity supports or waveguides are also influencing the cavity.

The practical realization of the phase and amplitude modulator might be done in several ways. Nevertheless due to the very high RF power levels (both peak and r.m.s.), only a limited choice of devices is available. In chapter 6, various configurations of the phase and power modulators are proposed and mathematically analysed. In chapter 8, different types of structures that can be used as phase-shifters within these modulators are analysed.

5

Detailed objectives for this work

The presented work concerns the domain of high power microwave technology related to particle accelerators, theoretical considerations and final proposals for the realisation of a corresponding device. The results are foreseen to be applied in the field of particle accelerators but are certainly also interesting for other high power RF domains e.g. tuning devices for industrial microwave heating, plasma applications or nuclear fusion reactors.

To introduce the initial problem, the fundamentals of particle acceleration and particular cavity resonators were defined. In particular a cost-effective scheme of supplying many cavities by one powerful transmitter was shown. The Lorentz force detuning effect was demonstrated. For classical accelerators, working with CW signals, this detuning is static and compensated by the tuning system. The proposed SPL accelerator will use superconducting cavities in the pulsed mode. However, the pulsed operation of the superconducting cavities, as only recently considered, results in dynamic detuning effects. When considering the possible enhancement by cavity mechanical resonances, it can no longer be compensated by the classical, mechanical slow cavity tuning system. New ways of handling this problem have to be found.

A cost-effective way to supply several cavities by one transmitter while keeping possibility of controlling the field in each individual cavity is by introducing a fast phase and amplitude modulator – also called a “Transmission controlling device” – into each cavity feeder line. This device is capable simultaneously of controlling the phase and amplitude of the passing wave.

In this way the modulator will compensate the individual deviations of each cavity in order to equalize their behaviour for the main control loop, which will compensate the average detuning of whole system [36].

Nevertheless, the problem of pulsing superconducting cavities is relatively new and there is not yet a lot of practical experience in the field world-wide. In order to study the behaviour of

such systems and to build working pulsed superconducting linacs, the following points have to be further studied:

1. Analysis of the requirements for the phase and amplitude modulator
 - a. Determination of the necessary phase and amplitude tuning range
 - b. Determination of the necessary tuning frequency (speed)
2. Analysis and detailed study of the transmission controlling device
 - a. Different circuit topologies, number of hybrids, types of hybrids
 - b. Different types of phase-shifters, transmission type, reflection type
 - c. Determination of the necessary phase tuning range
 - d. Detailed study of its behaviour when working with the matched or fully reflecting load
3. Analysis and development of the high power, fast ferrite phase-shifters to be used in the transmission controlling device
 - a. Study of the different topologies – reflective type of phase-shifter, transmission type of phase-shifter
 - b. Compatibility with very high power RF signals
 - c. Coherence with industry manufacturing capabilities
 - d. Optimization of the structure to achieve a good RF performance
 - e. Attenuation, phase-shift range, RF leakage out of the phase-shifters
 - f. Optimization of the structure to achieve high tuning speeds with reasonable tuning power
4. Study of the system integration
 - a. Analysis of the control needs
 - b. Precision of the obtained results
 - c. Exactness of the transfer function for any working condition

6

Phase and amplitude modulators

To compensate the Lorenz force detuning of the SC cavities, the fast phase and amplitude modulators have to be inserted into each cavity feeder line. A practical realization of the transmission controlling device might be done in several ways. Nevertheless the very high RF power levels (both peak and r.m.s.) limit the choice of devices that can be used. In this chapter, different possible configurations will be analyzed.

6.1 Definition of components

6.1.1 Quadrature (90°) hybrid

Quadrature hybrids are 3dB directional couplers with a 90° phase difference in the outputs of the through and coupled arms.

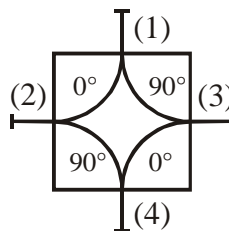


Fig. 6.1: Quadrature hybrid

This type of hybrid may be realized in waveguide form (Fig. 6.2) or made in micro-strip or strip-line form (Fig. 6.4).

The waveguide version shown in Fig. 6.3 – the Riblet short-slot coupler – consists of two waveguides with a common sidewall. Coupling takes place in the centre where part of the wall is absent. In this region, both the TE_{10} (even) and TE_{20} (odd) modes are excited. When properly designed, they cancel at the isolated port, and add up at the coupled port. The width of the interaction region must be reduced to prevent propagation of the undesired TE_{30} mode. This type of coupler can usually be smaller than other waveguide couplers [68].

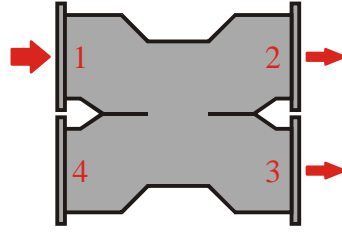


Fig. 6.2: Riblet short-slot waveguide coupler

A special development on waveguide 3dB hybrids has been done by Nantista and Fowkes in the Stanford Linear Accelerator Centre [69]. The design of the Next Linear Collider [71] requires powering of the high-gradient accelerating structures of the main linacs with 11.424 GHz X-band klystrons through a pulse compression and a power distribution system [72]. The pulsed RF signals will be combined, split or directed at peak power levels reaching 600 MW using novel waveguide hybrids (see Fig. 6.3) capable of handling very high power levels.

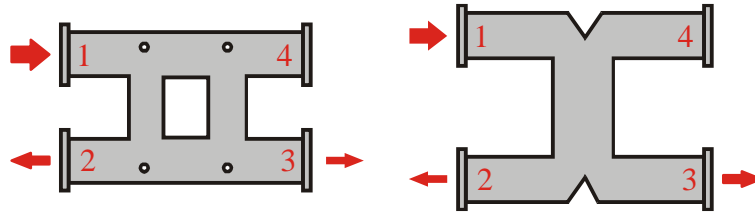


Fig. 6.3: Waveguide quadrature hybrids for the multi hundred-megawatt RF system

The micro-strip, or strip-line type of the coupler (Fig. 6.4) is known as a branch line hybrid. The branch line hybrid has a high degree of symmetry – any port may be used as an input port. When properly designed, it is able to handle a high RF power, which is necessary for the SPL's RF system application.

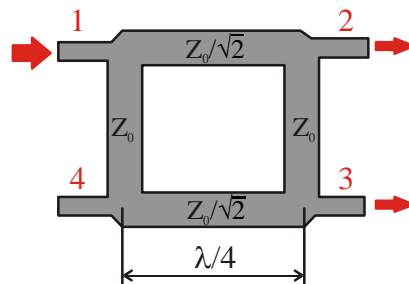


Fig. 6.4: Strip-line version – The Branch line hybrid

Operation of the quadrature hybrid is fully described by its scattering matrix:

$$S_{QH} = \begin{pmatrix} S_{11} & S_{12} & S_{13} & S_{14} \\ S_{21} & S_{22} & S_{23} & S_{24} \\ S_{31} & S_{32} & S_{33} & S_{34} \\ S_{41} & S_{42} & S_{43} & S_{44} \end{pmatrix} = \frac{1}{\sqrt{2}} \begin{pmatrix} 0 & j & 1 & 0 \\ j & 0 & 0 & 1 \\ 1 & 0 & 0 & j \\ 0 & 1 & j & 0 \end{pmatrix} \quad (6.1)$$

When all ports are matched, the power entering port 1 is equally split towards ports 2 and 3 with a 90° phase difference. No power is coupled to the port 4.

6.1.2 The 180° hybrid

The 180° hybrid junction is a four-port network, with a 180° phase shift between the two outputs (Δ). It also can be operated with outputs in phase (Σ) – see Fig. 6.5.

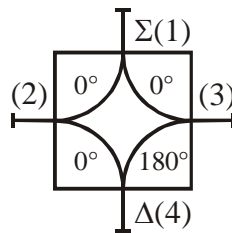


Fig. 6.5: The 180° hybrid

This type of hybrid may also be realised in waveguide form – the Magic Tee, or made in micro-strip or strip-line form – the ring (rat-race) hybrid.

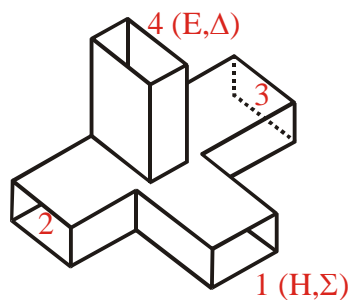


Fig. 6.6: Magic Tee – the waveguide version of 180° hybrid

The waveguide hybrid junction – known as Magic Tee – is shown in Fig. 6.6. When a TE_{10} mode is incident to port 1, the electric field has an even symmetry about the mid-plane and hence cannot excite the TE_{10} mode in arm 4. It is equally split in phase towards ports 2 and 3. There is no coupling between port 1 and 4. The coupling from port 4 to ports 2 and 3 is equal in magnitude, but 180° out of phase. There is again no coupling from ports 4 to 1.

A strip-line version of the hybrid is shown in Fig. 6.7. A wave incident to port 1 is equally split into two waves travelling around the ring. The wave arrives in phase to ports 2 and 3, and out of phase to port 4. Ports 1 and 4 are uncoupled, since the path coupling these ports differs by $\lambda/2$.

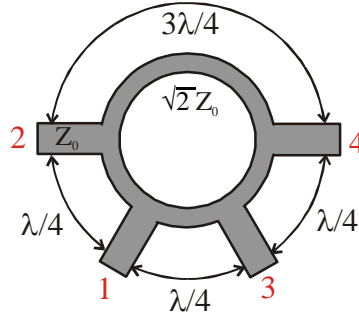


Fig. 6.7: Strip-line version of the 180° ring hybrid – the rat-race structure

Operation of the 180° hybrid is again fully described by its scattering matrix:

$$S_{MT} = \begin{pmatrix} S_{11} & S_{12} & S_{13} & S_{14} \\ S_{21} & S_{22} & S_{23} & S_{24} \\ S_{31} & S_{32} & S_{33} & S_{34} \\ S_{41} & S_{42} & S_{43} & S_{44} \end{pmatrix} = \frac{1}{\sqrt{2}} \begin{pmatrix} 0 & 1 & 1 & 0 \\ 1 & 0 & 0 & 1 \\ 1 & 0 & 0 & -1 \\ 0 & 1 & -1 & 0 \end{pmatrix} \quad (6.2)$$

6.1.3 Phase shifters

As discussed in chapter 7, there are two different types of phase-shifter available:

- single port – reflective type of phase-shifter
- two port – transmission type of phase-shifter

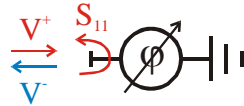


Fig. 6.8: Reflective type of phase-shifter

The reflective type of phase-shifter, is described by the equation:

$$S_{11} = \Phi = \frac{V^-}{V^+} = F e^{-j\phi} \quad (6.3)$$

where F is amplitude of the reflection coefficient and ϕ is the phase of reflection coefficient. For lossless phase shifters $F=1$.

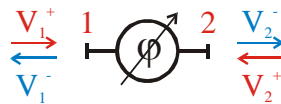


Fig. 6.9: Transmission type of phase-shifter

The reciprocal, transmission type of phase-shifter will be described by equations:

$$S_{11} = S_{22} = 0 \quad (6.5)$$

$$\Phi^+ = \frac{V_2^-}{V_1^+} = F e^{-j\phi} \quad (6.6)$$

$$\Phi^- = \frac{V_1^-}{V_2^+} = F e^{-j\phi} \quad (6.7)$$

considering the forward (+) and reflected (-) wave propagation. F is the amplitude of the transmission coefficient and ϕ is the phase of the transmission coefficient. For lossless phase shifters $F=1$.

6.1.4 Loads

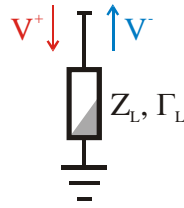


Fig. 6.10: General RF load

The RF load (Fig. 6.10) is described by its voltage reflection coefficient:

$$\Gamma_L = G e^{-j\gamma} \quad (6.8)$$

where G is the magnitude of the voltage reflection coefficient of the load and γ its phase. Without beam, a superconducting cavity reflects all power back to the generator with an arbitrary phase. Depending on the tuning frequency with beam, the load will become partly a source and the voltage induced by the beam might even be higher than the generator voltage. The connected devices must be able to handle this situation. We will not consider the influence of the beam in this context.

The RF dummy loads are used with the hybrids. Earlier, water filled loads were used but water as an absorbing medium induces several difficulties. For example, the need of leak tight waveguide/coaxial windows, the risk of flooding the waveguide structure with water and the high variation of the RF parameters (mainly the reflected phase) with temperature. Hence in the present systems, the dry ferrite loads are preferred as they do not suffer from any of these problems.

6.2. Phase and amplitude modulator using a single 3dB hybrid

The simplest configuration of the phase and amplitude modulator uses a single hybrid and two reflection type phase-shifters.

Two cases with different types of hybrids and the possibility of operation in different working modes are analysed.

6.2.1 Modulator with single Magic Tee working with an arbitrary load

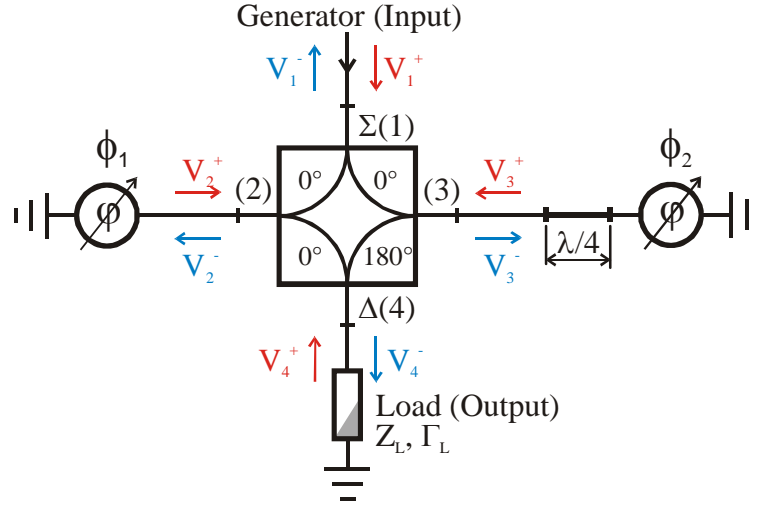


Fig. 6.11: Phase and amplitude modulator using single Magic Tee

Voltages of the waves in the structure are defined as:

$$V_2^+ = V_2^- \Phi_1 = V_2^- F_1 e^{-j\phi_1} \quad (6.9)$$

$$V_3^+ = V_3^- \Phi_2 = V_3^- F_2 e^{-j(\phi_2 - \pi)} \quad (6.10)$$

$$V_4^+ = V_4^- \Gamma = V_4^- G e^{-j\gamma} \quad (6.11)$$

Where all voltages, Φ_1 , Φ_2 and G are phasors of corresponding quantities. Using the scattering matrix of the Magic Tee (6.2), we get:

$$\begin{pmatrix} V_1^- \\ V_2^- \\ V_3^- \\ V_4^- \end{pmatrix} = \frac{1}{\sqrt{2}} \begin{pmatrix} 0 & 1 & 1 & 0 \\ 1 & 0 & 0 & 1 \\ 1 & 0 & 0 & -1 \\ 0 & 1 & -1 & 0 \end{pmatrix} \begin{pmatrix} V_1^+ \\ V_2^+ \Phi_1 \\ V_3^+ \Phi_2 \\ V_4^+ \Gamma \end{pmatrix} \quad (6.12)$$

Yielding the final system of equations to describe the behaviour of the structure:

$$\begin{aligned}
 \sqrt{2} V_1^- &= V_2^- \Phi_1 + V_3^- \Phi_2 \\
 \sqrt{2} V_2^- &= V_1^+ + V_4^- \Gamma \\
 \sqrt{2} V_3^- &= V_1^+ - V_4^- \Gamma \\
 \sqrt{2} V_4^- &= V_2^- \Phi_1 - V_3^- \Phi_2
 \end{aligned} \tag{6.13abcd}$$

These equations are solved by:

$$\begin{aligned}
 V_1^- &= V_1^+ \frac{\Phi_1 + \Phi_2 - 2\Phi_1\Phi_2\Gamma}{2 - \Gamma(\Phi_1 + \Phi_2)} \\
 V_2^- &= V_1^+ \sqrt{2} \frac{1 - \Phi_2\Gamma}{2 - \Gamma(\Phi_1 + \Phi_2)} \\
 V_3^- &= V_1^+ \sqrt{2} \frac{1 - \Phi_1\Gamma}{2 - \Gamma(\Phi_1 + \Phi_2)} \\
 V_4^- &= V_1^+ \frac{\Phi_1 - \Phi_2}{2 - \Gamma(\Phi_1 + \Phi_2)}
 \end{aligned} \tag{6.14abcd}$$

The solution for V_4^- (6.14d) gives an expression for the forward load voltage:

$$V_4^- = V_1^+ \frac{\Phi_1 - \Phi_2}{2 - \Gamma(\Phi_1 + \Phi_2)} \tag{6.15}$$

As expected, the output voltage depends on the load voltage reflection coefficient Γ for a mismatched load. (6.15) might even diverge when the denominator would approach zero. In a real system, this can cause a RF breakdown.

The Φ_1 , Φ_2 and Γ may all have the magnitude of 1. If Φ_1 , Φ_2 will have the same argument, which is opposite to the argument of Γ , the denominator becomes zero. But for equal Φ_1 and Φ_2 the numerator also becomes zero, preventing divergence. To calculate the limit condition, we assume a small, possibly complex number ε and express Φ_2 as:

$$\Phi_2 = \Phi_1 (1 - \varepsilon) \tag{6.16}$$

Then we get:

$$V_4^- = V_1^+ \frac{\varepsilon \Phi_1}{2 - \Gamma\Phi_1(2 - \varepsilon)} \tag{6.17}$$

Since Φ_1 and Γ have opposite arguments and both magnitude 1, we have $\Phi_1\Gamma=1$ and hence:

$$V_4^- = V_1^+ \Phi_1 \tag{6.18a}$$

Since F1 has magnitude 1, (6.18a) results in

$$|V_4^-| = |V_1^+| \quad (6.18b)$$

This means, that even in extreme conditions the output voltage will not be larger than the input voltage of the device. Nevertheless, since the output voltage of the modulator is dependent on the reflections from its load, the phase-shifters and the control system must be fast enough to compensate these changes, otherwise the amplitude and phase modulator will not work properly.

6.2.2 Modulator with a single Magic Tee working with a matched load

Adding a (small) circulator in the load feeder line ensures the modulator sees only a matched load, i.e. $\Gamma=0$ as shown in Fig. 6.12.

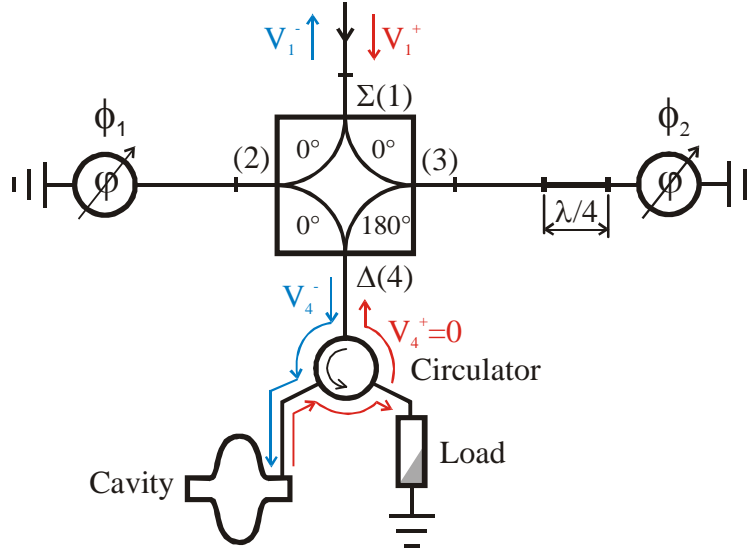


Fig. 6.12: Phase and amplitude modulator with single Magic Tee and the circulator

The transfer function (6.15), assuming loss less phase-shifters will then reduce to:

$$\frac{V_4^-}{V_1^+} = \frac{\Phi_1 - \Phi_2}{2} = \frac{e^{-j\Phi_1} + e^{-j\Phi_2}}{2} \quad (6.19)$$

The argument of the transfer function – the phase modulation will be:

$$\text{Arg} \left[\frac{V_4^-}{V_1^+} \right] = -\frac{\Phi_1 + \Phi_2}{2} \quad (6.20)$$

The magnitude of the transfer function – the amplitude modulation will be:

$$\text{Mag} \left[\frac{V_4^-}{V_1^+} \right] = \sqrt{\frac{1 + \cos(\varphi_1 - \varphi_2)}{2}} \quad (6.21)$$

Results from formula (6.20) are plotted in Fig. 6.13 and results from formula (6.21) are plotted in Fig. 6.14.

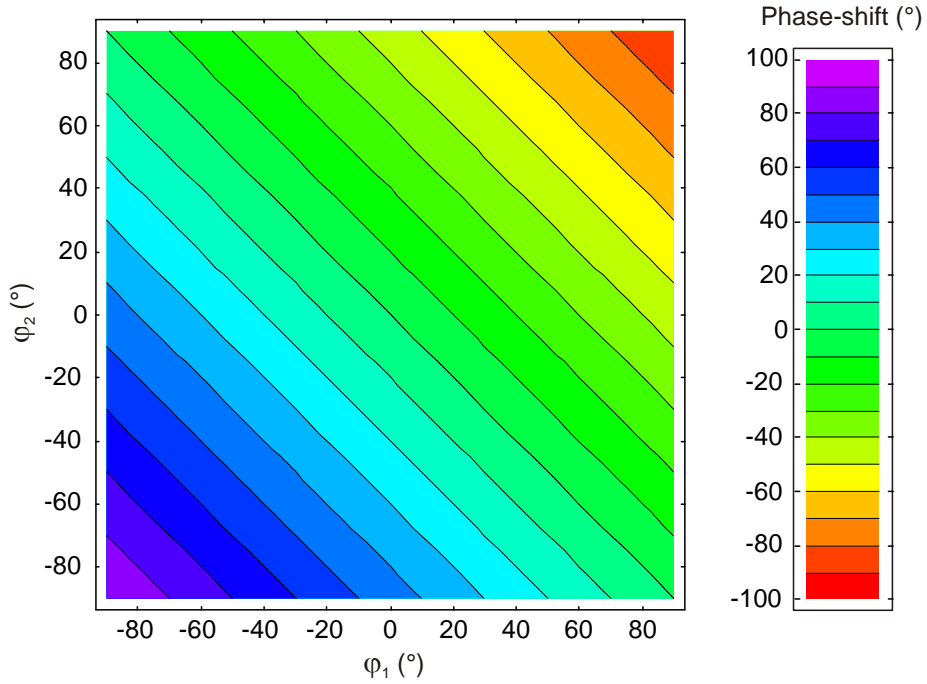


Fig. 6.13: Phase modulation by the phase and amplitude modulator

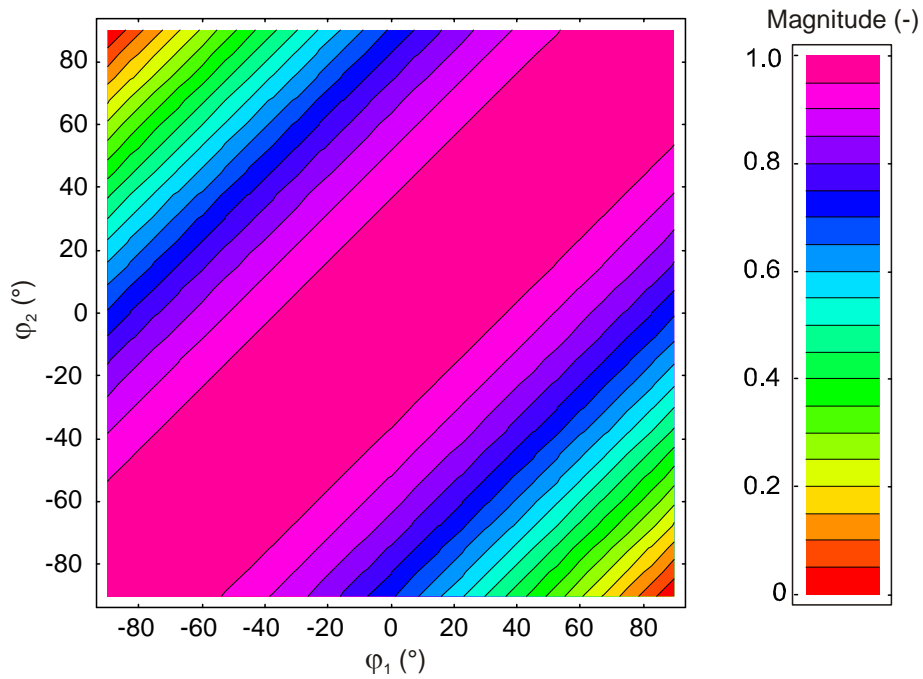


Fig. 6.14: Amplitude modulation by the phase and amplitude modulator

6.2.3 Operation of the modulator with $\varphi_1=\varphi_2$

If the phase-shifts of the phase-shifters are kept equal ($\varphi_1=\varphi_2=\varphi$), the modulator will behave as a transmission type phase-shifter. This can be useful at lower frequencies, where it is often easier or more economic to build the reflection type of phase-shifters. For the price of using two identical phase-shifters, the more expensive circulator at the output of the modulator can be avoided.

The phase-shift given by formula (6.20) will become

$$\text{Arg} \left[\frac{V_4^-}{V_1^+} \right] = -\frac{\varphi + \varphi}{2} = -\varphi \quad (6.22)$$

and the magnitude of transfer function (6.21) will become:

$$\text{Mag} \left[\frac{V_4^-}{V_1^+} \right] = \sqrt{\frac{1 + \cos(\varphi - \varphi)}{2}} = 1 \quad (6.23)$$

It can be shown, that the “reverse” transfer function (from port 4 to port 1) will be the same as the “forward” transfer function:

$$\text{Arg} \left[\frac{V_4^-}{V_1^+} \right] = \text{Arg} \left[\frac{V_1^-}{V_4^+} \right] = -\varphi \quad (6.24)$$

and

$$\text{Mag} \left[\frac{V_4^-}{V_1^+} \right] = \text{Mag} \left[\frac{V_1^-}{V_4^+} \right] = 1 \quad (6.25)$$

6.2.4 Modulator with a single quadrature hybrid working into an arbitrary load

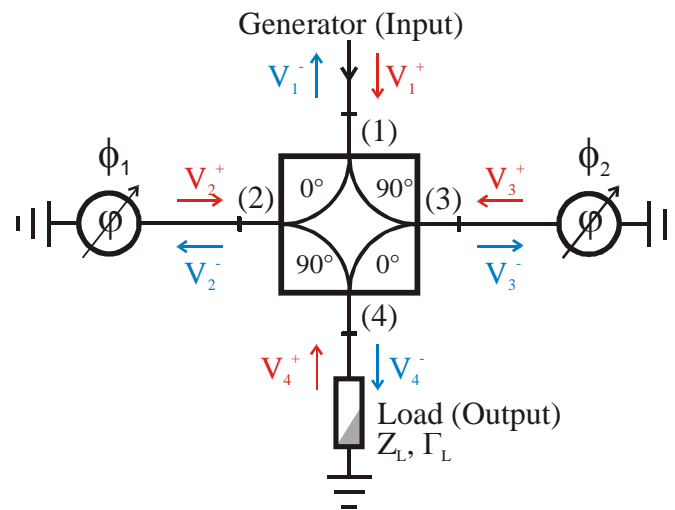


Fig. 6.15: Phase and amplitude modulator using single quadrature hybrid

Using exactly the same techniques as in the previous case of the single Magic Tee configuration, we can describe the voltages (waves) in the structure by:

$$V_2^+ = V_2^- \Phi_1 = V_2^- F_1 e^{-j\phi_1} \quad (6.26)$$

$$V_3^+ = V_3^- \Phi_2 = V_3^- F_2 e^{-j\phi_2} \quad (6.27)$$

$$V_4^+ = V_4^- \Gamma = V_4^- G e^{-j\gamma} \quad (6.28)$$

Using the scattering matrix of quadrature hybrid (6.1), we get:

$$\begin{pmatrix} V_1^- \\ V_2^- \\ V_3^- \\ V_4^- \end{pmatrix} = \frac{1}{\sqrt{2}} \begin{pmatrix} 0 & j & 1 & 0 \\ j & 0 & 0 & 1 \\ 1 & 0 & 0 & j \\ 0 & 1 & j & 0 \end{pmatrix} \begin{pmatrix} V_1^+ \\ V_2^- \Phi_1 \\ V_3^- \Phi_2 \\ V_4^- \Gamma \end{pmatrix} \quad (6.29)$$

And the final system of equations, describing behaviour of the structure is:

$$\begin{aligned} \sqrt{2} V_1^- &= j V_2^- \Phi_1 + V_3^- \Phi_2 \\ \sqrt{2} V_2^- &= j V_1^+ + V_4^- \Gamma \\ \sqrt{2} V_3^- &= V_1^+ + j V_4^- \Gamma \\ \sqrt{2} V_4^- &= V_2^- \Phi_1 + j V_3^- \Phi_2 \end{aligned} \quad (6.30abcd)$$

The solution of the system (6.30abcd) is:

$$\begin{aligned} V_1^- &= V_1^+ \frac{-\Phi_1 + \Phi_2 - 2\Phi_1\Phi_2\Gamma}{2 + \Gamma(\Phi_2 - \Phi_1)} \\ V_2^- &= j V_1^+ \sqrt{2} \frac{1 + \Phi_2\Gamma}{2 + \Gamma(\Phi_2 - \Phi_1)} \\ V_3^- &= V_1^+ \sqrt{2} \frac{1 - \Phi_1\Gamma}{2 + \Gamma(\Phi_2 - \Phi_1)} \\ V_4^- &= j V_1^+ \frac{\Phi_1 + \Phi_2}{2 + \Gamma(\Phi_2 - \Phi_1)} \end{aligned} \quad (6.31abcd)$$

The solution for V_4^- (6.31d) gives the expression for the forward load voltage:

$$V_4^- = j V_1^+ \frac{\Phi_1 + \Phi_2}{2 + \Gamma(\Phi_2 - \Phi_1)} \quad (6.32)$$

As for the first case, the output voltage is a function of the load voltage reflection coefficient, when the modulator is working into a mismatched load. Use of this type of phase and amplitude modulator with a fast changing unmatched load is not recommended.

6.2.5 Modulator with a single quadrature hybrid working with matched load

With the circulator in the load feeder line it can be ensured that the output of the modulator will be matched for any load condition ($\Gamma=0$, Fig. 6.16) and simplifications on (6.31abcd) may be done.

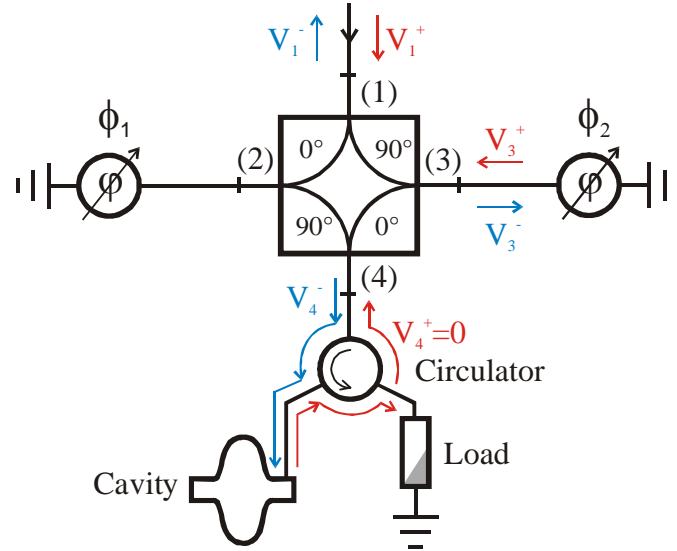


Fig. 6.16: Phase and amplitude modulator with single Magic Tee and the circulator

The transfer function (6.32), assuming loss less phase-shifters will then reduce to:

$$\frac{V_4^-}{V_1^+} = j \frac{\Phi_1 + \Phi_2}{2} = j \frac{e^{-j\Phi_1} + e^{-j\Phi_2}}{2} \quad (6.33)$$

The argument of the transfer function – the phase modulation will be:

$$\text{Arg} \left[\frac{V_4^-}{V_1^+} \right] = -\frac{\Phi_1 + \Phi_2}{2} + \frac{\pi}{2} \quad (6.34)$$

The magnitude of the transfer function – the amplitude modulation will be:

$$\text{Mag} \left[\frac{V_4^-}{V_1^+} \right] = \sqrt{\frac{1 + \cos(\Phi_1 - \Phi_2)}{2}} \quad (6.35)$$

Results from the formula (6.34) are plotted in Fig. 6.17 and results from the formula (6.35) are plotted in Fig. 6.18.

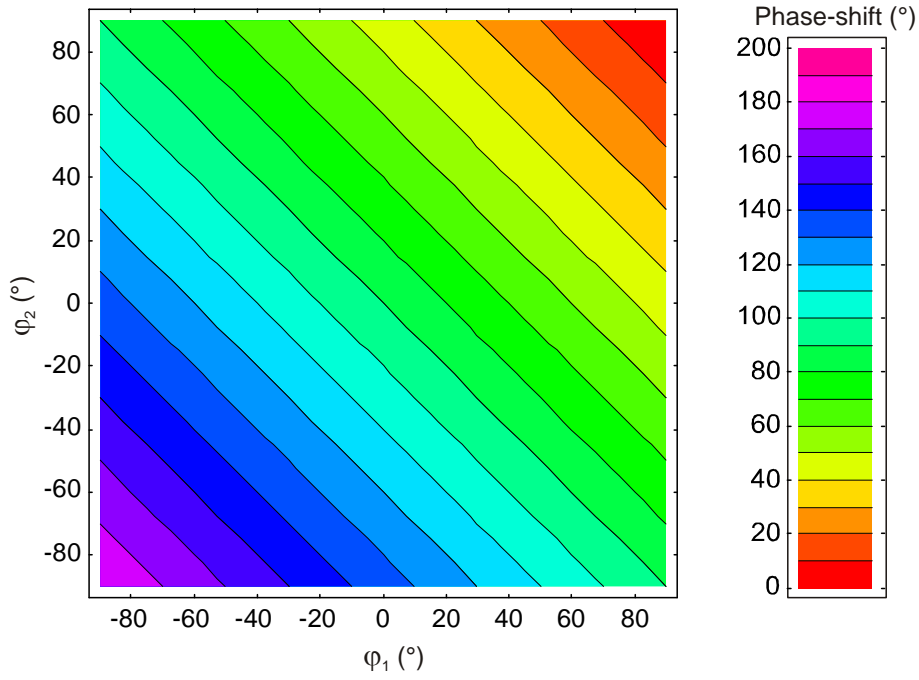


Fig. 6.17: Phase modulation by the phase and amplitude modulator

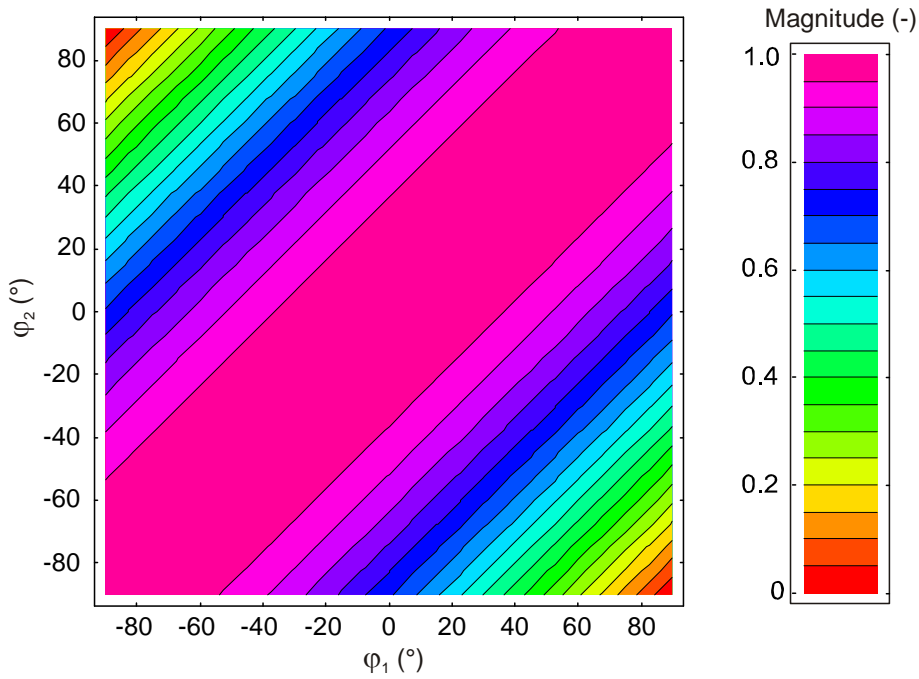


Fig. 6.18: Amplitude modulation by the phase and amplitude modulator

6.2.6 Operation of the modulator with $\phi_1=\phi_2$

As in the case discussed in the section 6.2.3, if the phase shift of both the phase-shifters is kept equal ($\phi_1=\phi_2=\phi$), the modulator will act as a transmission type of phase-shifter. The phase-shift given by formula (6.34) will become:

$$\text{Arg} \left[\frac{V_4^-}{V_1^+} \right] = -\frac{\varphi + \varphi}{2} + \frac{\pi}{2} = -\varphi + \frac{\pi}{2} \quad (6.36)$$

and the magnitude of the transfer function (6.35) will become:

$$\text{Mag} \left[\frac{V_4^-}{V_1^+} \right] = \sqrt{\frac{1 + \cos(\varphi - \varphi)}{2}} = 1 \quad (6.37)$$

It can be shown, that the “reverse” transfer function (from port 4 to port 1) will be the same as the “forward” transfer function:

$$\text{Arg} \left[\frac{V_4^-}{V_1^+} \right] = \text{Arg} \left[\frac{V_1^-}{V_4^+} \right] = -\varphi + \frac{\pi}{2} \quad (6.38)$$

and

$$\text{Mag} \left[\frac{V_4^-}{V_1^+} \right] = \text{Mag} \left[\frac{V_1^-}{V_4^+} \right] = 1 \quad (6.39)$$

6.3. Phase and amplitude modulator using two 3dB hybrids

For a “clean” operation of the amplitude and phase modulator, a two-hybrid configuration with two phase-shifters of transmission type and two RF loads is necessary. The modulator structure is more complex, but it has some favourable properties in comparison to the single hybrid structure. As it will be shown in the next chapter, transmission type of phase-shifters are easier to build for higher frequencies, but operation with double the number of reflection type phase-shifters is also possible (see paragraphs 6.2.3 and 6.2.6).

Two cases with different types of hybrids and the possibility of operation in different working modes are analysed.

6.3.1 Modulator with two Magic Tees working into an arbitrary load

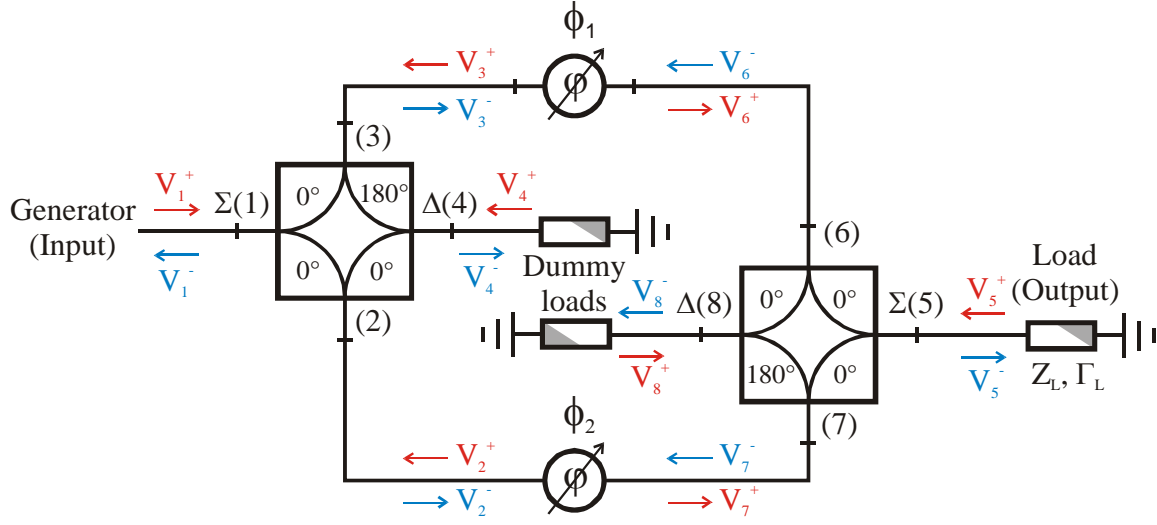


Fig. 6.19: Phase and amplitude modulator using two Magic Tees

Voltages (waves) in the structure are defined as:

$$V_2^+ = V_7^- \Phi_2 = V_7^- F_2 e^{-j\phi_2} \quad (6.40)$$

$$V_3^+ = V_6^- \Phi_1 = V_6^- F_1 e^{-j\phi_1} \quad (6.41)$$

$$V_4^+ = 0 \quad (6.42)$$

$$V_5^+ = V_5^- \Gamma_L = V_5^- G e^{-j\gamma} \quad (6.43)$$

$$V_6^+ = V_3^- \Phi_1 = V_3^- F_1 e^{-j\phi_1} \quad (6.44)$$

$$V_7^+ = V_2^- \Phi_2 = V_2^- F_2 e^{-j\phi_2} \quad (6.45)$$

$$V_8^+ = 0 \quad (6.46)$$

Using the scattering matrix of Magic Tee (6.2), we obtain the final system of equations:

$$\begin{pmatrix} V_1^- \\ V_2^- \\ V_3^- \\ V_4^- \end{pmatrix} = \frac{1}{\sqrt{2}} \begin{pmatrix} 0 & 1 & 1 & 0 \\ 1 & 0 & 0 & 1 \\ 1 & 0 & 0 & -1 \\ 0 & 1 & -1 & 0 \end{pmatrix} \begin{pmatrix} V_1^+ \\ V_7^- \Phi_2 \\ V_6^- \Phi_1 \\ 0 \end{pmatrix} \quad (6.47a)$$

$$\begin{pmatrix} V_5^- \\ V_6^- \\ V_7^- \\ V_8^- \end{pmatrix} = \frac{1}{\sqrt{2}} \begin{pmatrix} 0 & 1 & 1 & 0 \\ 1 & 0 & 0 & 1 \\ 1 & 0 & 0 & -1 \\ 0 & 1 & -1 & 0 \end{pmatrix} \begin{pmatrix} V_5^- \Gamma_L \\ V_3^- \Phi_1 \\ V_2^- \Phi_2 \\ 0 \end{pmatrix} \quad (6.48b)$$

The solution of (6.48a) and (6.48b) for the output signal is:

$$V_5^- = V_1^+ \frac{1}{2}(\Phi_1 + \Phi_2) \quad (6.49)$$

The signal reflected back to the generator:

$$V_1^- = V_1^+ \frac{1}{4} \Gamma_L (\Phi_1 + \Phi_2)^2 \quad (6.50)$$

The signal dissipated in the load of hybrid 1:

$$V_4^- = V_1^+ \frac{1}{4} \Gamma_L (-\Phi_1^2 + \Phi_2^2) \quad (6.51)$$

The signal dissipated in the load of hybrid 2:

$$V_8^- = V_1^+ \frac{1}{2}(\Phi_1 - \Phi_2) \quad (6.52)$$

As we can see from equation (6.49), the modulator output signal is not dependent on the connected load. This means that the transfer function will be defined only by the controlling quantities (the phase-shifts of the phase-shifters) at any load condition, and that it will be stable. The modulator also does not produce any reflection caused by the phase and amplitude tuning at the input port. The difference between the incident and outgoing power is dissipated in the load of hybrid 2 (equation (6.52)). Since the modulator is fully reciprocal, the same is also valid for the reflected signal from the load (cavity).

The argument and phase of the transfer function can be calculated from (6.49):

$$\text{Arg} \left[\frac{V_5^-}{V_1^+} \right] = -\frac{\varphi_1 + \varphi_2}{2} \quad (6.53)$$

The magnitude of the transfer function – the amplitude modulation will be:

$$\text{Mag} \left[\frac{V_5^-}{V_1^+} \right] = \sqrt{\frac{1 + \cos(\varphi_1 - \varphi_2)}{2}} \quad (6.54)$$

Since formula (6.53) is identical to (6.20), and formula (6.54) is identical to (6.21), results are the same as plotted in Fig. 6.13 and Fig. 6.14.

6.3.2 Modulator with two quadrature hybrids working into an arbitrary load

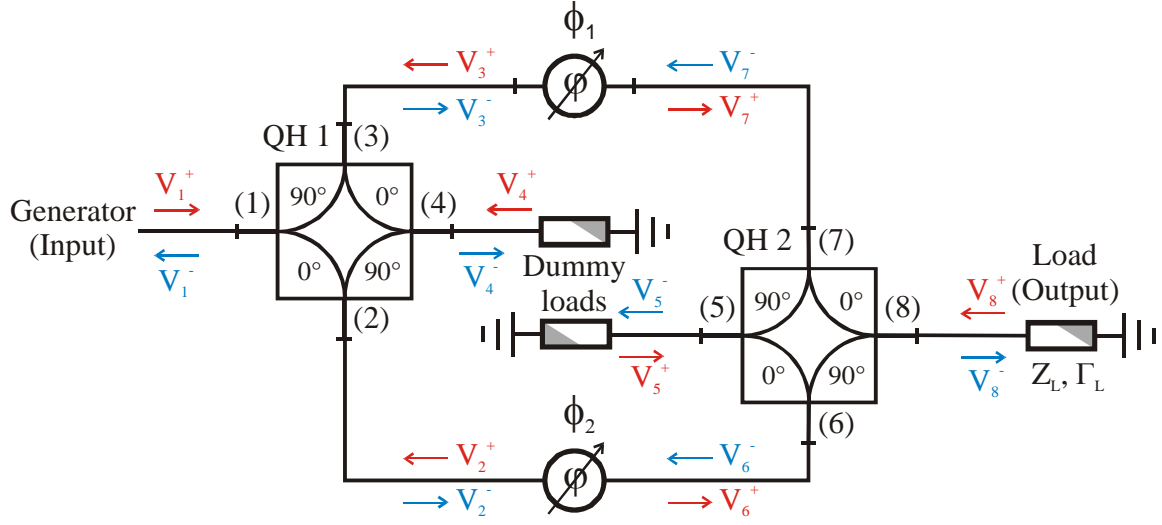


Fig. 6.20: Phase and amplitude modulator using two Magic Tees

Voltages (waves) in the structure are defined as:

$$V_2^+ = V_6^- \Phi_2 = V_6^- F_2 e^{-j\phi_2} \quad (6.55)$$

$$V_3^+ = V_7^- \Phi_1 = V_7^- F_1 e^{-j\phi_1} \quad (6.56)$$

$$V_4^+ = 0 \quad (6.57)$$

$$V_5^+ = 0 \quad (6.58)$$

$$V_6^+ = V_2^- \Phi_2 = V_2^- F_2 e^{-j\phi_2} \quad (6.59)$$

$$V_7^+ = V_3^- \Phi_1 = V_3^- F_1 e^{-j\phi_1} \quad (6.60)$$

$$V_8^+ = V_8^- \Gamma_L = V_8^- G e^{-j\gamma} \quad (6.61)$$

Using the scattering matrix of the quadrature hybrid (6.1), we obtain the final system of equations:

$$\begin{pmatrix} V_1^- \\ V_2^- \\ V_3^- \\ V_4^- \end{pmatrix} = \frac{1}{\sqrt{2}} \begin{pmatrix} 0 & j & 1 & 0 \\ j & 0 & 0 & 1 \\ 1 & 0 & 0 & j \\ 0 & 1 & j & 0 \end{pmatrix} \begin{pmatrix} V_1^+ \\ V_6^- \Phi_2 \\ V_7^- \Phi_1 \\ 0 \end{pmatrix} \quad (6.62a)$$

$$\begin{pmatrix} V_5^- \\ V_6^- \\ V_7^- \\ V_8^- \end{pmatrix} = \frac{1}{\sqrt{2}} \begin{pmatrix} 0 & j & 1 & 0 \\ j & 0 & 0 & 1 \\ 1 & 0 & 0 & j \\ 0 & 1 & j & 0 \end{pmatrix} \begin{pmatrix} 0 \\ V_2^- \Phi_2 \\ V_3^- \Phi_1 \\ V_8^- \Gamma_L \end{pmatrix} \quad (6.62b)$$

The solution of (6.62a) and (6.62b) for the output signal:

$$V_8^- = jV_1^+ \frac{1}{2}(\Phi_1 + \Phi_2) \quad (6.63)$$

The signal reflected back to the generator:

$$V_1^- = -V_1^+ \frac{1}{4}\Gamma_L(\Phi_1 + \Phi_2)^2 \quad (6.64)$$

The signal dissipated in the load of hybrid 1:

$$V_4^- = -jV_1^+ \frac{1}{4}\Gamma_L(\Phi_1^2 - \Phi_2^2) \quad (6.65)$$

The signal dissipated in the load of hybrid 2:

$$V_5^- = V_1^+ \frac{1}{2}(\Phi_1 - \Phi_2) \quad (6.66)$$

As can be seen from equation (6.63), the output signal of the modulator is not dependent on the connected load. This means that the transfer function will be defined only by the controlling quantities (phase-shifts of the phase-shifters) at any load condition, and will be stable, as it is for the modulator with two Magic Tees. The modulator also does not produce any reflection caused by the phase and amplitude tuning at the input port. The difference between the incident and outgoing power is dissipated in the load of hybrid 2 (equation (6.66)). As the modulator is fully reciprocal, the same also is valid for the reflected signal from the load (cavity).

The argument and phase of the transfer function can be calculated from (6.63):

$$\text{Arg} \left[\frac{V_8^-}{V_1^+} \right] = -\frac{\Phi_1 + \Phi_2}{2} + \frac{\pi}{2} \quad (6.67)$$

The magnitude of the transfer function – the amplitude modulation will be:

$$\text{Mag} \left[\frac{V_8^-}{V_1^+} \right] = \sqrt{\frac{1 + \cos(\Phi_1 - \Phi_2)}{2}} \quad (6.68)$$

Since formula (6.67) is identical to (6.34), and formula (6.68) is identical to (6.35), the results are the same as plotted in Fig. 6.17 and Fig. 6.18.

6.4 Transmission controlling capabilities

As calculated, the studied modulators allow independent control of the phase and amplitude of the passing signal. However, the tuning range of the whole device is related to the

individual full-scale phase-shift of the phase-shifters. The phase-shifters with a phase tuning range of 360° would allow total amplitude control from 0 to 100% with simultaneous phase-shift of $\pm 90^\circ$, which could compensate any cavity detuning situation assuming enough RF power provided at the input of the modulator. However, the full amplitude range is only available if there is a permanent ‘overpower’, even for a tuned cavity. Since for cost reasons the ‘overpower’ has to be limited, the cavity detuning has to be kept within corresponding limits. Having phase-shifters with the $\pm 60^\circ$ full-scale phase-tuning range was considered as a reasonable and affordable compromise. The phase-shift was defined for DC, keeping the range as high as possible for faster tuning speeds (see chapter 9). Fig. 6.21 shows the phase and amplitude tuning capabilities for such a modulator.

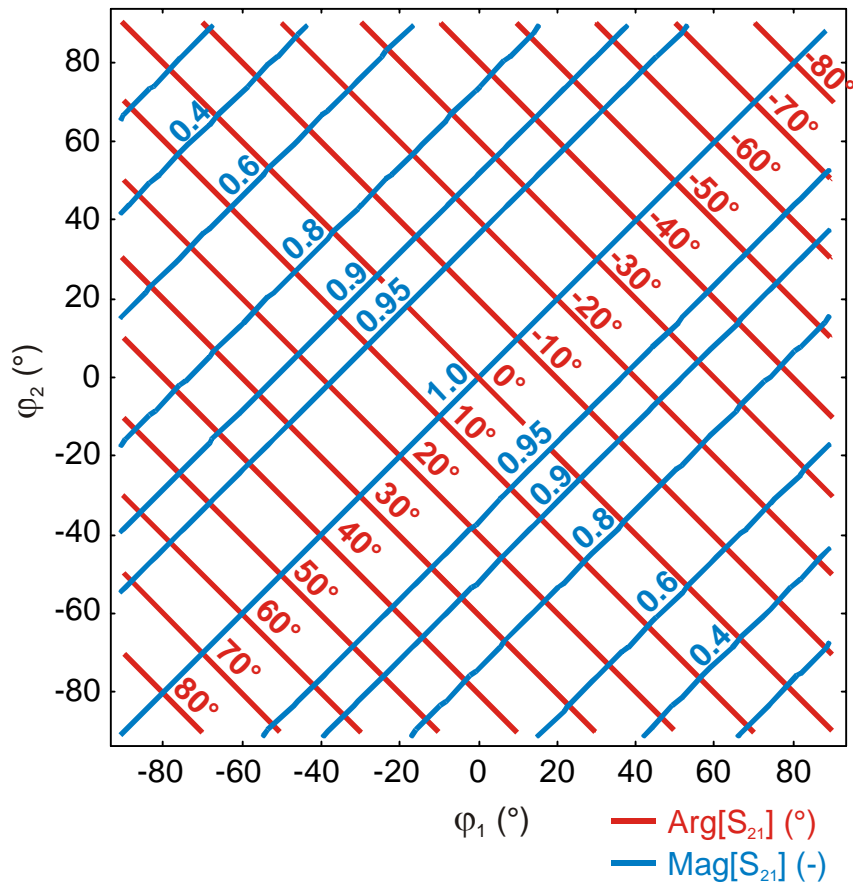


Fig. 6.21: Transmission controlling capabilities of the phase and amplitude tuner from chapter 6.3.1, phase-shifter’s full scale is $\pm 90^\circ$

To keep the modulator’s phase tuning capability symmetric, the range of both phase-shifters should have no mutual offset e.g. both must work from $-\varphi_{\max}$ to $+\varphi_{\max}$. The available transmission controlling capabilities for the phase and amplitude modulator equipped by the CERN fast ferrite phase-shifters are plotted in Fig. 6.22. The working point can lie only inside the region surrounded by the curves. The horizontal width between the branches at a

given (vertical) amplitude reduction factor shows the remaining available phase-shift of the modulator. For example no phase shift is available for -6dB amplitude reduction, or for guaranteed $\pm 45^\circ$ phase shift, only about -0.4dB of amplitude reduction is available.

As will be discussed later in chapter 9, the phase-shift depends on the phase tuning frequency, hence the three curves in Fig. 6.22 represent the controlling capabilities for DC to 400Hz (blue), 1kHz (red) and 1.5kHz (green) phase tuning speeds.

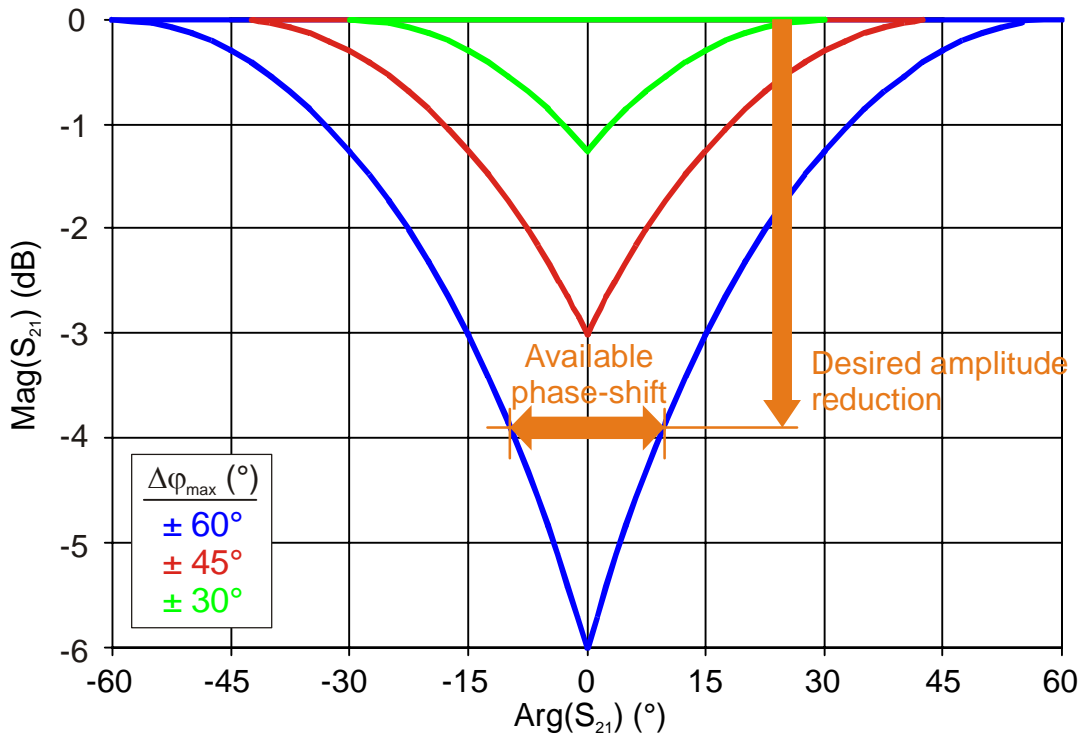


Fig. 6.22: Available working points for different full-scale differential phase-shift

6.5 Summary of the analysed modulators

Four different types of phase and amplitude modulators have been analyzed in the previous chapters. A summary of the properties of each structure is given in Table 6.1. As can be seen, with a matched load the overall properties of the modulators are – except for the fixed $\pi/2$ phase offset – the same.

Single hybrid modulators have an output signal that depends on the load reflection factor, which must be considered when designing the system. If the mismatch of the load is so large that the additionally induced standing wave dominates the primary wave, the system may become uncontrollable. This is exactly the case for the superconducting cavity which in the loading state before a beam arrives, reflects the full incident wave back to the generator. The

only safe solution is to introduce a small² circulator between the modulator and the cavity, assuring the modulator always ‘sees’ the matched load.

The single hybrid structure works with the reflective type of phase-shifters, which are in the domain of lower frequencies. The whole modulator is then quite compact in comparison to the double hybrid configuration.

Two hybrid modulators are more complex, but have some favourable properties. The output signal is independent of the output load, so amplitude and phase are only a function of the controlling quantities (i.e. the phase-shifts of both phase-shifters). The amplitude and/or phase modulation does not produce any reflections back to the generator. Also the structure uses the transmission type phase-shifters, which are easier and more reasonable to build at higher frequencies.

Hybrid(s)	Phase-shifters	Output amplitude*	Output phase*	Properties
Single Magic tee	Reflective type	$\sqrt{\frac{1 + \cos(\varphi_1 - \varphi_2)}{2}}$	$-\frac{\varphi_1 + \varphi_2}{2}$	<ul style="list-style-type: none"> - Output signal is dependent on the modulator load - Simple structure - For real application requires output circulator - Compact design
Single quadrature hybrid	Reflective type	$\sqrt{\frac{1 + \cos(\varphi_1 - \varphi_2)}{2}}$	$-\frac{\varphi_1 + \varphi_2}{2} - \frac{\pi}{2}$	<ul style="list-style-type: none"> - Suitable for lower frequencies - Amplitude regulation produces a mismatch at the input port
Two Magic tees	Transmission type	$\sqrt{\frac{1 + \cos(\varphi_1 - \varphi_2)}{2}}$	$-\frac{\varphi_1 + \varphi_2}{2}$	<ul style="list-style-type: none"> - Output signal is not dependent on the modulator load
Two quadrature hybrids	Transmission type	$\sqrt{\frac{1 + \cos(\varphi_1 - \varphi_2)}{2}}$	$-\frac{\varphi_1 + \varphi_2}{2} - \frac{\pi}{2}$	<ul style="list-style-type: none"> - More complex structure - Requires two dummy loads - Bulky at lower frequencies

* for matched output

Table 6.1: Comparison of different phase and amplitude modulator structures

² Small in this context means that the circulator has to handle only the power of one cavity, not the full transmitter power for the whole group of cavities.

7

High frequency and microwave phase shifting devices

Chapter 7 gives an introduction to phase shifting devices. Reflective and transmission type phase-shifters are introduced. The parameters and capabilities of the different structures are compared.

7.1 Introduction to the phase-shifters and basic terms

Phase-shifters are devices permitting controlled variation of the phase of a passing RF signal. The phase-shift may be controlled either mechanically or electrically. Mechanical phase-shifters usually use moving plungers, short circuits, rotating dielectric slabs inside the waveguide or rotating inner conductor of the strip-line type transmission line. Electrically controlled phase-shifters use changes in the RF material properties (e.g. permeability of the ferrite material or permittivity of the dielectric material) to control the phase of the RF signal. Applications of phase-shifting devices are very wide, including phased antenna arrays, dynamic RF power division, impedance matching, signal modulation, circulators and isolators, scientific instruments and many others.

Phase-shifters may be classified as:

- single port/two port
- digital/analog
- reciprocal/nonreciprocal

The single port, so called reflective phase-shifters change the phase of the reflection coefficient Γ (equal to the S_{11}) at its port. From the principle of operation, the wave is passing the active part of the single-port device twice (non-resonant types) or multiple times (resonant types). This brings an advantage of shorter structure in comparison to the two-port devices.

The S matrix (in this case only one dimensional) of an ideal lossless single port phase-shifter device can be written as:

$$[S] = \left[e^{-j(\varphi_0 + \Delta\varphi)} \right] \quad (7.1)$$

where φ_0 is the ‘residual’ or ‘steady’ phase-shift (when the device is not energized) and $\Delta\varphi$ is the phase-shift obtained by the tuning.

The negative sign of the exponent in (7.1) means that the wave is delayed by passing the phase-shifter. A positive value of the $\Delta\varphi$ then increases the phase-shift and accordingly the delay.

The two port phase-shifters – so called transmission type – change the phase of the propagating wave from one port to the other. Depending on the construction, the phase-shift may be a reciprocal or nonreciprocal.

The S matrix of an ideal, lossless and reciprocal two port phase-shifter can be written as:

$$[\mathbf{S}_{\text{reciprocal}}] = \begin{bmatrix} 0 & e^{-j(\varphi_0 + \Delta\varphi)} \\ e^{-j(\varphi_0 + \Delta\varphi)} & 0 \end{bmatrix} \quad (7.2)$$

The S matrix of an ideal, lossless and nonreciprocal two port phase-shifter can be written as:

$$[\mathbf{S}_{\text{non-reciprocal}}] = \begin{bmatrix} 0 & e^{-j\varphi^-} \\ e^{-j\varphi^+} & 0 \end{bmatrix} \quad (7.3)$$

where φ^+ is the phase-shift for the forward wave (propagating from port 1 to port 2), and φ^- is the phase-shift for the reflected wave (propagating from port 2 to port 1). Nonreciprocal devices are usually designed such that the phase-shift for the reflected wave is much lower than for the forward one. Then the S matrix may be then written as:

$$[\mathbf{S}_{\text{non-reciprocal}}] = \begin{bmatrix} 0 & 1 \\ e^{-j\varphi^+} & 0 \end{bmatrix} = \begin{bmatrix} 0 & 1 \\ e^{-j(\varphi_0 + \Delta\varphi)} & 0 \end{bmatrix} \quad (7.4)$$

The meaning of the quantities is the same as for formulas (7.2) and (7.3).

Analog phase-shifters provide a continuous variation of the phase-shift as a function of the tuning quantity. In contrast digital phase-shifters provide fixed step changes in the phase variations. Digital phase shifters consist of a number of elements, each providing a fixed phase-shift, combined in series to obtain a full tuning range.

The conventional figure of merit – FM (°/dB) – describes the performance of the phase-shifters by relating the maximum phase-shift $\Delta\varphi_{\text{max}}$ and the highest insertion loss \mathbf{IL}_{max} which is encountered when the phase-shift is varied from zero to $\Delta\varphi_{\text{max}}$

$$\text{FM} = \frac{\Delta\varphi_{\text{max}}}{\mathbf{IL}_{\text{max}}} \quad (7.5)$$

7.2 Ferrite phase-shifters

Most linear ferrite devices operate with biasing magnetic fields H_{DC} either perpendicular or parallel to the wave propagation direction. These two geometries are called transverse and longitudinal magnetizations. To simplify the analysis of both of the cases, slightly different matrices for the $[\mu]$ tensor are used [62]:

$$[\mu]_{LONG} = \mu_i \begin{bmatrix} \tilde{\mu} & -j\tilde{\kappa} & 0 \\ j\tilde{\kappa} & \tilde{\mu} & 0 \\ 0 & 0 & 1 \end{bmatrix} \quad [\mu]_{TRANS} = \begin{bmatrix} \mu & 0 & j\kappa \\ 0 & \mu_i & 0 \\ -j\kappa & 0 & \mu \end{bmatrix} \quad (7.6)$$

In the case of longitudinal magnetization, propagation through the (infinite) ferrite medium is governed by the eigenvalues of $[\mu]$, respectively $\mu_{\pm} = \mu \mp \kappa$. Then the normalized propagation factor is

$$\Gamma_{\pm} = \frac{\beta_{\pm}}{\beta_0} = \sqrt{\varepsilon\mu_{\pm}} \quad (7.7)$$

where the β_0 is the propagation constant in the air $\beta_0 = \omega\sqrt{\varepsilon_0\mu_0}$.

Phase-shift is then proportional to

$$\Delta\varphi \approx \frac{1}{2}(\Gamma_+ + \Gamma_-) \quad (7.8)$$

In the case of transverse magnetization, the biasing field H_0 may be parallel either to the H or E vectors of the electromagnetic wave. The normalized propagation constants are

$$\Gamma = \sqrt{\varepsilon\mu_i} \quad \text{and} \quad \Gamma = \sqrt{\varepsilon\mu_e} \quad \text{respectively} \quad (7.9)$$

The effective permeability $\mu_e = (\mu^2 - \kappa^2)/\mu$ controls interaction of the ferrite and microwave signal. Typical curves for the μ_{\pm} , and μ_e , together with the typical operating regions of the common ferrite devices are shown in Fig. 7.1. σ stands for the normalized biasing field $\sigma = H_0/H_{res}$. The meaning of the quantities is explained in the ‘‘Used symbols’’ section.

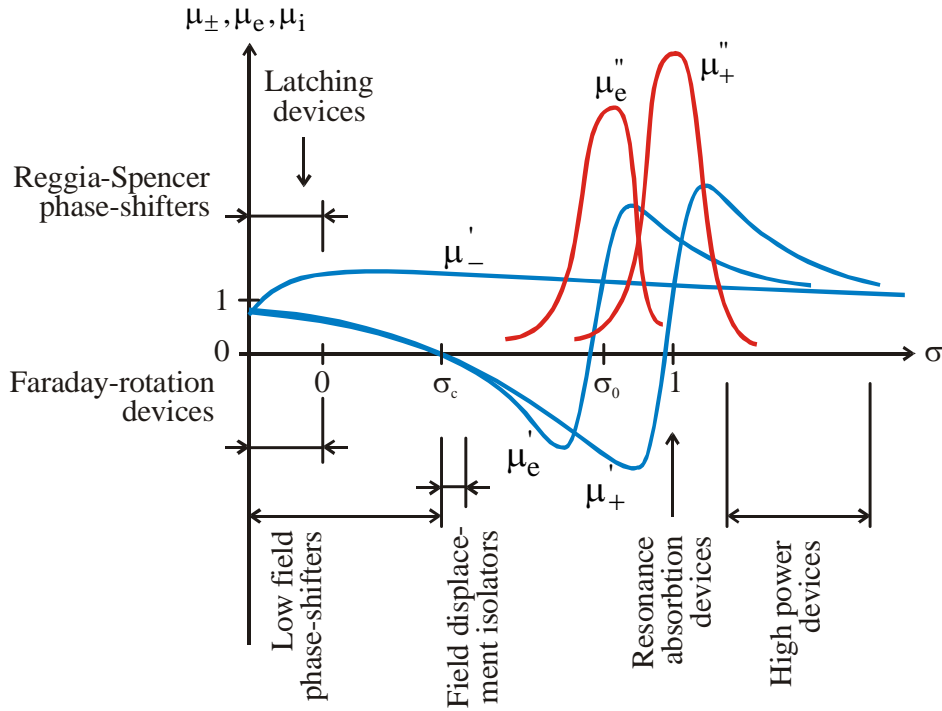


Fig. 7.1: Typical curves of the μ_{\pm} and μ_e , and operating regions of the common ferrite devices

Schematic drawings of the different ferrite phase-shifter devices are shown in Fig. 7.2, Fig. 7.3, Fig. 7.4, Fig. 7.5 and Fig. 7.6. Comparison of the parameters for different phase-shifter configurations is given in the table 7.1.

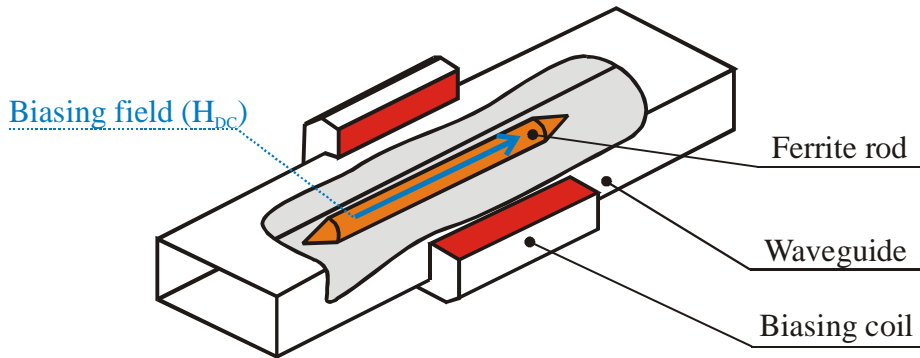


Fig. 7.2: Reggia-Spencer type of ferrite phase-shifter

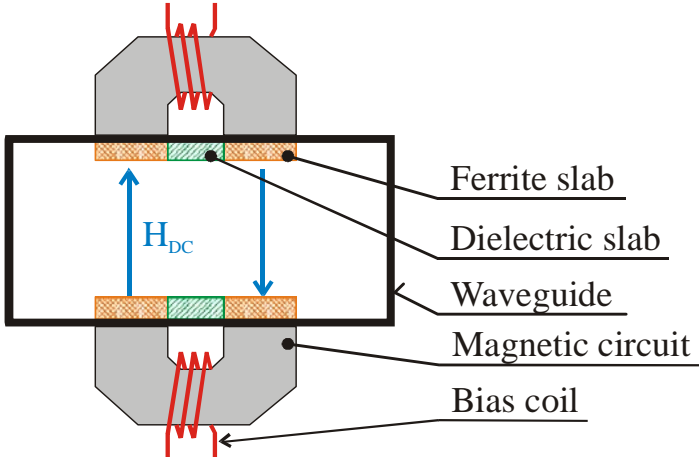


Fig. 7.3: H-plane differential phase-shifter

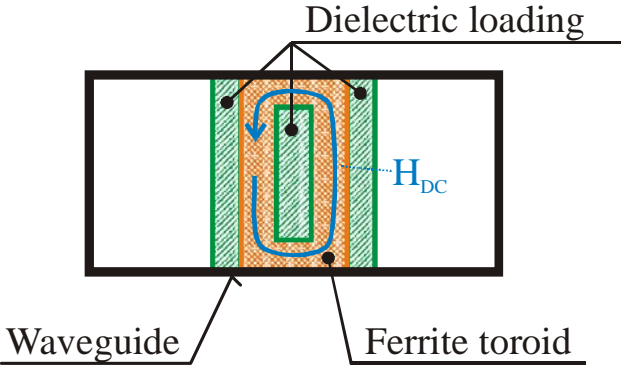


Fig. 7.4: Waveguide latching phase-shifter

Type of phase-shifter	Analog	Latching	Typical operating frequency (GHz)	Figure of merit ($^{\circ}$ /dB)	Bandwidth	Power capability	Phase tuning speed	Power needed for tuning	Compact design	
Coaxial, below resonance	Yes		3	Poor	Average	Average	Average	Average	Average	
Coaxial, above resonance	Yes		0.5-1.5	Excellent	Average	High	Average	Average	Average	High power applications
Reggia-Spencer	Yes		3-35	Excellent	Low	Low	Average	Average	Yes	
Reggia-Malk	Yes	Yes	9	Poor	Low	Low	High	Low	Yes	
Twin slabs in waveguide	Yes		9	Average	Low	Average	Low	High	No	
Rotating field	Yes		9	Average	Low	Low	n/a	High	No	Periodically variable phase-shift for SSB modulation
Single slab in waveguide			3-15	Average	Average	High	n/a	n/a	Average	Fixed field devices for four port circulators
Twin slabs in waveguide			3-15	Average	Average	High	n/a	n/a	Average	
Toroid in waveguide		Yes	3-10	Average	High	Average	High	Low	Yes	Latching digital devices for phased antenna arrays applications
Toroid in strip-line		Yes	3-5	Average	Average	Low	High	Low	Yes	
Slow-wave structure		Yes	1-3	Poor	Average	Low	High	Low	Yes	
Reciprocal										
Non-reciprocal										

Table 7.1: Comparison of the different phase-shifter configurations

As we can see from the Table 7.1, several configurations are possible. However, for the high-power and high phase tuning speed applications, only some of them are suitable. For a lower average RF power, a two slab waveguide configuration is applicable. But when moving towards the high average power region, only the coaxial structures are suitable.

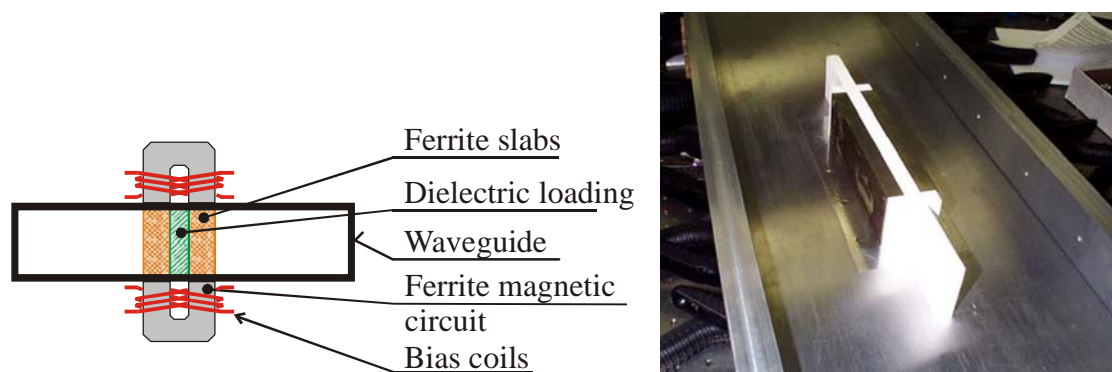


Fig. 7.5: Two-slab waveguide phase-shifter by Y. Kang

In the Chicago's Argonne National Laboratory a two-slab design shown in Fig. 7.5 was built and tested by Kang [63]. The ferrite slabs are placed in a hollow waveguide where the RF magnetic fields are circularly polarized in the plane orthogonal to the external magnetic bias field. Using the circularly polarized magnetic fields requires that the orthogonal biased ferrite slabs be located at around 1/3 and 2/3 of the width in the rectangular waveguide. Alternatively, a dielectric substrate could be used. The ferrites work below the resonance point. The phase-shifter is nonreciprocal and offers a phase-shift larger than 40° per 150mm at 805MHz operating frequency.

For the CERN application, a coaxial type phase-shifter working above the gyromagnetic resonance was chosen (see Fig. 7.6).

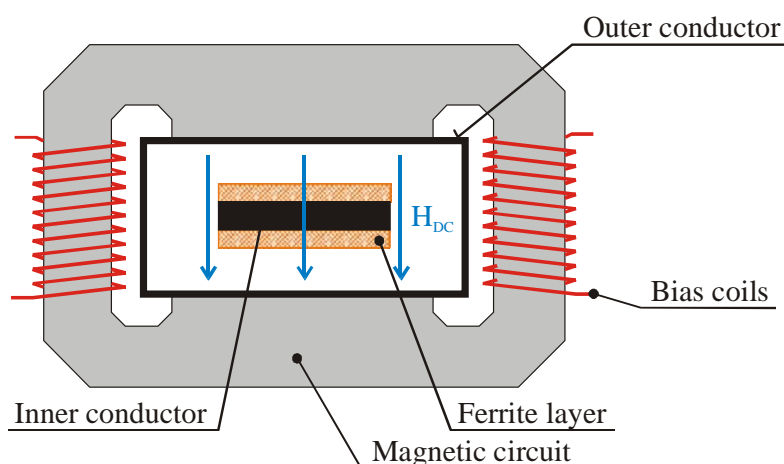


Fig. 7.6: Strip-line coaxial phase-shifter for high power application

8

Coaxial ferrite phase-shifter working above ferrite's gyromagnetic resonance

In this chapter a coaxial phase-shifter working above the ferrite's gyromagnetic resonance is discussed. The ferrite loaded strip-line structure with its variable impedance and propagation constant properties is introduced. Use of such a line in different phase-shifter configurations is shown and various configurations of a reflection type and transmission type of the phase-shifter are analysed.

8.1 Strip transmission lines

The term strip-line was originally used to describe any planar transmission line based on strip conductors, including a microstrip line. Its meaning has come in recent years to be more specific and now it generally refers to a structure having a conducting strip embedded in a dielectric medium between the two ground planes as shown in Fig. 8.1 (left). In 1936 Wheeler developed a planar transmission line (two coplanar strips), which could be rolled up, and in 1942 a strip-line like structure [51]. The first use of a “flat strip coaxial transmission line” was by Rumsey and Jamieson during the second world war [52]. In 1949 Barrett applied this new structure to printed circuit boards and now strip-line is one of the most popular transmission line structures [52].

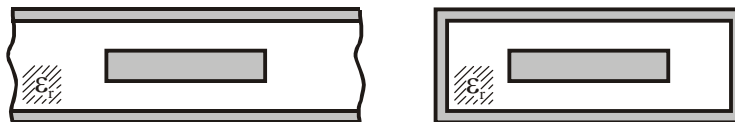


Fig. 8.1: General strip-line structure (left) and a real strip-line with the side walls (right)

The strip-line has very favorable properties for use in the field of high power RF systems. It has reasonable attenuation and since the whole structure is surrounded by the metallic shielding, RF radiation out of the line is negligible. When using a hollow internal conductor, water cooling is easily applicable. Strip-line transmission line is easy to manufacture and hence cheap.

For some applications another useful feature is that by rotating the center conductor, the characteristic impedance of the strip-line can be varied.

8.2 Impedance of the general transmission line

To characterize the general transmission line, the RLCG lumped model is one of the basic techniques well known from the circuit theory [65].

A transmission line is fully electrically characterized by the distributed resistance R (Ohm/m), the distributed inductance L (H/m), the distributed capacity C (F/m), the distributed conductance G (S/m) and the line length l (m) (see Fig. 8.2).

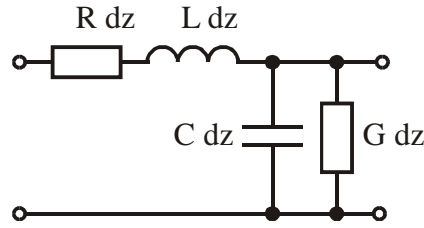


Fig. 8.2: The RLCG lumped model of the transmission line

Impedance of the transmission line is:

$$Z_0 = \frac{v(z,t)}{i(z,t)} = \sqrt{\frac{R + j\omega L}{G + j\omega C}} \quad (8.1)$$

and the propagation constant as:

$$\gamma = \alpha + j\beta = \sqrt{(R + j\omega L)(G + j\omega C)} \quad (8.2)$$

where α is the attenuation constant and β is the phase constant. In the case of the loss-less transmission line, the series resistance and the parallel conductance can be neglected reducing (8.1) and (8.2) to the form:

$$Z_0 = \frac{v(z,t)}{i(z,t)} = \sqrt{\frac{L}{C}} \quad (8.3)$$

$$\beta = \omega \sqrt{LC} \quad (8.4)$$

Propagation velocity in such a line will be:

$$v_p = \frac{1}{\sqrt{LC}} \quad (8.5)$$

8.3 Impedance of the ideal strip-line transmission line

For the symmetrical strip-line the TEM-mode characteristic impedance is readily found from the distributed capacitance with the latter determined by conformal mapping techniques [53] [55]. In the 1950s, Wheeler calculated the impedance of the strip-line with a centered internal conductor and ground planes extending to infinity [56].

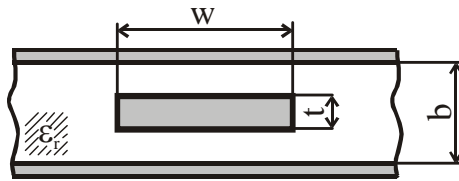


Fig. 8.3: Strip-line structure with infinite ground planes.

The equations are:

$$Z = \frac{Z_0}{2\pi\sqrt{\epsilon_r}} \ln \left[1 + \frac{4(b-t)}{\pi w'} \left(\frac{8(b-t)}{\pi w'} + \sqrt{\left[\frac{8(b-t)}{\pi w'} \right]^2 + 6.27} \right) \right] \quad (8.6)$$

where:

$$w' = w + \frac{\Delta w}{t} t \quad (8.7)$$

$$\frac{\Delta w}{t} = \frac{1}{\pi} \ln \left[\frac{e}{\sqrt{\left(\frac{1}{2(b-t)/t+1} \right)^2 + \left(\frac{1/4\pi}{w/t+1.1} \right)^m}} \right] \quad (8.8)$$

$$m = \frac{6}{3 + \frac{2t}{b-t}} \quad (8.9)$$

Nevertheless, formula 8.6 gives results with reasonable precision for only the most commonly used strip-lines with dimensions t/b varying from 0 to 0.5 and w/b varying from 0.1 to 10. The impedance then usually lies in the range from 15 to 200 Ohm.

8.4 Impedance of the shielded strip-line (rectangular coaxial line)

When the strip-line structure is completely closed between the conductive walls (not only the top and bottom ground planes) it is necessary to correct the formulas for the effect of the sidewalls at a finite distance from the center conductor [57]. This configuration also brings an intermediate step between the strip-line structure and the round coaxial line – the shielded strip-line, or the rectangular coaxial line.

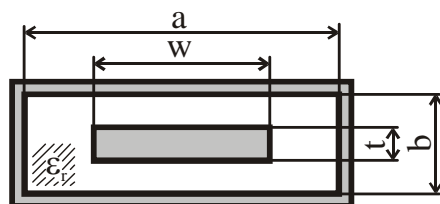


Fig. 8.4: Shielded strip-line structure

Chen [58] calculated the impedance of the shielded strip-line, even for very wide ($w/b \gg 1$) lines like the one used in the phase-shifter device. Hence for the impedance we can write:

$$Z = \frac{Z_0}{4\sqrt{\epsilon_r}} \frac{1}{\frac{w/b}{1-t/b} + \frac{2}{\pi} \text{Ln}\left(\frac{1}{1-t/b} + \text{Coth}\frac{\pi a}{2b}\right)} \quad (8.10)$$

With the dimensions of line chosen to be $a=180$ mm, $w=150$ mm, $b=20$ mm, $t=11$ mm and for an air filled line with $\epsilon_r=1$, we obtain $Z_0=5.41$ Ohm. This agrees very well with the result $Z_0=5.31$ Ohm obtained by the finite element method calculation.

The rectangular coaxial line also offers another advantage. When turning the inner conductor [59], the impedance of such a line can be varied (Fig. 8.5).

As will be shown later, variable impedance lines are frequently used in phase-shifting devices.

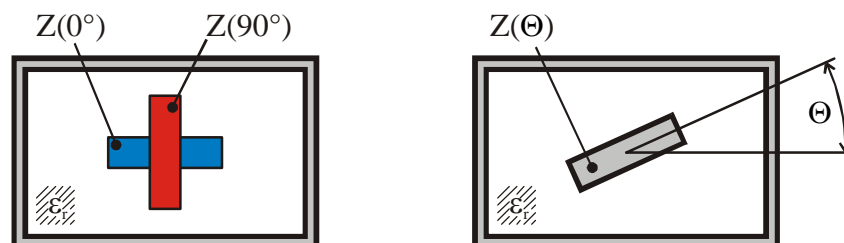


Fig. 8.5: Rotation of the center conductor

Using the impedance of the line at position $Z(0^\circ)$ and $Z(90^\circ)$ the impedance of the tilted line can be calculated:

$$Z(\Theta) = \frac{Z(0^\circ) [1 + \cos(2\Theta)] + Z(90^\circ) [1 - \cos(2\Theta)]}{2} \quad (8.11)$$

An example of the impedance changing capabilities for $Z(0^\circ)=55$ Ohm and $Z(90^\circ)=45$ Ohm is shown in Fig. 8.6.

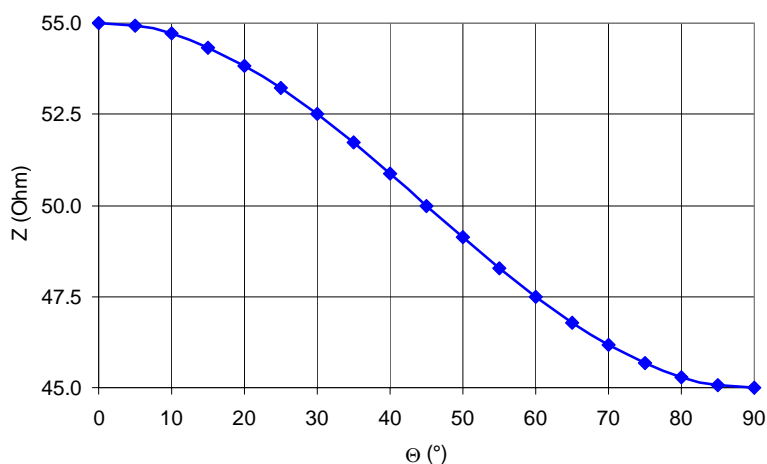


Fig. 8.6: Impedance variation provided by tilting of the inner conductor

8.5 Impedance of the ferrite loaded strip-line

Since it is difficult, or even impossible, to calculate the electrical parameters of the ferrite loaded strip-line analytically, as it was done for the previous cases, a different method of the impedance determination must be used.

An increasing availability of computer resources coupled with a desire to model more complex electromagnetic problems has resulted in a wave of interest in finite element methods for solving electromagnetic problems [60].

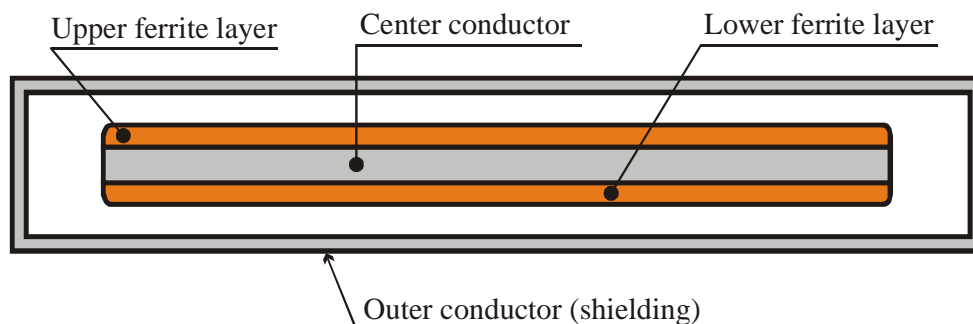


Fig. 8.7: High power, very low impedance, ferrite loaded strip-line structure

Consider the structure shown in Fig. 8.7. The first step in finite-element analysis is to divide the geometry into a number of small homogeneous elements. An example of a finite-element model of the strip-line structure is shown in figure Fig. 8.8. The model contains information about the device geometry, material constants, excitations and boundary constraints. The elements can be small where geometric details are important and much larger elsewhere. In each finite element, a simple (often linear) variation of the field quantity is assumed. The corners of the elements are called nodes. The goal of the finite-element analysis is to determine the field quantities at the nodes.

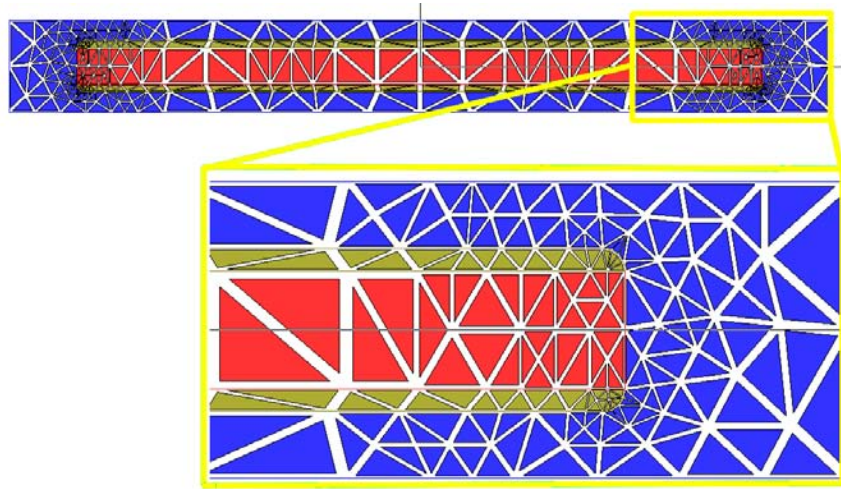


Fig. 8.8: Mesh of the finite element model for the structure shown in the Fig. 8.7

Most finite element methods use variational techniques. Variational methods work by minimizing or maximizing an expression that is known to be stationary about the true solution. Generally, finite-element analysis techniques solve for the unknown field quantities by minimizing an energy functional. The energy functional is an expression describing all the energy associated with the configuration being analyzed. For 3-dimensional, time-harmonic problems this function may be represented as:

$$EF = \frac{1}{2} \iiint_V \left(\mu |\mathbf{H}|^2 + \varepsilon |\mathbf{E}|^2 - \frac{\mathbf{J} \cdot \mathbf{E}}{j\omega} \right) dv \quad (8.12)$$

The first two terms in the integrand represent the energy stored in the magnetic and electric fields and the third term is the energy dissipated (or supplied) by conduction currents.

In order to obtain a unique solution, it is necessary to constrain the values of the field at all boundary nodes. A major weakness of the finite element method is that it is relatively difficult to model open configurations (i.e. configurations where the fields are not known at every

point on a closed boundary). Various techniques such as ballooning and absorbing boundaries are used in practice to overcome this deficiency.

The major advantage that finite element methods have over other electromagnetic modeling techniques stems from the fact that the electrical and geometric properties of each element can be defined independently. This permits the problem to be set up with a large number of small elements in regions of complex geometry and fewer, larger elements in relatively open regions. Thus it is possible to model configurations that have complicated geometries and many arbitrarily shaped dielectric regions in a relatively efficient manner.

8.6 Externally controlled, variable impedance ferrite loaded strip-line

As already mentioned, to control the transmission line parameters, a ferrite material layer is used. The externally controllable parameter is the permeability of the ferrite material. Since the inductance of the transmission line (and thus the permeability of the material) appears in the formulas (8.3) and (8.4) both the characteristic impedance and the phase propagation constant change. In this sub-chapter the electrical and RF parameters of the strip-line which are interesting for the study of the phase-shifter are evaluated.

The ferrite material used for CERN's design is one of AFT's low loss ferrite garnets [61]. The ferrite material is biased to operate above the gyromagnetic resonance. Then the material can be described only by the scalar values of the permeability, significantly simplifying further analysis. Values of μ' and μ'' as a function of the bias magnetic field are listed in the Table 8.1 and plotted in the Fig. 8.9 (full table and graphs are in the Appendix A).

B [Gauss]	μ'	μ''	$\tan \delta$
1560	4.43	0.049	0.0111
1600	4.20	0.044	0.0105
1700	3.62	0.031	0.0086
1800	3.09	0.019	0.0061
1900	2.75	0.011	0.0040
1992	2.53	0.0075	0.0030
2100	2.35	0.0058	0.0025
2280	2.12	0.005	0.0024

Table 8.1: Ferrite material permeability as a function of the bias field. Bold items are measured values, the rest are extrapolated from the measured curve.

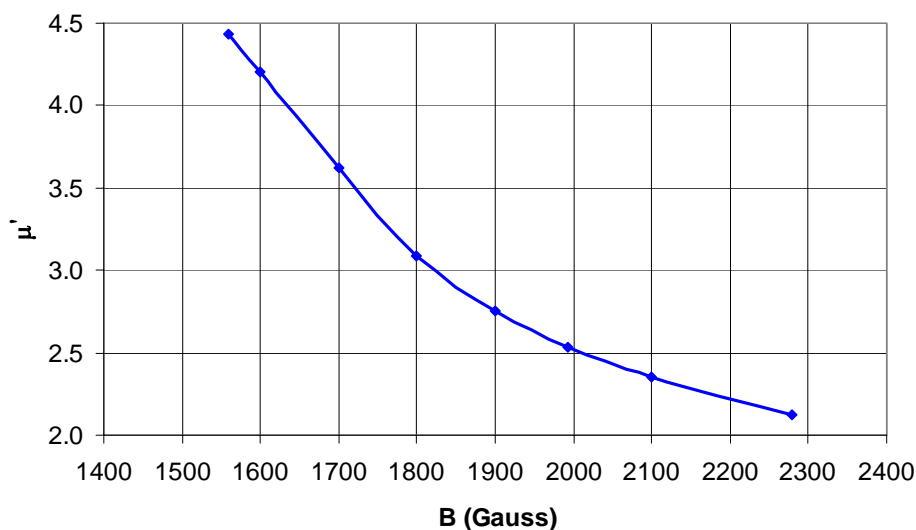


Fig. 8.9: Real part of the permeability as a function of the bias field

The variable impedance line used in the ferrite phase-shifter is sketched in Fig. 8.10. To define the precise geometry, RF power and voltage handling and thermal considerations must be taken into account. The peak RF power (voltage) to which the line is exposed determines its minimal height (sum m and f , line height b , Fig. 8.10). A maximum tolerable power loss per unit area, and hence the thermal dissipation, determines the minimal area of the ferrite region (strip width and length, Fig. 8.10).

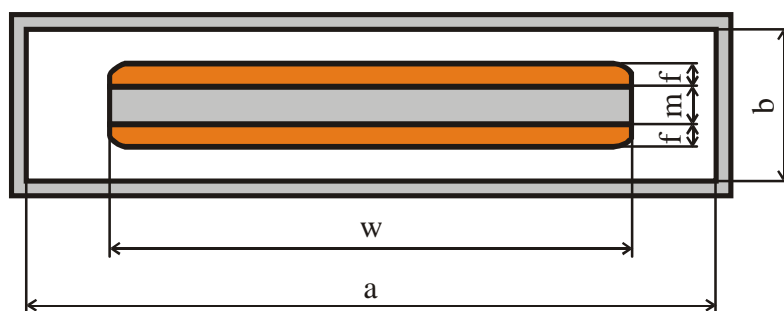


Fig. 8.10: High power, ferrite loaded strip-line structure

By using the Maxwell 2D code [54], a series of simulations were run in order to obtain the distributed line parameters as well as the electric and thermal loading for such a line. The theoretical analysis of the line and its various configurations are valid generally. However as the phase-shifters will be used in the SPL machine, constraints are placed on the operating parameters. The following analysis is adapted to the cases applicable to the SPL machine.

The results of the line impedance calculations when varying the internal conductor width (w), while ferrite thickness is remaining constant, are given in Table 8.2 and plotted in Fig. 8.11.

w (mm)	$B_{DC}=1700$ Gauss		$B_{DC}=2100$ Gauss		Rel. change of β (%)
	Z (Ohm)	v/c (-)	Z (Ohm)	v/c (-)	
10	12.33	0.183	11.85	0.191	4.08
20	7.863	0.159	7.418	0.169	6.01
30	5.974	0.153	5.572	0.164	7.21
40	4.655	0.144	4.315	0.155	7.87
50	3.910	0.142	3.607	0.154	8.39
60	3.336	0.139	3.069	0.151	8.71
70	2.895	0.136	2.655	0.148	9.05
80	2.556	0.134	2.339	0.146	9.30
90	2.301	0.133	2.103	0.145	9.41
100	2.090	0.132	1.906	0.144	9.63
110	1.916	0.131	1.746	0.144	9.71
120	1.768	0.130	1.610	0.143	9.81
130	1.652	0.131	1.503	0.143	9.94
140	1.537	0.130	1.397	0.143	9.99
150	1.434	0.129	1.303	0.142	10.12

Table 8.2: Ferrite loaded strip-line impedance variation depending on the width of the internal conductor ($a=180\text{mm}$, $b=20\text{mm}$, $t=8\text{mm}$, $f=1.5\text{mm}$)

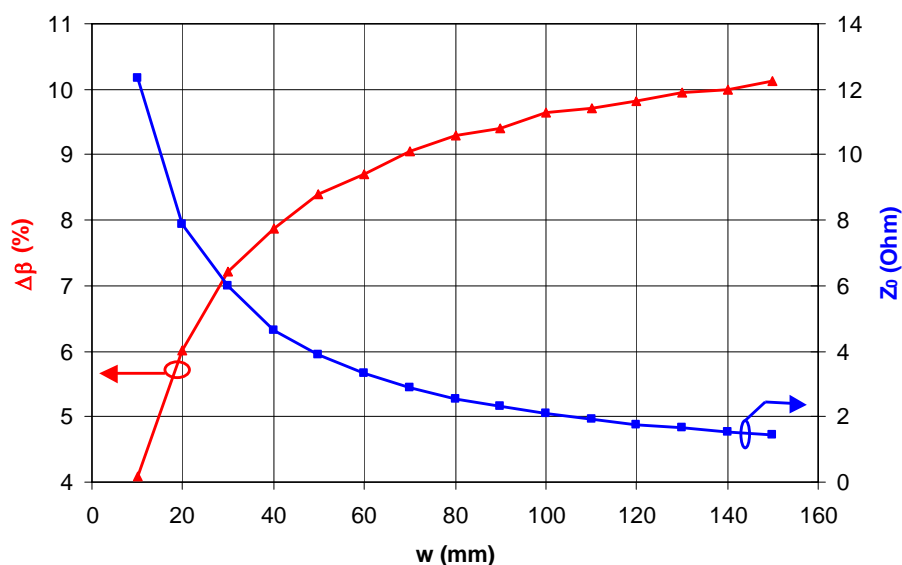


Fig. 8.11: Impedance variation and relative phase constant change as a function of the strip-line width.

As can be seen from Fig. 8.11, the highest relative change of the propagation factor (and hence the phase constant) is available for very low-impedance lines, where the inductance of the line is dominant. In order to maintain reasonable physical dimensions of the phase-shifters, at lower frequencies low impedance lines are mostly used. At higher frequencies,

higher impedance lines provide sufficient phase-shift, lower losses and less sensitivity to the higher order modes propagating in the strip-line structure.

Three different cases were studied and analysed for the “wide” line, which is suitable at 352MHz. The ferrite layer thickness was changed in three steps 1.5-2-2.5mm and the line impedance and propagation factor was calculated. Comparison for the different ferrite thicknesses is shown in the Table 8.3, and detailed results are given in the Appendix B.

t (mm)	f (mm)	$B_{DC}=1700\text{Gauss}$		$B_{DC}=2100\text{Gauss}$		Rel. change of β (%)
		Z (Ohm)	v/c (-)	Z (Ohm)	v/c (-)	
8	1.5	1.434	0.129	1.303	0.142	10.09
7	2.0	1.786	0.137	1.601	0.153	11.53
6	2.5	2.131	0.143	1.892	0.161	12.68

Table 8.3: impedance variation of the ferrite loaded strip-line depending on the thickness of the ferrite layer ($a=180\text{mm}$, $b=20\text{mm}$, $w=150\text{mm}$)

B (Gauss)	L (H/m)	C (F/m)	Z_0 (Ohm)	β (rad/m)	v_p (m/s)	v_p/c
1560	4.0660E-08	1.8030E-08	1.502	59.853	36933329	0.1231
1700	3.7097E-08	1.8030E-08	1.434	57.170	38666311	0.1289
1800	3.4434E-08	1.8030E-08	1.382	55.080	40133626	0.1338
1900	3.2690E-08	1.8030E-08	1.347	53.667	41190274	0.1373
1992	3.1549E-08	1.8030E-08	1.323	52.722	41928501	0.1398
2100	3.0593E-08	1.8030E-08	1.303	51.917	42578573	0.1419
2280	2.9391E-08	1.8030E-08	1.277	50.887	43440514	0.1448

Table 8.4: Ferrite thickness $f=1.5\text{mm}$, metal conductor thickness $m=8\text{mm}$

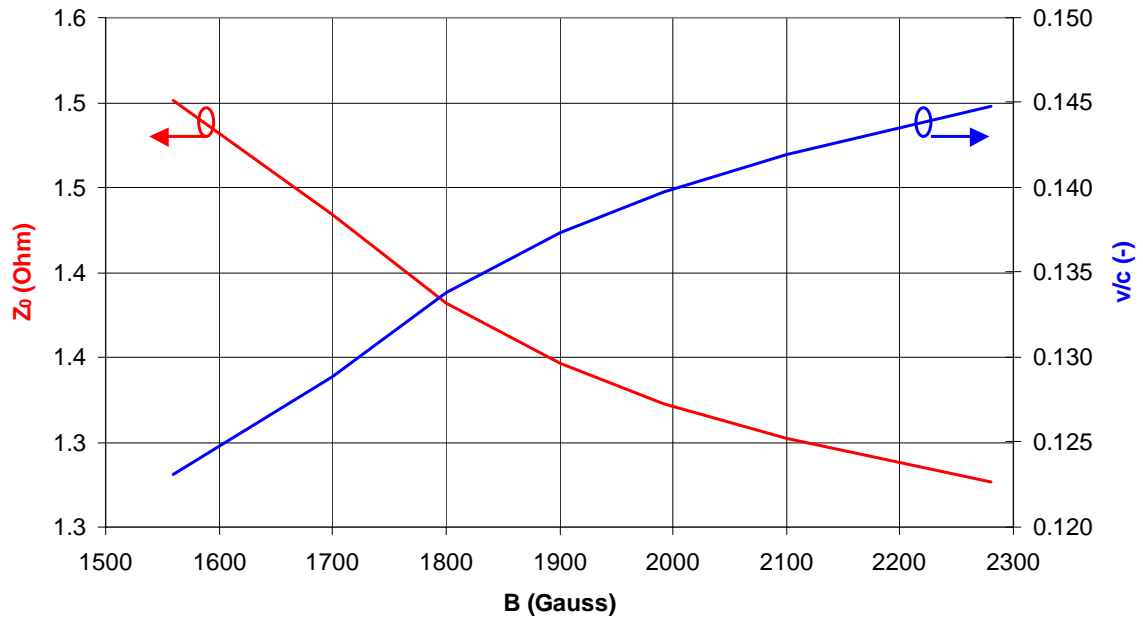


Fig. 8.12: Impedance and propagation factor variation as a function of the bias field, 1.5/8mm structure

8.7 Reflection coefficient of the shorted line connected to an unmatched port – coaxial phase-shifter type one

8.7.1 Definition of the terms

Voltage reflection coefficient

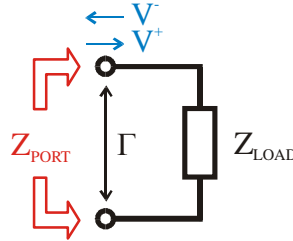


Fig. 8.13: Voltage reflection coefficient definition

The voltage reflection coefficient Γ on the transmission line is generally defined using the voltages of the forward (V^+) and reflected (V^-) waves [68] as

$$\Gamma = \frac{V^-}{V^+} \quad (8.13)$$

For the single port device, the voltage reflection coefficient Γ is equal to the S_{11} parameter.

If a load is connected to the end of transmission line (or directly to the port), the voltage reflection coefficient can be evaluated using the transmission line (or port) impedance:

$$\Gamma = \frac{Z_{\text{LOAD}} - Z_{\text{PORT}}}{Z_{\text{LOAD}} + Z_{\text{PORT}}} \quad (8.14)$$

Where Z_{PORT} is the port impedance and Z_{LOAD} is impedance of the connected element.

Voltage reflection coefficient along the transmission line

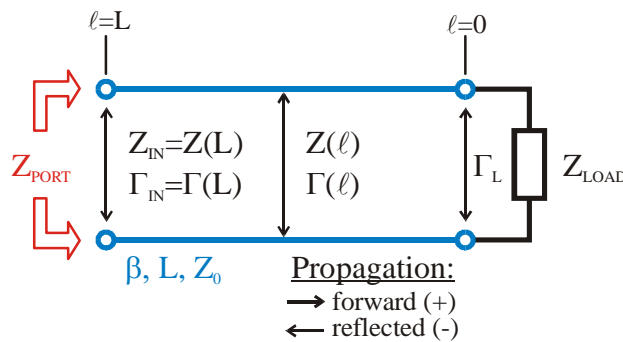


Fig. 8.14: Voltage reflection coefficient along the transmission line

As the forward and reflected waves are propagating along the transmission line, the voltage reflection coefficient is defined at every point on the line as well. Its transformed value is¹⁰:

$$\Gamma(\ell) = \frac{V^- e^{-j\beta\ell}}{V^+ e^{+j\beta\ell}} = \frac{V^-}{V^+} e^{-j2\beta\ell} = \Gamma_L e^{-j2\beta\ell} \quad (8.15)$$

Impedance transformation along the transmission line

The impedance seen at the beginning of a general transmission line, terminated by impedance Z_{LOAD} is:

$$Z_{IN} = Z_0 \frac{Z_{LOAD} \cosh(\gamma\ell) + Z_0 \sinh(\gamma\ell)}{Z_0 \cosh(\gamma\ell) + Z_{LOAD} \sinh(\gamma\ell)} = Z_0 \frac{Z_{LOAD} + Z_0 \tanh(\gamma\ell)}{Z_0 + Z_{LOAD} \tanh(\gamma\ell)} \quad (8.16)$$

where Z_0 is the impedance of the transmission line, Z_{LOAD} is the termination impedance, γ is the propagation constant and ℓ is length of the transmission line.

For a lossless transmission line, formula (8.16) reduces to:

$$Z_{IN} = Z_0 \frac{Z_{LOAD} \cos(\beta\ell) + jZ_0 \sin(\beta\ell)}{Z_0 \cos(\beta\ell) + jZ_{LOAD} \sin(\beta\ell)} = Z_0 \frac{Z_{LOAD} + jZ_0 \tan(\beta\ell)}{Z_0 + jZ_{LOAD} \tan(\beta\ell)} \quad (8.17)$$

Additionally, the input impedance of the transmission line can be calculated using the voltage reflection coefficient transformed to the input of the line ($\ell=L$):

$$Z_{IN}(L) = Z_{LINE} \frac{1 + \Gamma(L)}{1 - \Gamma(L)} \quad (8.18)$$

Input impedance of the shorted line

When the lossless line is terminated by a short circuit ($Z_{LOAD}=0$) with its reflection coefficient

$$\Gamma_L = \Gamma_{SHORT} = \frac{Z_{LOAD} - Z_{PORT}}{Z_{LOAD} + Z_{PORT}} = -1 \quad (8.19)$$

the reflection coefficient seen at beginning of the line will become:

$$\Gamma(L) = \Gamma_{SHORT} e^{-j2\beta\ell} = -e^{-j2\beta L} \quad (8.20)$$

¹⁰ In order to have coherent marking with the literature, the end of the transmission line, where the load is connected has been assigned position $\ell=0$. Since the transmission line is placed at the left side of the load, its length L will be a negative number.

and the impedance transformation formula (8.17) will reduce to:

$$Z_{IN} = jZ_0 \tan(\beta L) \quad (8.21)$$

8.7.2 Analysis of the shorted line connected to an unmatched port

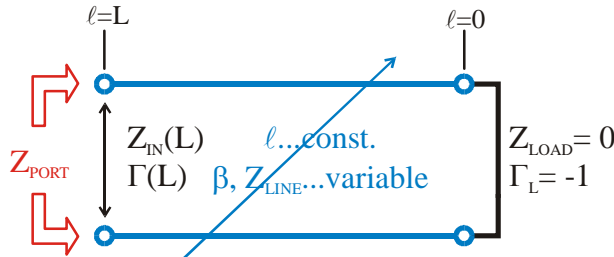


Fig. 8.15: Simple shorted transmission line connected to an unmatched port

The first type of structure, which may have useful properties for phase-shifter devices, is a shorted variable impedance line connected to an unmatched input port, shown in the Fig. 8.15. The shorted line connected to the impedance mismatched input port forms a transmission line resonator. It is obvious, that changes of the electrical parameters of line (nominal impedance or/and phase constant, length), or the port impedance will have an impact to the S_{11} parameter of this structure. If lossless, or low loss line will be used, the magnitude of S_{11} will remain unity (or close to unity), but the argument will change. By mathematical analysis, the sensitivity of the phase change as a function of various structure parameters may be examined. Then, by choosing specific line and port parameters, the resulting structure can be optimised to obtain the maximal available phase-shift caused by changes of the controlling quantity.

In order to obtain a final phase-shift, we have to calculate the reflection coefficient seen by the device's input port.

Using the voltage reflection coefficient transformation along the transmission line, we can calculate the impedance seen at the beginning of the shorted line (inject (8.20) into (8.18)):

$$Z_{IN}(L) = Z_{LINE} \frac{1 - e^{-j2\beta L}}{1 + e^{-j2\beta L}} \quad (8.22)$$

Then (8.14) gives a value of the input reflection coefficient:

$$S_{11} = \Gamma_{PORT} = \frac{Z_{IN}(L) - Z_{PORT}}{Z_{IN}(L) + Z_{PORT}} \quad (8.23)$$

(8.22) introduces the length of the actual structure:

$$S_{11} = \frac{Z_{\text{LINE}} \frac{1 - e^{-j2\beta L}}{1 + e^{-j2\beta L}} - Z_{\text{PORT}}}{Z_{\text{LINE}} \frac{1 - e^{-j2\beta L}}{1 + e^{-j2\beta L}} + Z_{\text{PORT}}} \quad (8.24)$$

and a simplified and rearranged version of (8.24) gives:

$$S_{11} = \frac{(-1 + e^{j2\beta L}) Z_{\text{LINE}} - (1 + e^{j2\beta L}) Z_{\text{PORT}}}{(-1 + e^{j2\beta L}) Z_{\text{LINE}} + (1 + e^{j2\beta L}) Z_{\text{PORT}}} \quad (8.25)$$

However, (8.25) still does not contain the externally controlled parameter – the variable inductance of the transmission line. The distributed inductance and the distributed capacitance obtained by the finite element method calculation will be applied using (8.3) and (8.4). From this, we obtain:

$$S_{11} = \frac{\left(-1 + e^{j2L\omega \sqrt{L_0 C_0}}\right) \sqrt{\frac{L_0}{C_0}} - \left(1 + e^{j2L\omega \sqrt{L_0 C_0}}\right) Z_{\text{PORT}}}{\left(-1 + e^{j2L\omega \sqrt{L_0 C_0}}\right) \sqrt{\frac{L_0}{C_0}} + \left(1 + e^{j2L\omega \sqrt{L_0 C_0}}\right) Z_{\text{PORT}}} \quad (8.26)$$

L_0 in (8.26) is the distributed inductance of the ferrite loaded strip-line, C_0 its distributed capacity, L its length, ω is the operating frequency and Z_{PORT} is the impedance of the input port.

Since the structure has multiple independent parameters, in order to examine the influence of each parameter, some of them must be held constant and preferably close to the expected operating values. The following list gives an overview of reasonable values of the parameters for the RF structure:

- Impedance of the ferrite loaded line: 1.2 to 12 Ohm (see the Table 8.2)
- “Port” impedance: 10 to 50 Ohm (see paragraph 8.4)
- Length of the structure: 50 to 100 mm (e.g. thermal loading considerations)
- Operating frequency: is given to be 352, 704 and 1408 MHz respectively (three different systems)

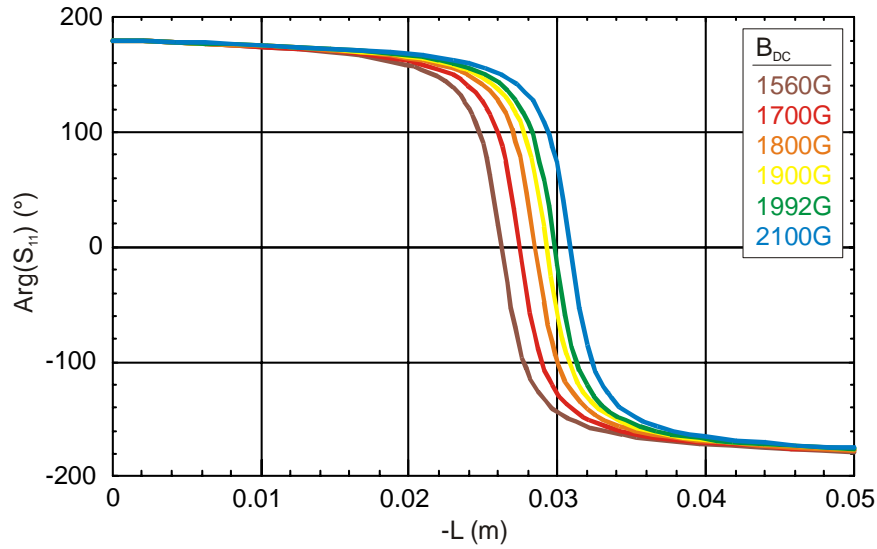


Fig. 8.16: A typical curve for argument of the S_{11} at different ferrite magnetizations ($f=352\text{MHz}$, $w=150\text{mm}$, $f=1.5\text{mm}$, $Z_{PORT}=200\Omega$)

The characteristic curve for $\text{Arg}(S_{11})$ for a variable ferrite bias magnetization is shown in the Fig. 8.16.

However, when developing the phase-shifter device, it is important to consider not only the absolute value of the $\text{Arg}(S_{11})$, but the stroke of the phase caused by the change of the ferrite layer bias point. This value will be called the differential phase-shift (DP, or $\Delta\phi$) and can be obtained using the formula:

$$\text{DP} = \Delta\phi = \text{Arg}(S_{11}[B_{\max}]) - \text{Arg}(S_{11}[B_{\min}]) \quad (8.27)$$

Fig. 8.17 shows a typical curve of differential phase-shift as a function of the line length.

In the next paragraphs the sensitivity of the differential phase-shift to the different structure parameters will be examined further.

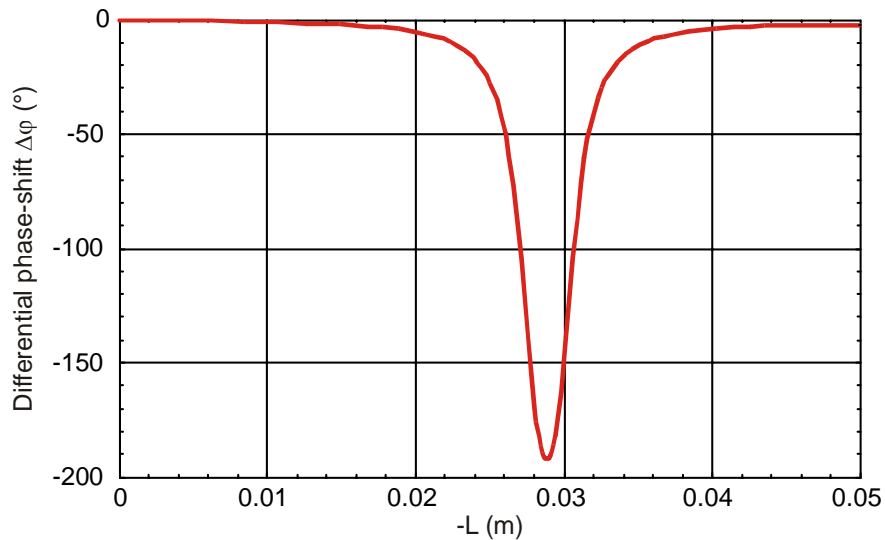


Fig. 8.17: Typical curve for the $\Delta\phi$ as a function of line length

8.7.3 Influence of the transmission line impedance and length on the $\Delta\phi$

An analysis of achievable strip-line impedances was done in chapter 8.6. It was shown that the highest impedance change and propagation speed change is achievable for transmission lines where the inductance is dominant i.e. very low impedance lines. Due to the RF power handling and phase tuning power¹¹ requirements, cooling capabilities etc. it is reasonable to build a variable impedance part with impedances in range about 1.2 to 3 Ohm. The Fig. 8.18 shows a comparison of differential phase-shift for the different impedances of the variable line at 352MHz and Fig. 8.19 at 704MHz.

The length of the structure is related to a center frequency, where the maximum of the phase-shift is available. Nevertheless, short structures suffer from bad cooling and long structures introduce higher RF power losses and significant increase in the phase tuning power needs. Practically usable values will be below 100mm.

¹¹ phase tuning power = power needed to tune the RF phase ($\Delta\phi$) at a certain tuning frequency e.g. full scale $\Delta\phi$ change with 500Hz repetition frequency

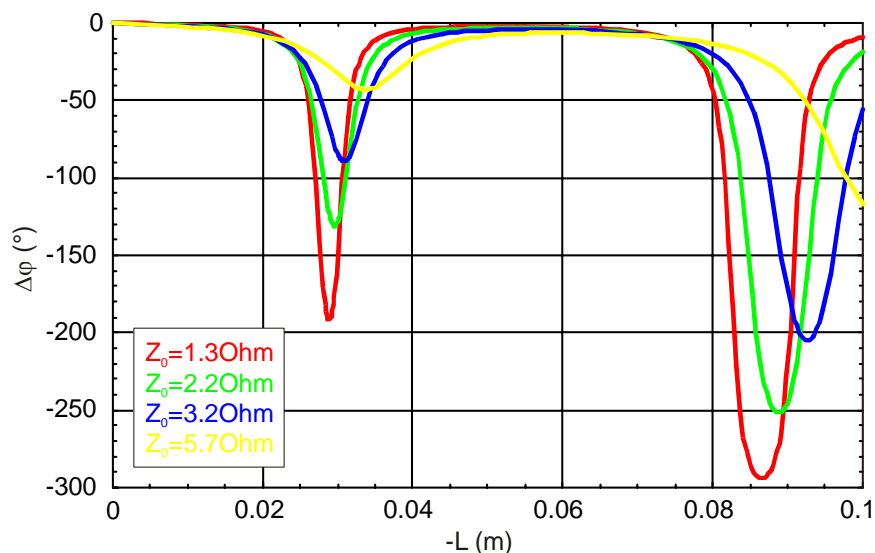


Fig. 8.18: $\Delta\varphi$ for the different impedances of the variable line at 352MHz

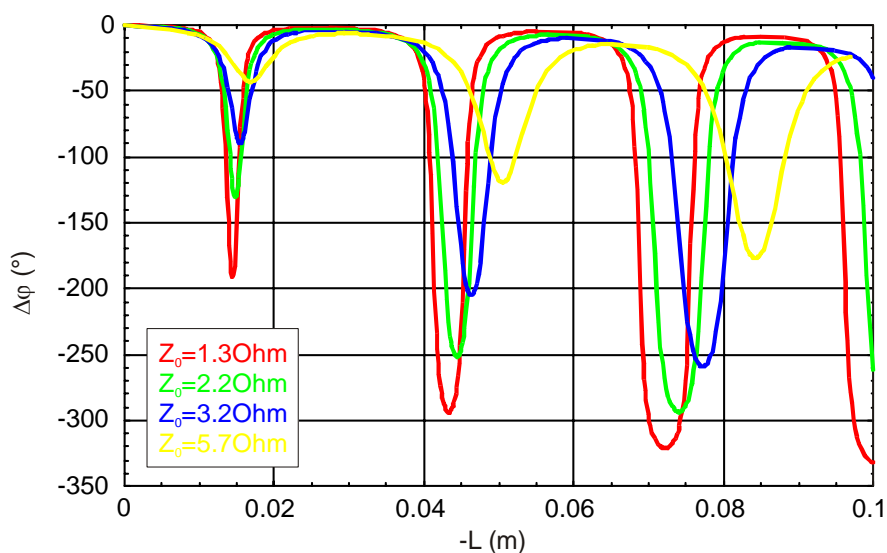


Fig. 8.19: $\Delta\varphi$ for the different impedances of the variable line at 704MHz

The use of the discussed type of structure (simple variable impedance line connected to the unmatched port) at 1408MHz does not bring any substantial advantages and it starts to suffer from higher order modes inside the structure.

8.7.4. Influence of the port impedance on the $\Delta\varphi$

Due to the impedance mismatch between the variable impedance line and the port, a resonator is formed. From circuit theory it is known, that a higher load impedance is damping the resonator less, providing a higher circuit Q [66].

In practice, reasonable values of the feeder line impedance (the “port”) will lie in range of 10 to 50 Ohms. Fig. 8.20 shows the highest available $\Delta\phi$ as a function of the port impedance. Fig. 8.21 shows an interesting property of such a structure. When the length of the ferrite loaded line is properly chosen, the $\Delta\phi$ will not be dependent on the port impedance (or only very little).

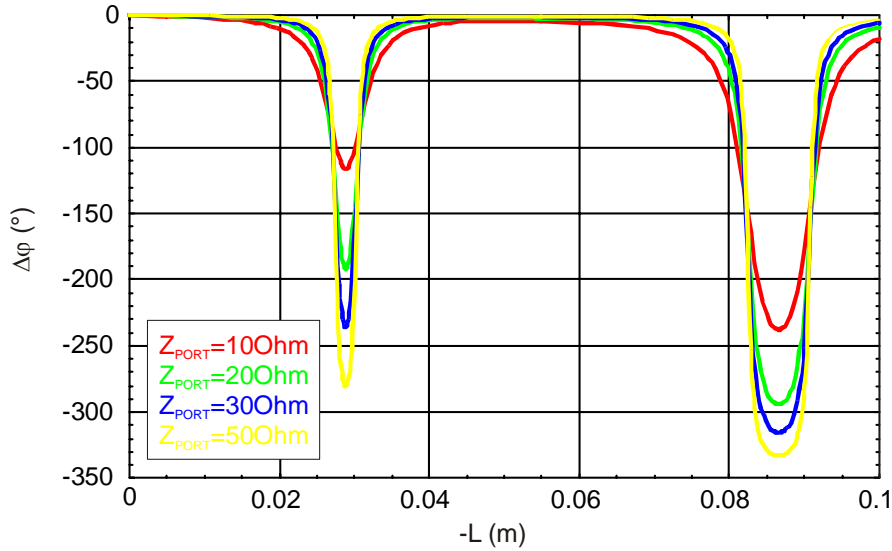


Fig. 8.20: $\Delta\phi$ as a function of the port impedance, $f=352\text{MHz}$

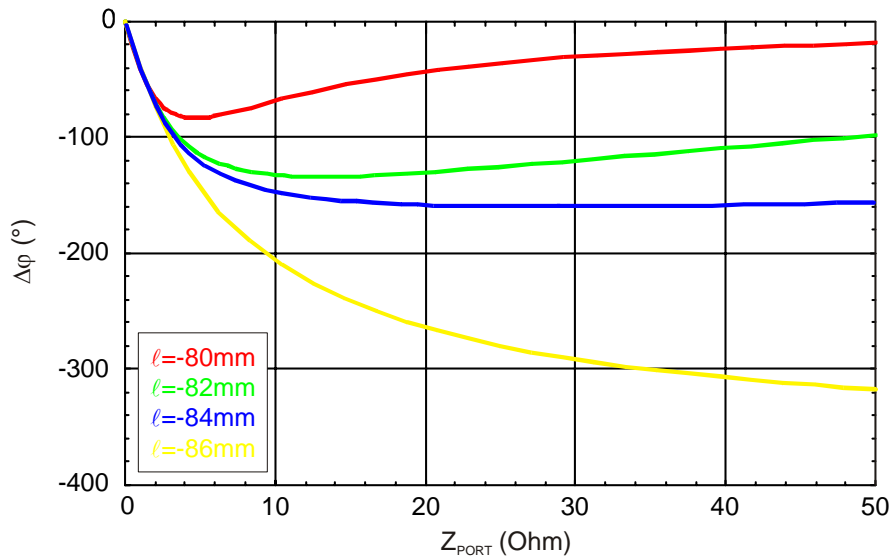


Fig. 8.21: $\Delta\phi$ as a function of the port impedance for certain line length, $f=352\text{MHz}$

8.7.5 Influence of the frequency to the $\Delta\phi$

The operating frequency is the only imposed parameter. In the present SPL accelerator study a 352MHz system is used, but in the future, 704 and 1408MHz systems are foreseen.

However, as was mentioned earlier, the use of the discussed type of structure at 1408MHz is not optimal. $\Delta\phi$ as a function of the frequency is shown in Fig. 8.22.

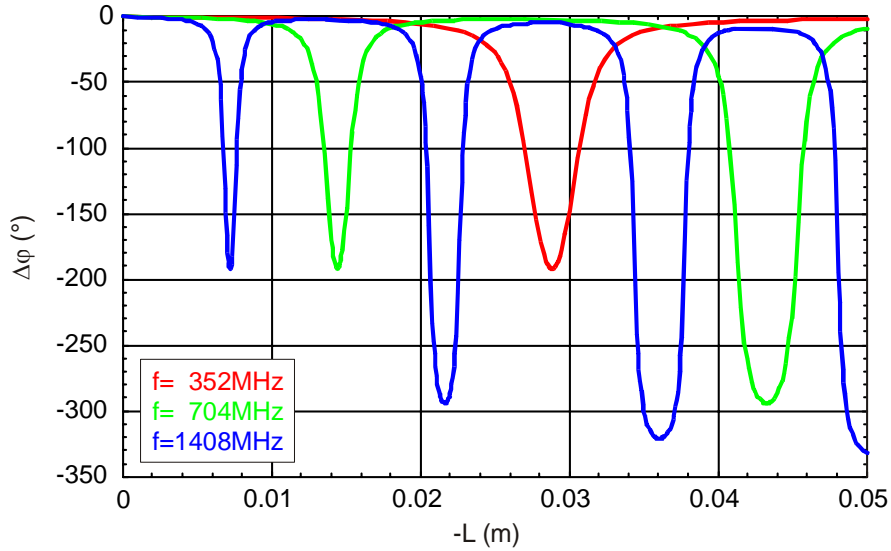


Fig. 8.22: $\Delta\phi$ as a function of the frequency

8.7.6 Voltage distribution along the phase-shifting structure

Since the phase-shifters discussed in this thesis are foreseen to operate in the high-power RF system, adequate dimensions of all structures must be chosen to ensure proper operation. The electric field stress on the structure is analyzed in the next paragraphs.

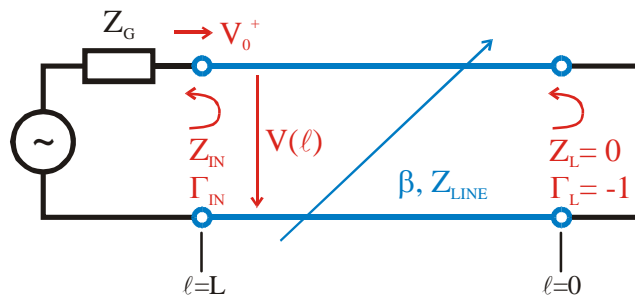


Fig. 8.23: Phase-shifting structure excited by the generator

Because both generator and load may be mismatched, multiple reflections occur on the transition to the transmission line. The circuit can be analyzed using an infinite series to represent multiple reflections, or the impedance transformation method. The second method is easier and more useful for practical applications.

The voltage along the transmission line in the presence of reflections can be written as:

$$V(z) = V_0^+ \left(e^{-j\beta\ell} + \Gamma_L e^{+j\beta\ell} \right) \quad (8.28)$$

where V_0^+ is the “driving” voltage. The latter is in fact the voltage passed to the structure from the mismatched port (the complement of the generator voltage being reflected back to the generator). Therefore the voltage at the entry of the line is

$$V(\ell = L) = V_g \frac{Z_{in}}{Z_{in} + Z_g} \quad (8.29)$$

Z_{in} stands for impedance seen at the beginning of the line, where the generator is connected. By using (8.28) and (8.29) we can find the value of V_0^+ from the equity at the beginning of the line ($\ell=L$):

$$V_g \frac{Z_{in}}{Z_{in} + Z_g} = V_0^+ (e^{-j\beta L} + \Gamma_L e^{+j\beta L}) \quad (8.30)$$

yielding:

$$V_0^+ = V_g \frac{Z_{in}}{Z_{in} + Z_g} \frac{1}{e^{-j\beta L} + \Gamma_L e^{+j\beta L}} \quad (8.31)$$

Injecting it into a (0.28) we obtain:

$$V(\ell) = V_g \frac{Z_{in}}{Z_{in} + Z_g} \frac{e^{-j\beta \ell} + \Gamma_L e^{+j\beta \ell}}{e^{-j\beta L} + \Gamma_L e^{+j\beta L}} \quad (8.32)$$

In the case of the phase-shifter structure, the transmission line is shorted at its end, giving a $\Gamma_L = -1$. Then impedance Z_{in} can be replaced by (8.21) and final formula for the voltage along the transmission line will simplify into:

$$V(\ell) = V_g \frac{Z_{LINE} \tan \beta L}{Z_{LINE} \tan \beta L - jZ_g} \frac{e^{-j\beta \ell} - e^{+j\beta \ell}}{e^{-j\beta L} - e^{+j\beta L}} \quad (8.33)$$

As it is more convenient to use the distributed transmission line parameters L_0 and C_0 for the variable impedance line, (8.33) will become:

$$V(\ell) = V_g \frac{\sqrt{\frac{L_0}{C_0}} \tan(\omega L \sqrt{L_0 C_0})}{\sqrt{\frac{L_0}{C_0}} \tan(\omega L \sqrt{L_0 C_0}) - jZ_g} \frac{e^{-j\omega \ell \sqrt{L_0 C_0}} - e^{+j\omega \ell \sqrt{L_0 C_0}}}{e^{-j\omega L \sqrt{L_0 C_0}} - e^{+j\omega L \sqrt{L_0 C_0}}} \quad (8.34)$$

The design of a phase-shifter is an iterative process, where multiple parameters have to be chosen as a compromise between the RF performance, phase tuning power requirements, thermal considerations etc. Once the expected variable impedance line is defined, the voltage stress analysis can be performed, and eventually all parameters iteratively corrected.

Fig. 8.24 shows the typical voltage distribution along the phase-shifting structure, normalized to the generator voltage.

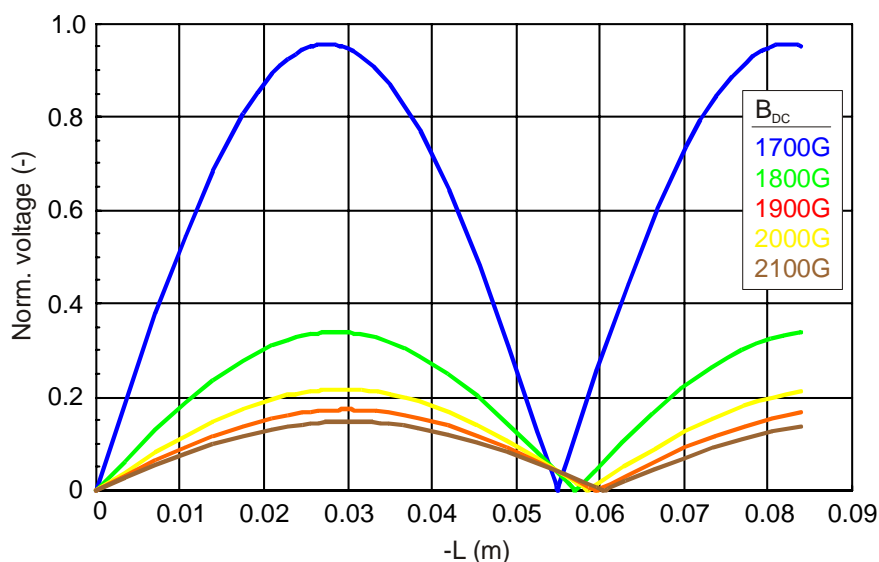


Fig. 8.24: The typical normalised voltage distribution along the phase-shifting structure ($f=352\text{MHz}$, $L=-82\text{mm}$, ferrite loaded line with parameters from Table 8.4, $Z_{\text{PORT}}=20\text{Ohm}$)

In some applications, phase-shifting devices may operate in so called “full reflection mode”. This means, the phase-shifter is loaded by the forward wave, propagating from the generator towards the load, and the wave reflected from the load, propagating towards the generator. These two waves combine inside the phase-shifter providing in the worst case a double voltage loading of the strip-line structure.

8.8 Reflection coefficient of the two serially connected transmission lines with an unmatched port – coaxial phase-shifter type two

The behavior of the ferrite loaded strip-line, shorted at one end and connected to the impedance mismatched port was analyzed in the previous chapter. However, this kind of structure is not always the most appropriate solution. As already mentioned, the length of the ferrite loaded line is a very broad compromise between the RF parameters, phase tuning speed and the power required to perform this tuning. A single variable impedance line configuration may not provide the best compromise e.g. the structure must be either too short (problems

with cooling) or too long (problems with tuning speed) for obtaining a certain desired phase-shift (see Fig. 8.22).

Inserting an additional transmission line with different electrical parameters may help to overcome this disadvantage as well as providing other useful characteristics. With this additional degree of freedom, a better compromise between the structure parameters of the phase-shifter may be achieved.

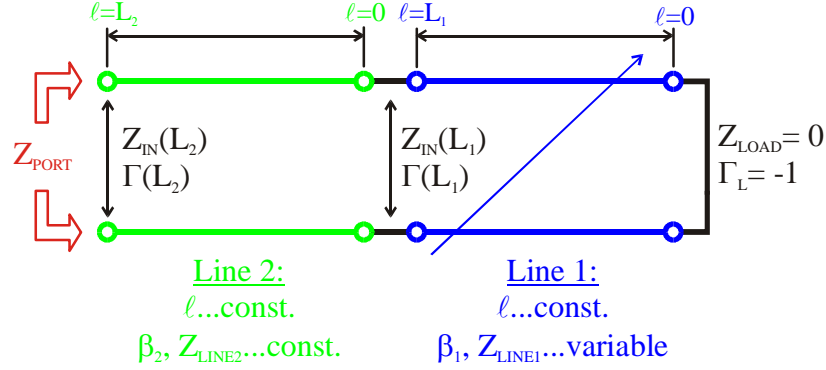


Fig. 8.25: Two serially connected transmission lines and the unmatched port

A mathematical analysis of this case will use the impedance transformation along the transmission line (8.17). The short circuit, transformed to the start of the line 1 has the impedance:

$$Z_{IN}(L_1) = jZ_{LINE1} \tan(\beta_1 L_1) \quad (8.35)$$

The impedance $Z_{IN}(L_1)$ is further transformed along line 2:

$$Z_{IN}(L_2) = Z_{LINE2} \frac{Z_{IN}(L_1) + jZ_{LINE2} \tan(\beta_2 L_2)}{Z_{LINE2} + jZ_{IN}(L_1) \tan(\beta_2 L_2)} \quad (8.36)$$

obtaining:

$$Z_{IN}(L_2) = j \frac{Z_{LINE2} [Z_{LINE1} \tan(\beta_1 L_1) + Z_{LINE2} \tan(\beta_2 L_2)]}{Z_{LINE2} - Z_{LINE1} \tan(\beta_1 L_1) Z_{LINE2} \tan(\beta_2 L_2)} \quad (8.37)$$

Injecting (8.14) results in the input reflection coefficient

$$S_{11} = \Gamma_{PORT} = \frac{Z_{IN}(L_2) - Z_{PORT}}{Z_{IN}(L_2) + Z_{PORT}} = \quad (8.38)$$

$$= \frac{Z_{LINE2} [jZ_{PORT} + Z_{LINE2} \tan(\beta_2 L_2)] + Z_{LINE1} \tan(\beta_1 L_1) [Z_{LINE2} - jZ_{PORT} \tan(\beta_2 L_2)]}{Z_{LINE2} [-jZ_{PORT} + Z_{LINE2} \tan(\beta_2 L_2)] + Z_{LINE1} \tan(\beta_1 L_1) [Z_{LINE2} + jZ_{PORT} \tan(\beta_2 L_2)]} \quad (8.39)$$

As in the chapter 8.7.2, the transmission line parameters of line one are defined by the distributed inductance L_0 and capacitance C_0 , obtaining:

$$S_{11} = \frac{Z_{\text{LINE2}}[jZ_{\text{PORT}} + Z_{\text{LINE2}} \tan(\beta_2 L_2)] + \dots}{Z_{\text{LINE2}}[-jZ_{\text{PORT}} + Z_{\text{LINE2}} \tan(\beta_2 L_2)] + \dots} \dots \quad (8.40)$$

$$\dots \frac{+ \sqrt{\frac{L_0}{C_0}} \tan(\omega \sqrt{L_0 C_0} L_1) [Z_{\text{LINE2}} - jZ_{\text{PORT}} \tan(\beta_2 L_2)]}{+ \sqrt{\frac{L_0}{C_0}} \tan(\omega \sqrt{L_0 C_0} L_1) [Z_{\text{LINE2}} + jZ_{\text{PORT}} \tan(\beta_2 L_2)]}$$

where L_1 and L_2 are the line lengths, β_2 is the phase constant of the fixed impedance line and Z_{LINE2} is its impedance.

The structure has, as in the previous case, many independent parameters. The idea is to fix parameters of the variable impedance line to reasonable values giving a good performance (e.g. high phase-shift stroke, optimal magnetic circuit length, low losses etc.), and “tune” the rest of the parameters (e.g. center frequency) by the additional transmission line.

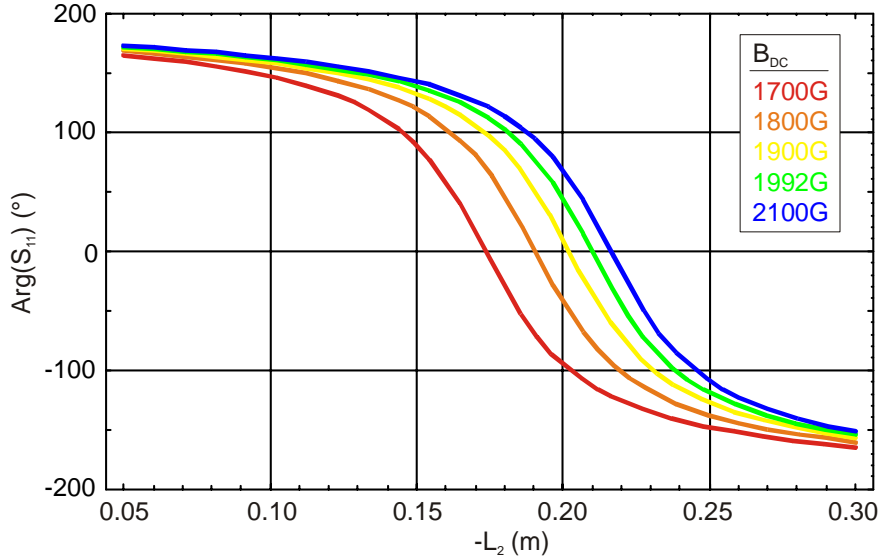


Fig. 8.26: A typical curve for argument of the S_{11} at different ferrite magnetizations ($f=352\text{MHz}$, $Z_{1700}=1.43\text{Ohm}$, $Z_{\text{PORT}}=30\text{Ohm}$)

Fig. 8.26 shows a typical curve of the $\text{Arg}(S_{11})$ at different ferrite magnetizations, Fig. 8.27 shows the differential phase-shift for the same case. When comparing with the “single line and port” structure (Fig. 8.16 and Fig. 8.17), we can see that the curves are less steep, and the peak on the differential phase-shift characteristics is wider. This relaxes requirements on

the precision of the line lengths and electrical parameters, and gives a certain freedom to optimize the structure parameters.

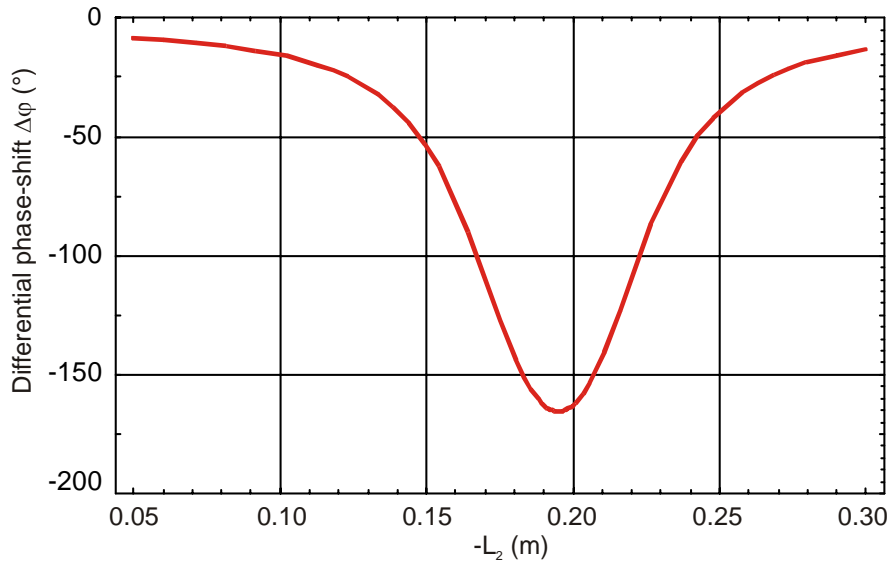


Fig. 8.27: Differential phase-shift as a function of the length L_2

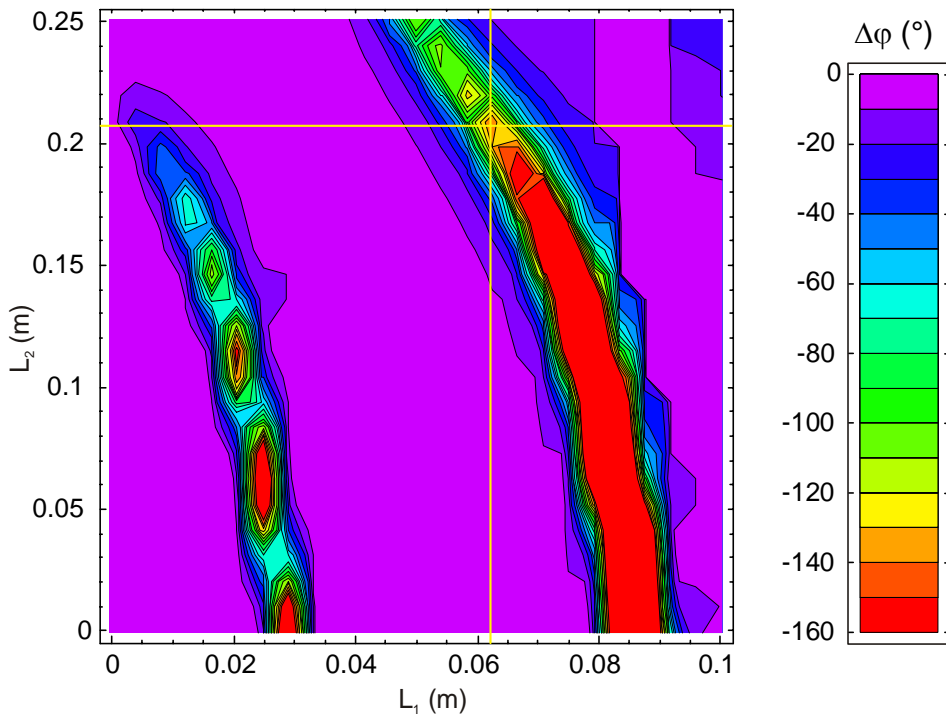


Fig. 8.28: $\Delta\phi$ as a function of the line lengths ($f=352\text{MHz}$, $Z_{\text{PORT}}=20\text{Ohm}$, $Z_{\text{LINE1}}=1.43\text{Ohm}@1700\text{Gauss}$, $Z_{\text{LINE2}}=3\text{Ohm}$)

Fig. 8.28 shows the differential phase-shift as a function of the two transmission-line lengths. Once the optimal length of the ferrite-loaded structure is calculated, the “working point”

regarding the required $\Delta\phi$ may be adjusted by the length of the fixed line as a second structure parameter. An example from Fig. 8.28 (the yellow lines) shows such an exercise.

8.9 Ferrite loaded transmission line in the transmission mode – coaxial phase-shifter type three

The transmission type phase-shifter is a two port device, shifting the phase of the passing signal while maintaining very low input and output reflection coefficients. The transmission type of the coaxial phase-shifter is represented for example by the coaxial line fully or partially filled by the ferrite material. Depending on the bias working point, the fully filled structures could even be used as coaxial switches.

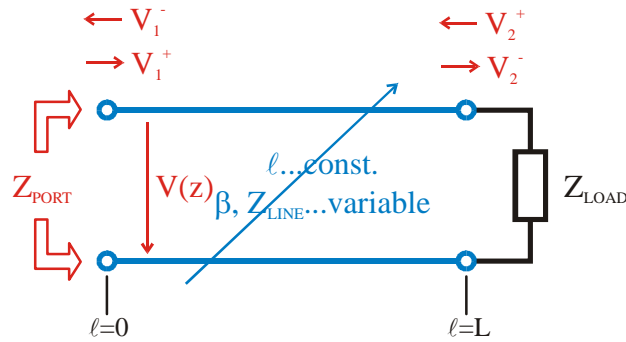


Fig. 8.29: Transmission type of phase-shifter

The wave passing through the phase-shifter is delayed by the factor S_{21} as:

$$V_2^- = S_{21} V_1^+ = V_1^+ e^{-j\beta L} \quad (8.41)$$

where β is the phase constant of the considered line and L its length. If the ferrite loaded line is used, the change of the ferrite permeability is changes the total delay and hence the phase-shift of such a line.

Similar to the single port devices the differential phase shift is then defined as:

$$DP = \Delta\phi = \text{Arg}(S_{21}[B_{\max}]) - \text{Arg}(S_{21}[B_{\min}]) \quad (8.42)$$

Since

$$\text{Arg}(S_{21}) = -\beta L \quad (8.43)$$

for $\Delta\phi$ we can write:

$$\Delta\phi = L\beta_{B_{\max}} - L\beta_{B_{\min}} = L\omega(\sqrt{L_0[B_{\min}]C_0} - \sqrt{L_0[B_{\max}]C_0}) \quad (8.44)$$

An example of $\Delta\varphi$ as a function of the structure length and the frequency of the transmission lines from Table 8.2 is shown in Fig. 8.30.

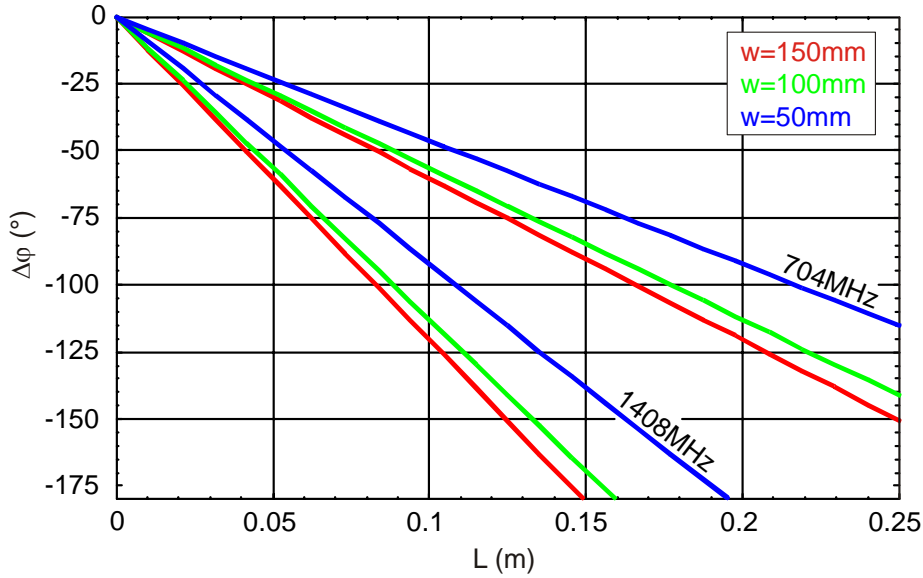


Fig. 8.30: $\Delta\varphi$ as a function of the structure length and the frequency (considered transmission lines from Table 8.2)

8.9.1 Impedance mismatch of the transmission type phase-shifter

Since the transmission line parameters (Z_{LINE} , β) change while the phase-shift is tuned, the variable line will not be matched for all working points. The voltage reflection coefficient can be calculated and analyzed in order to minimize the impedance mismatch over the whole phase tuning range.

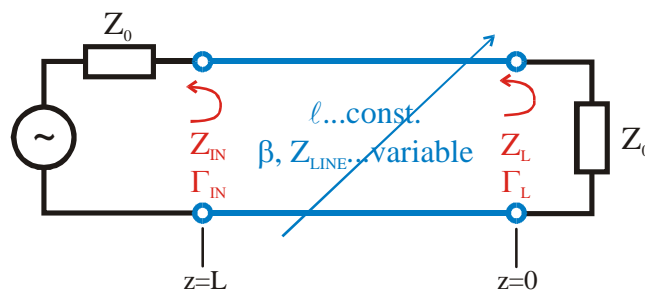


Fig. 8.31: Impedance mismatch caused by the phase tuning

The load impedance, Z_0 , transformed by the variable impedance line will have a value at the beginning of the line of:

$$Z_{\text{IN}} = Z_{\text{LINE}} \frac{Z_0 + jZ_{\text{LINE}} \tan(\beta L)}{Z_{\text{LINE}} + jZ_0 \tan(\beta L)} \quad (8.45)$$

and the voltage reflection coefficient at the beginning of the line will be:

$$\Gamma_{IN} = S_{11} = \frac{Z_{IN} - Z_0}{Z_{IN} + Z_0} = \frac{(Z_{LINE}^2 - Z_0^2) \tan(\beta L)}{(Z_{LINE}^2 + Z_0^2) \tan(\beta L) - j2Z_0 Z_{LINE}} \quad (8.46)$$

The mismatch (proportional to $\text{Mag}(S_{11})$) can be minimized by choosing a suitable electrical length and impedance of the variable impedance line. For the real system, it is reasonable to chose $Z_0 = Z_{LINE}$ [middle range]. Then assuming small variations in the line inductance by factor x (x is very close to unity):

$$L'_0 \rightarrow x L_0 \quad (8.47)$$

the impedance of the line can be replaced by:

$$Z_0 = \sqrt{L_0 / C_0} \rightarrow \sqrt{x L_0 / C_0} = \sqrt{x} Z_0 \quad (8.48)$$

and the electrical length of the line βL can be replaced by:

$$\beta L = \omega L \sqrt{L_0 C_0} \rightarrow \omega L \sqrt{x L_0 C_0} = \beta L \sqrt{x} \quad (8.49)$$

(8.48) can be then simplified obtaining:

$$S_{11} = \frac{(x - 1) \sin(\beta L \sqrt{x})}{(x + 1) \sin(\beta L \sqrt{x}) - j2\sqrt{x} \cos(\beta L \sqrt{x})} \quad (8.50)$$

Typical values of $\text{Mag}(S_{11})$ for the phase-shifter as a function of phase tuning and its electrical length are shown in Fig. 8.32.

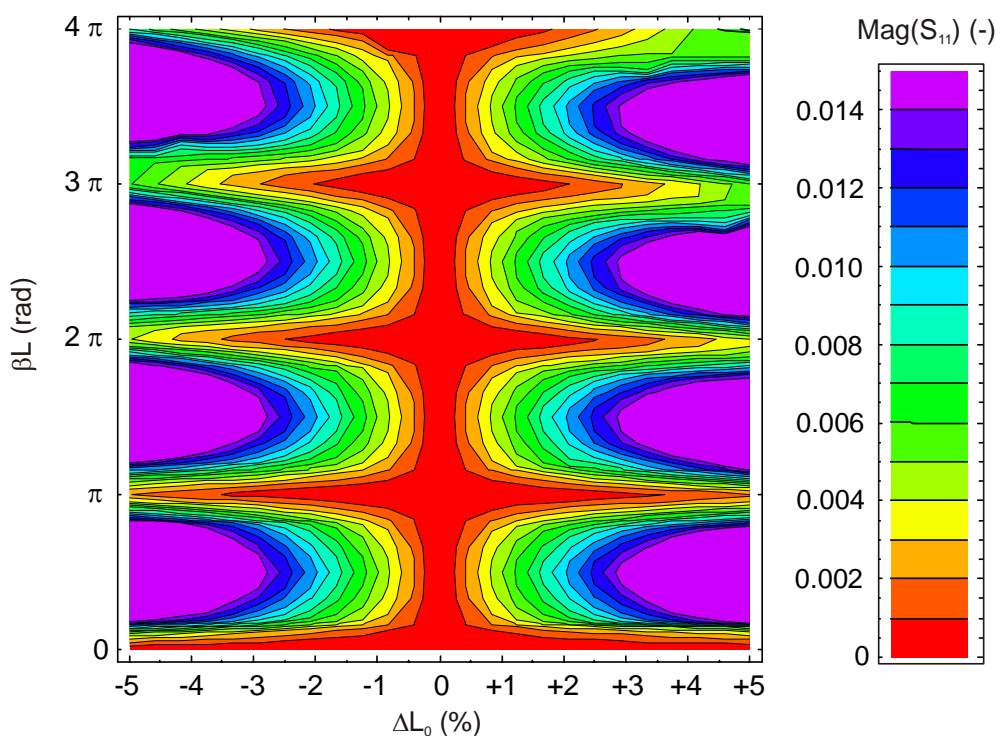


Fig. 8.32: Typical values of $\text{Mag}(S_{11})$ for the phase-shifter as a function of phase tuning and its electrical length.

8.10 Thermal load of the phase-shifting structure

The phase-shifters discussed in this work are foreseen to operate at power levels in the range of several hundred of kilowatts peak, and about one hundred kilowatts r.m.s. power. Hence not only the electromagnetic stress, but the temperature stress has to be analyzed.

Fig. 8.33 shows the cross-section of the RF strip-line structure. The heat is generated inside the ferrite region and transferred to the cooling water via the stainless steel wall. A small fraction of the heat is transported away by the outer conductor to the ambient air.

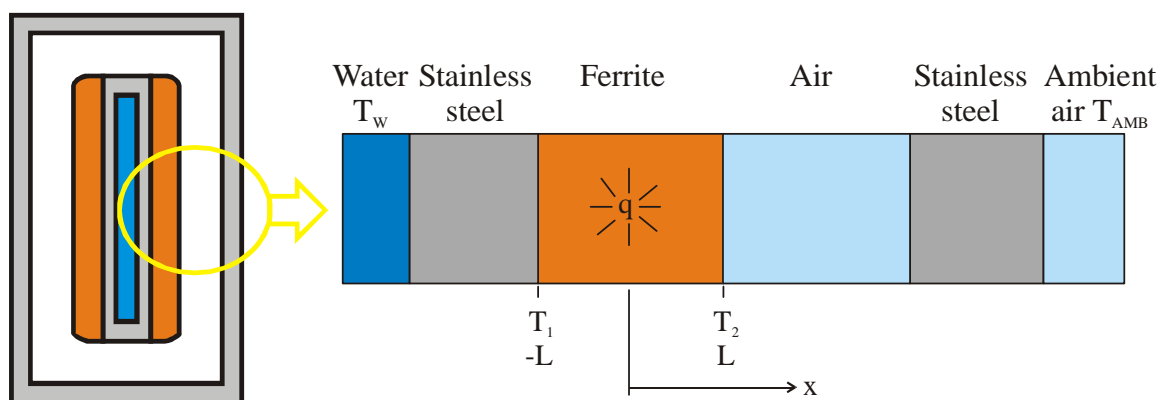


Fig. 8.33: Cross-section of the strip-line structure for the thermal calculations

Since the RF pulses are short compared to the thermal relaxation times of the structure, it represents a steady state conduction problem with a uniform heat source in one of the sub-layers [74].

Generally, the steady state temperature distribution inside the ferrite, as a heat source, is described by the differential equation:

$$\frac{\partial^2 T}{\partial x^2} + \frac{\dot{q}}{k_f} = 0 \quad (8.51)$$

where \dot{q} is a source term in the equation governing the energy balance (W/m^3) and k_f is the thermal conductivity of the ferrite material (W/mK). The solution of this equation for a uniform source term is:

$$T(x) = -\frac{\dot{q}L^2}{2k_f} \left(1 - \frac{x^2}{L^2} \right) + \frac{T_2 - T_1}{2} \frac{x}{L} + \frac{T_2 + T_1}{2} \quad (8.52)$$

where T_1 and T_2 are the “boundary” temperatures at both sides of the ferrite layer. Since the thermal conductivity of the air is much smaller than the one of the stainless steel, a non-uniform thermal distribution across the ferrite will build up.

Fig. 8.34 shows an example of the temperature distribution across the strip-line structure (infinite ideal 2D model) as a function of the ferrite layer thickness. For numerical calculations, the StarCD code was used [75]. The material parameters were set to describe a common microwave ferrite material and thermal dissipation was set to $\dot{q}=18\text{mW/mm}^3$. Formula (8.52) shows, that the peak temperature is a linear function of the thermal power loss and quadratic function of the layer thickness, where the losses are dissipated. These are the important facts, which must be considered when determining the ferrite layer thickness.

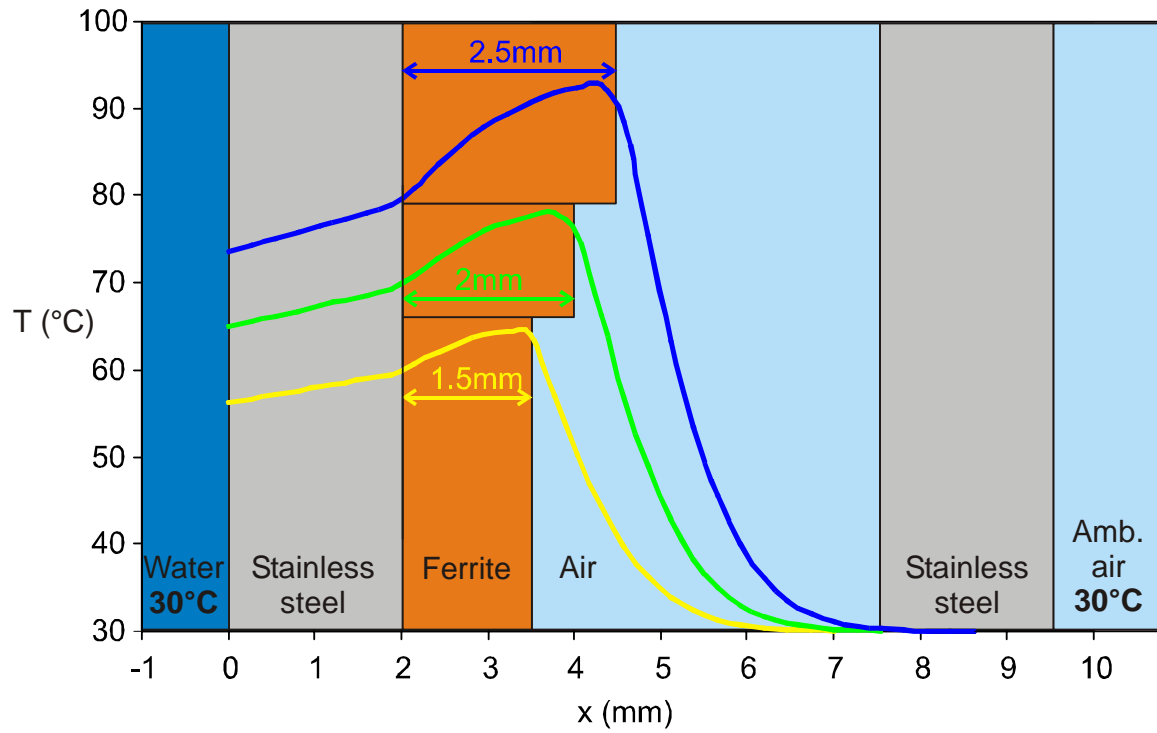


Fig. 8.34: Temperature distribution across the strip-line structure for same volume heat dissipation and three different ferrite thicknesses

9

Phase tuning speed, the CERN high power, fast ferrite phase-shifter

Main subject of chapter 9 is the phase tuning speed and optimization of the structure in order to obtain the best tuning performance. A development of a particular phase-shifter for the CERN's SPL application is discussed and achieved data are shown.

9.1 Phase tuning speed

In previous chapters, different phase and amplitude modulators were shown and different types of phase-shifters were analysed. What is common for all phase-shifters is the way, in which the phase is tuned. The variable permeability ferrite region must be properly DC biased in order to achieve the correct working point and hence low RF losses. The ferrite region must be also properly penetrated by the tuning magnetic field in order to achieve a good tuning performance. As the RF structure has to be entirely surrounded by the “RF tight” housing using a highly conductive material (low RF losses), the penetration efficiency of the variable tuning field significantly influences the phase tuning speed and hence must be analyzed.

If a conductive material is placed into a variable magnetic field, eddy currents, trying to compensate the source field, will appear. The phase-shifter eddy currents are directly limiting the phase-tuning speed. For the application with former LEP2 superconducting cavities, a sufficient phase tuning speed up to 1kHz is necessary (see paragraph 4.6). As the 704 and 1408MHz cavities are mechanically smaller, the disturbing mechanical modes will have even higher frequencies.

Materials used in the phase-shifter and their electromagnetic properties are listed in Table 9.1. All materials, where the skin depth is comparable with its thickness must be examined for eddy currents influence. Numerous computer simulations using the Maxwell 2D and Maxwell 3D codes [54] were run in order to optimize the phase-shifter structure for highest possible tuning speed. The Fig. 9.1 shows a 3D model of the phase-shifter, used also for simulations.

	Stainless steel	Magnetic steel	Copper	Silver	Ferrite	NdFeB magnet
Relative permeability (-)	1	2000	1	1	10	1
Relative permittivity (-)	1	1	1	1	14	1
Conductivity (S/m)	1.1×10^6	-	5.8×10^7	6.1×10^7	1×10^{-2}	6.25×10^5
Thermal conductivity (W/mK)	15	45	400	427	3.5	-
Magnetic retentivity B_r (T)	-	-	-	-	-	0 to 1.2
Skin depth at 50Hz (mm)	67.9	-	9.3	9.1	-	90.0
Skin depth at 500Hz (mm)	21.5	-	3.0	2.9	-	28.5
Skin depth at 2kHz (mm)	10.7	-	1.5	1.4	-	14.2
Skin depth at 352MHz (μm)	25.6	-	3.5	3.4	-	n/a

Table 9.1: Electromagnetic properties of the phase-shifter's materials

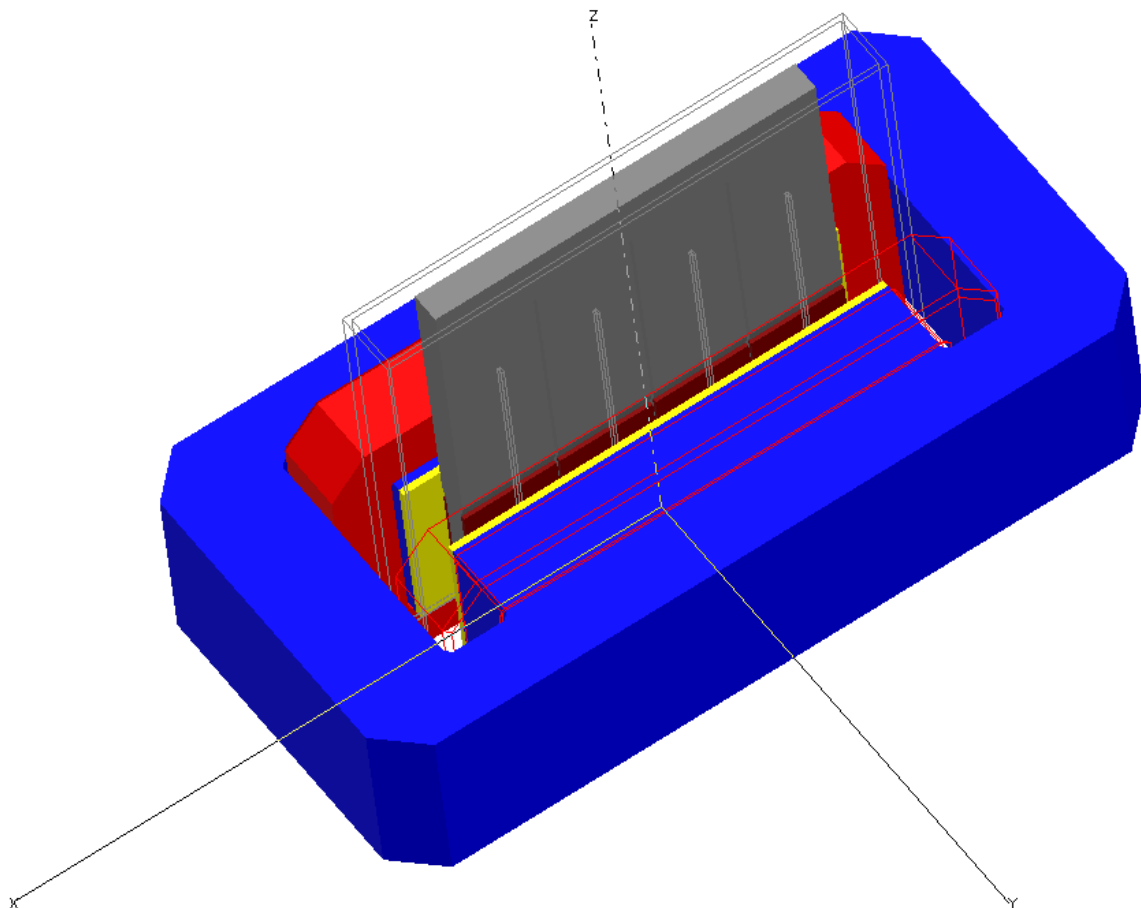


Fig. 9.1: 3D model of the CERN fast ferrite phase-shifter. Legend: blue – magnetic circuit, red – coils, yellow – permanent magnets, brown – ferrites, grey – strip-line metallic structure.

In order to minimize the eddy currents, the inner and outer conductor of the strip-line structure is slotted. The number of slots, and their position was optimized by computer simulations for the best compromise between the electrical performance and the manufacturing effort. As the tuning frequency is rising, less and less of the magnetic field is penetrating into the ferrite region and the distribution of the magnetic field is not uniform. The nominal tuning field stroke was chosen to be ± 200 Gauss. Its field distribution as a function of tuning frequency in 5mm slices is shown in Fig. 9.2, Fig. 9.3, Fig. 9.4, and Fig. 9.5.

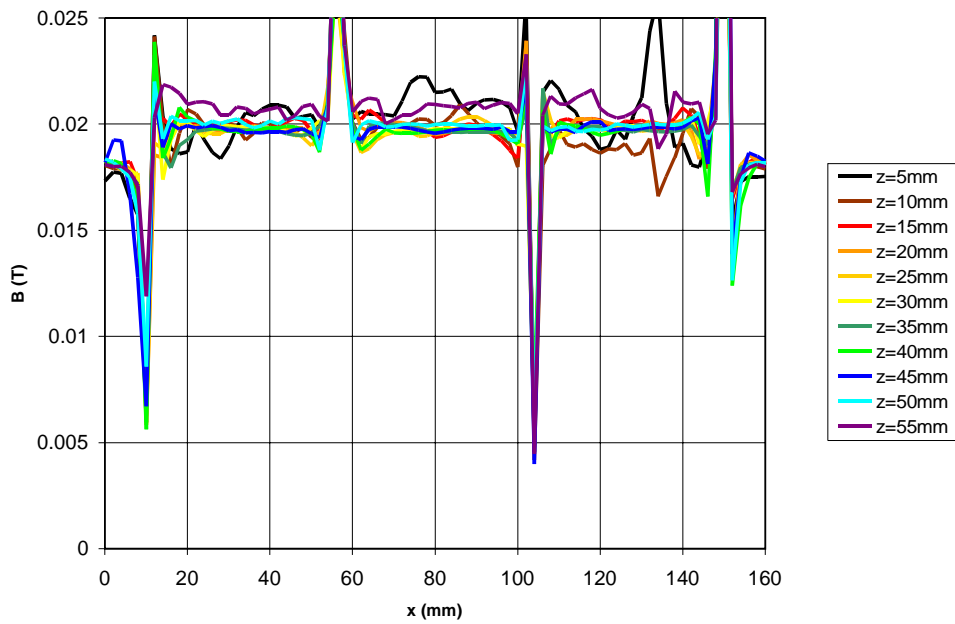


Fig. 9.2: Tuning field for $I=2 \times 200A$, $f=50Hz$

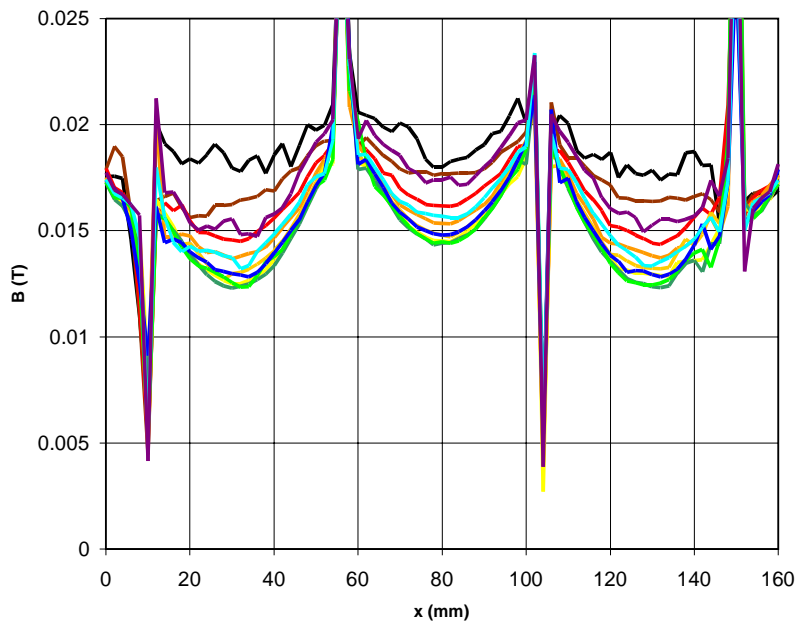


Fig. 9.3: Tuning field for $I=2 \times 200A$, $f=500Hz$

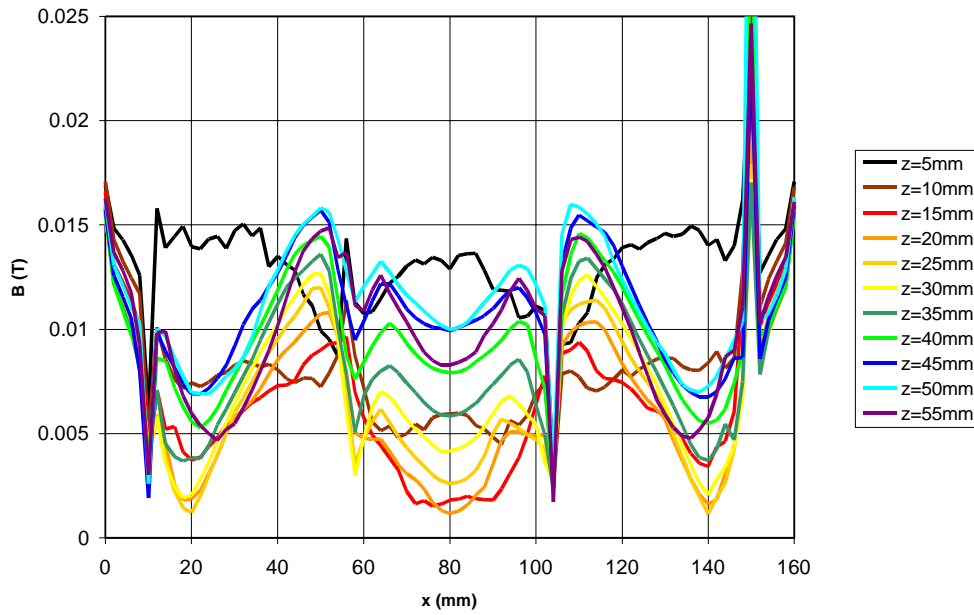


Fig. 9.4: Tuning field for $I=2 \times 200A$, $f=2kHz$

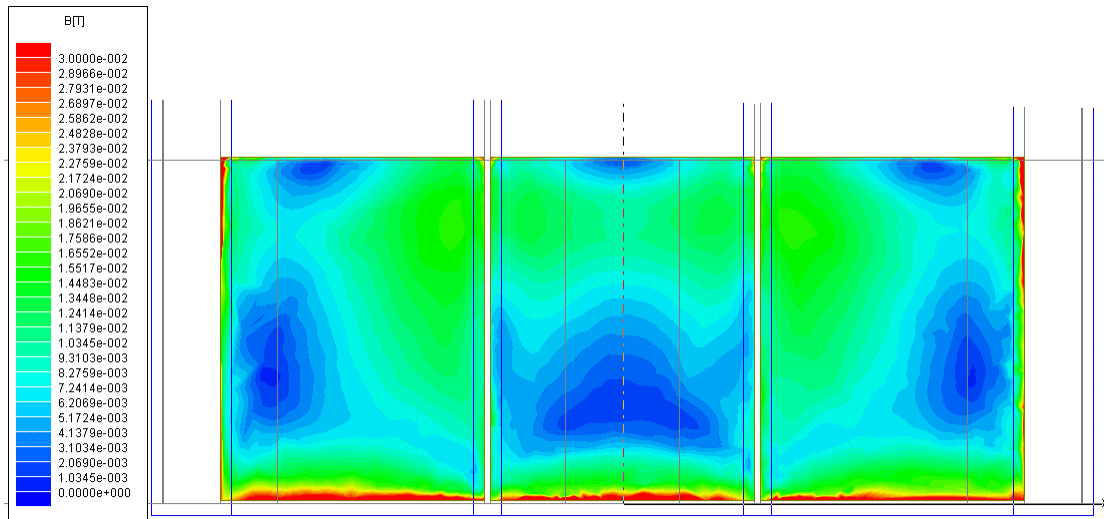


Fig. 9.5: Bias field for $I=2 \times 200A$, $f=2kHz$

At 50Hz (see Fig. 9.2), the field reaches the nominal value and is uniform over whole structure. At 500Hz (Fig. 9.3), the field starts to be deformed, but it is still quite uniform with mean value of approx ± 170 Gauss, still giving almost full phase-tuning stroke. At 2kHz the field penetration is much degraded (Fig. 9.4, Fig. 9.5), with mean value slightly above ± 60 Gauss, and very non-uniform giving significantly reduced phase-tuning stroke.

A special structure with interlaced slots was developed to minimize the eddy currents influence, but it has not yet been implemented in the first prototype phase-shifters, which have been built. The magnetic field distribution at 2kHz tuning frequency is shown in Fig. 9.6. In the simulations the new structure is promising almost full tuning range, even at 2kHz,

where the original structure has nearly no phase-shift available. However, the interlaced structure is more difficult to build and hence it will be more expensive.

The measured phase-tuning frequency response of the realised device is shown in Fig. 9.10.

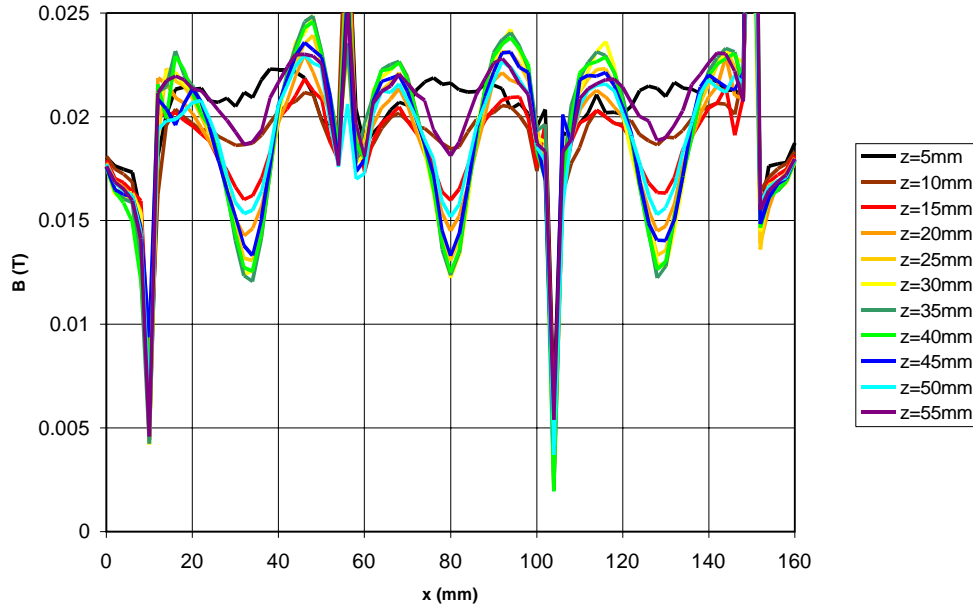


Fig. 9.6: Bias field for $I=2 \times 200A$, $f=2kHz$, a specially optimized structure

9.2 Power requirements for phase tuning

Another important parameter, characterizing the phase-shifter device is the power needed to tune the phase. The magnetic circuit of the phase-shifter is using a special magnetically soft transformer steel, capable to work at higher frequencies ($\sim kHz$). The DC bias point of the ferrites is set by permanent magnets to 2000 Gauss. Some experiments with the ferrite magnets were done, but their low magnetic retentivity (below 3kGauss) makes the magnetic circuit very bulky, and NdFeB magnets were finally used. However, the NdFeB magnets are quite conductive at the expected tuning frequencies (see Table 9.1), so their shape must be optimized to suppress the eddy currents and hence the self-heating effects.

The variable tuning field is produced by a pair of coils. By numerical simulations a total current of $2 \times 200A$ was found to produce the required tuning field of ± 200 Gauss. From the same simulation the total stored energy in the system can be found and the power requirements for the phase tuning can be estimated. Using an iterative process, the magnetic circuit, or even the RF structure can be optimized in order to lower the magnetic stored energy to a reasonable value.

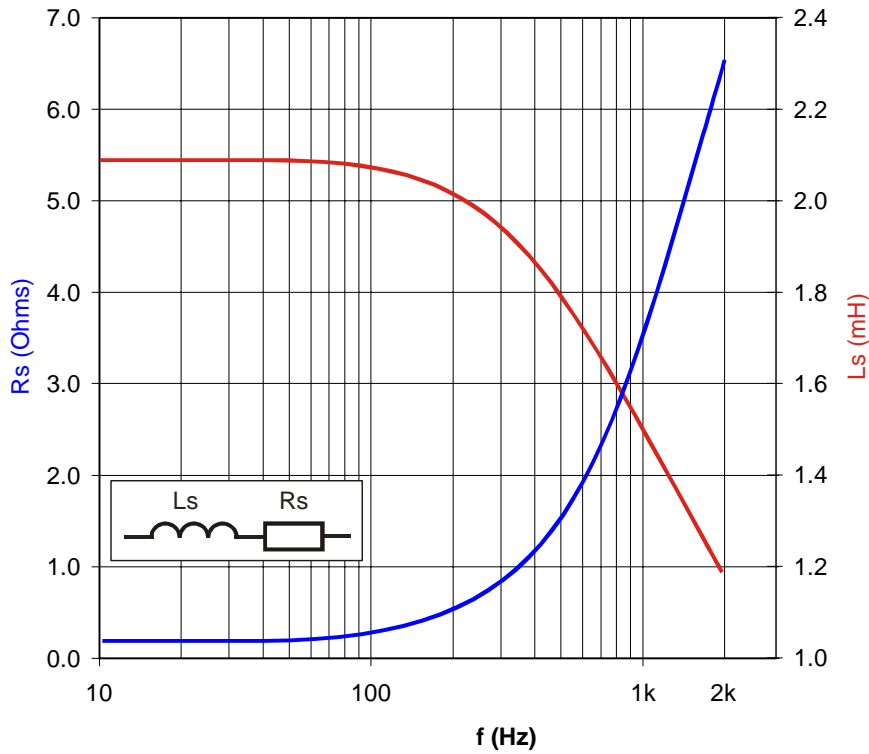


Fig. 9.7: Impedance of the tuning coil as a function of frequency

The power requirements for the phase tuning, when the phase-shifter is supplied by the ideal sinusoidal current source of $I_{\text{peak}}=12\text{A}$ are calculated in the Table 9.2. U_{peak} stands for the peak voltage of the current source, P_{supply} is the power delivered to the structure and P_{losses} is the power dissipated in the loss resistance of the equivalent circuit (in fact it represents the losses in coils, magnetic circuit and losses caused by the eddy currents in the structure). In the low frequency region, the DC losses of the coil are dominating, and only very little power is needed to tune the phase. For the high frequencies the eddy current losses are dominant and a significant part of the delivered power is dissipated in the structure.

f (Hz)	L_s (mH)	R_s (Ohm)	U_{peak} (V)	P_{supply} (W)	P_{losses} (W)
1	2.085	0.181	2.2	15.9	15.9
50	2.085	0.181	8.1	37	15.5
100	2.074	0.252	15.8	70	22
200	2.015	0.492	30.8	136	43.4
500	1.792	1.661	70.4	322	146.6
1000	1.492	3.671	120.6	576	323
2000	1.184	6.567	194.7	952	578

Table 9.2: The phase tuning power requirements

If the structure will be supplied by a four-quadrant power supply, the operation of the phase-shifter will be energy efficient, because the energy stored in the magnetic circuit can be

recuperated back to the power supply and reused. For tests, the Copley Controls Model 220 [76] switching amplifier, capable of delivering $\pm 75\text{V}/12\text{A}$ in four-quadrant mode was used.

9.3 Technical specifications of the CERN fast ferrite phase-shifter

In collaboration with company AFT, two prototypes of the fast ferrite phase-shifters have been developed and built. Basic required technical parameters of the phase-shifters are listed in the Table 9.3.

Parameter	Required value	Measured value
Mode of operation	Reflective resonant type	
Peak power	>125kW, full reflection tolerant	High power tested at 400MHz/240kW peak power, 60kW r.m.s. OK
R.m.s. power	>30kW (25% duty cycle)	
RF Pulse repetition freq.	50Hz	
Insertion loss	<0.1dB	0.15dB
RF operation frequency	352MHz	
Diff. phase-shift range	>90°	>125°
Tuning speed	>1kHz for 70% of full scale phaseshift	75% of full scale phase-shift at 1kHz

Table 9.3: Technical parameters of the CERN SPL phase-shifter

The actually achieved RF and tuning parameters of the built prototypes are shown in

- Fig. 9.8 – the attenuation as function of frequency and tuning current
- Fig. 9.9 – differential phase-shift as function of the tuning current
- Fig. 9.10 – Phase tuning frequency response, normalized to the DC full-scale value

Since the power supply (switching amplifier) output voltage is limited to $\pm 75\text{V}$, the frequency response was measured with the peak current of 5A, assuring the amplifier was operating in the linear mode.

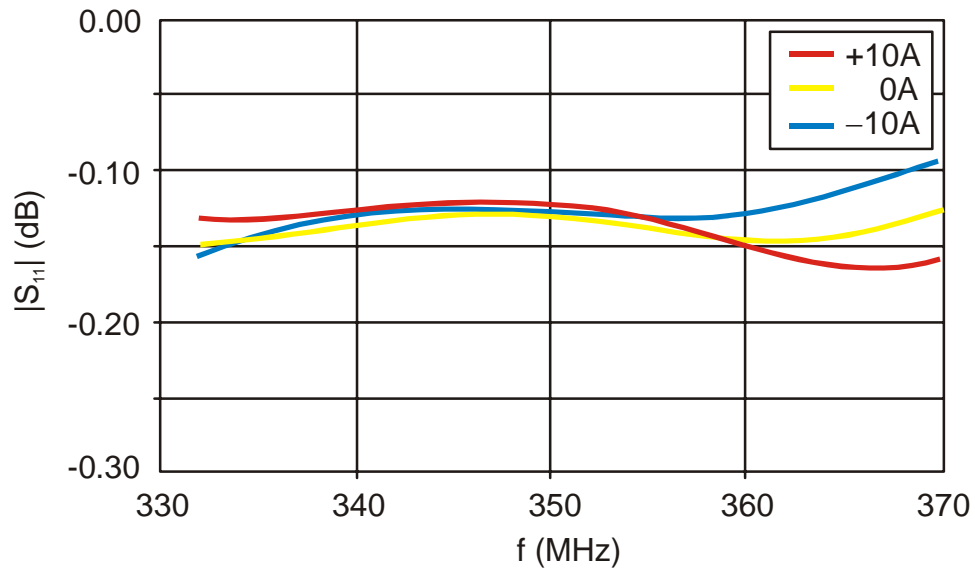


Fig. 9.8: Attenuation as function of frequency and tuning current

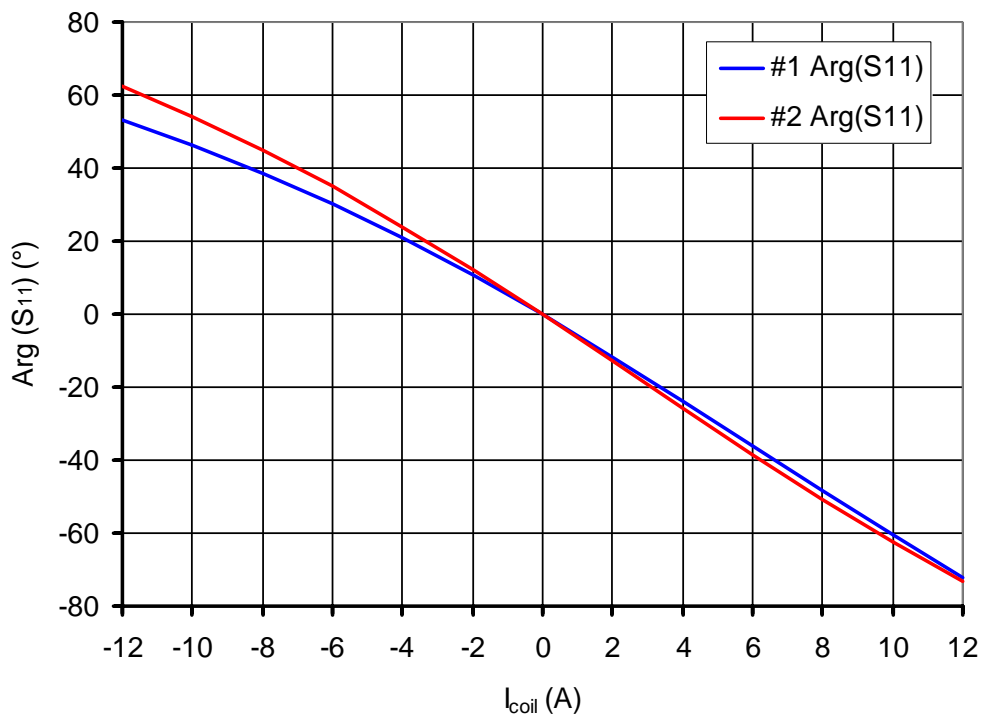


Fig. 9.9: Phase as function of tuning current (both prototypes, curves are shifted to have zero phase-shift for zero current)

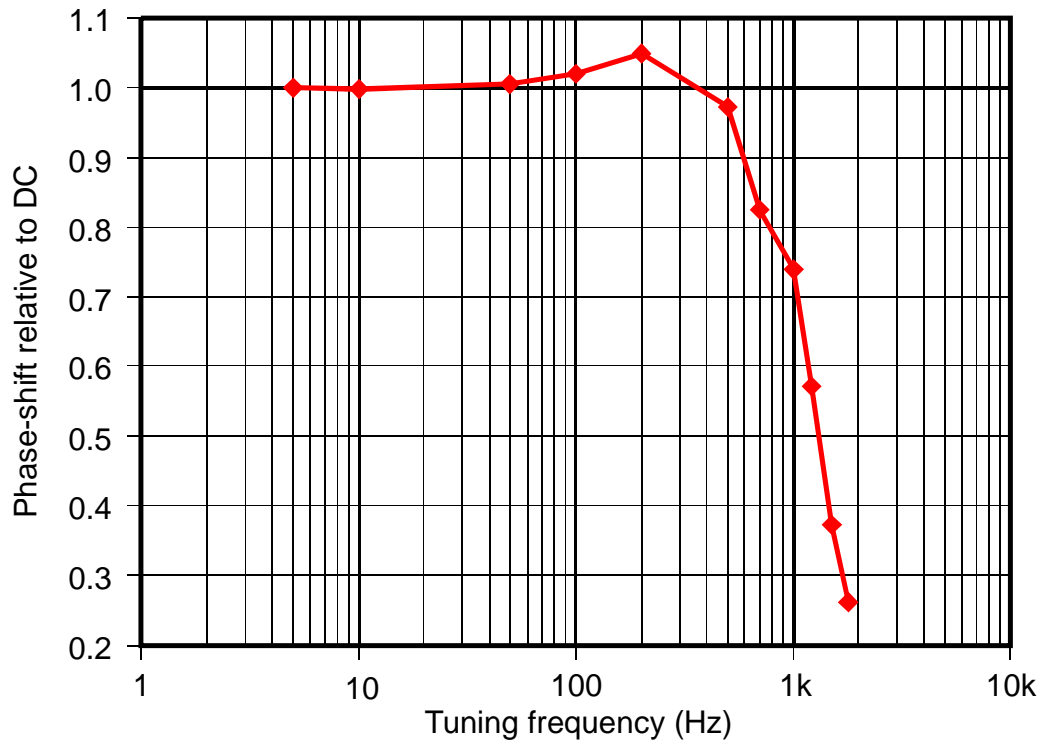


Fig. 9.10: The measured phase-tuning frequency response of the realised phase-shifters

10

First results with the phase and amplitude modulator that has been built

A complete unit of phase and amplifier modulator was built and tested in order to prove the theoretical principles calculated in the chapters 6 and 8. The measured transmission coefficient of the modulator shown in Fig. 6.13 as a function of the tuning currents is shown in Fig. 10.1.

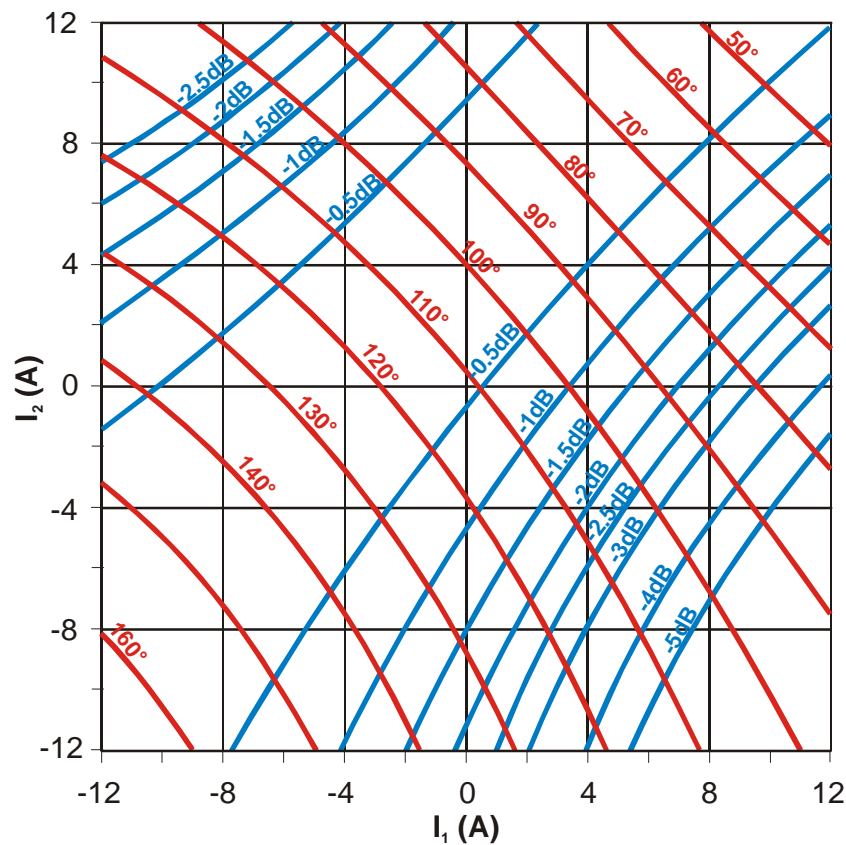


Fig. 10.1: Measured transmission function controlling capabilities of the modulator

As the phase of the phase-shifter is not exactly a linear function of the tuning current (see Fig. 9.9), the curves are slightly bended. In order to achieve a higher amplitude reduction, a permanent offset of about 20° was installed in series with the phase-shifter number two, as can be seen from the shifted system of transmission curves in Fig. 10.1.

11

Conclusions and outcomes from the dissertation thesis

RF and microwave technology is a crucial part of any particle accelerator, because the acceleration itself and many other operations on the particle beam are carried out using RF fields. This present work is dedicated to the high power microwave technology used for particle acceleration. As an introduction to particle accelerator technology, a summary of the fundamentals of microwave technology used in particle accelerators has been presented, with particular focus on microwave cavity resonators.

A technique to determine the fields inside cavities (small perturbation theory) was described. In addition a method to calculate the change in resonant frequency caused by a mechanical deformation of the cavity (Slater's theorem) was shown. Also, a brief introduction to the properties and behaviour of superconducting cavities was given, focusing on the Lorentz force detuning phenomenon (section 4.1).

For classical accelerators, working with CW signals, the Lorentz force detuning is static and compensated by the tuning system. The proposed SPL accelerator will use superconducting cavities in pulsed mode. However, pulsed operation of the superconducting cavities, as only recently considered, results in dynamic detuning effects.

Each cavity with its ancillary equipment is also a mechanical resonator and the Lorentz forces linked to the pulsed RF fields will excite the mechanical modes of this object. The excited amplitudes may become large when a multiple of the pulsing frequency is close to a mechanical resonance. A vector-sum feedback system (Fig. 4.7) will add the voltages from all the cavities fed by one transmitter, resulting in a signal which is equivalent to what the beam sees from this group of cavities. This signal is fed back to the transmitter to stabilise the total field. If there is more than one cavity connected to the transmitter, the system is not completely defined. The vector-sum feedback stabilises only the sum of the voltage, but not the voltage in each individual cavity.

For low excitation the practically identical cavities behave identically and the cavity voltages are equally distributed between the cavities. However as discovered by Tückmantel [33],

above a certain threshold, this is no longer the case. The cavities can behave differently, some delivering more voltage, some less. A mathematical analysis [34] has shown that this is a real effect and not a simulation artefact. To avoid this problem, control of each individual cavity voltage is necessary. A solution, to control the phase and amplitude of the incident wave for each cavity, was proposed by Frischholz [35]. A more detailed description of his proposal is given in section 4.6.

A cost-effective way to supply several cavities by one transmitter while keeping the possibility of controlling the field in each individual cavity is by introducing a fast phase and amplitude modulator – also called a “Transmission Controlling Device” – into each cavity feeder line. This device is capable of simultaneously controlling the phase and amplitude of the passing wave. In this way the modulator will compensate the individual deviations of each cavity in order to equalize their behaviour for the main control loop, which will compensate the average detuning of whole system.

Four different types of phase and amplitude modulators have been analyzed in chapter 6:

1. Modulator using a single 180° hybrid and reflective type phase-shifters (section 6.2.1)
2. Modulator using a single quadrature hybrid and reflective type phase-shifters (section 6.2.5)
3. Modulator using two 180° hybrids and transmission type phase-shifters (section 6.3.1)
4. Modulator using two quadrature hybrids and transmission type phase-shifters (section 6.3.2)

A summary of the properties of each structure is given in Table 6.1. With a matched load the overall properties of the modulators are – except for the fixed $\pi/2$ phase offset – the same (equations (6.20), (6.21) for case 1, equations (6.34), (6.35) for case 2, equations (6.53), (6.54) for case 3 and equations (6.67), (6.68) for case 4).

Single hybrid modulators have an output signal that depends on the load reflection factor, which must be considered when designing the system. If the mismatch of the load is so large that the additionally induced standing wave dominates the primary wave, the system may become uncontrollable. This is exactly the case for the superconducting cavity, which in the loading state before a beam arrives reflects the full incident wave back to the generator. The only safe solution is to introduce a circulator between the modulator and the cavity, assuring the modulator always ‘sees’ the matched load.

The single hybrid structure works with the reflective type of phase-shifters, which are in the domain of lower frequencies. The whole modulator is then quite compact in comparison to the double hybrid configuration.

Two hybrid modulator structures are more complex, but have some favourable properties. The output signal is independent of the output load, so amplitude and phase are only a function of the controlling quantities (i.e. the phase-shifts of both phase-shifters). The amplitude and/or phase modulation do not produce any reflections back to the generator. Also the structure uses the transmission type of phase-shifters, which are easier and more economic to build for higher frequencies.

A comparison of different types of ferrite phase-shifters and their properties is given in Table 7.1. However, for the high power and high phase tuning speed applications, only some of them are suitable. For lower average RF power, a two-slab waveguide configuration is applicable (Y. Kang [63]). However when moving towards the high average power region, only the coaxial structures are suitable. For the CERN application, a coaxial type phase-shifter working above the ferrite's gyromagnetic resonance was chosen (see Fig. 7.6).

The ferrite loaded strip-line structure with its variable electrical parameters is introduced in chapter 8. The parameters of such a transmission line (with focus on the variable impedance and propagation constant) have been evaluated for various geometries. Use of such a line in different phase-shifter configurations is shown for the reflection type and transmission type of the phase-shifter.

The behavior of the variable impedance line, represented by the ferrite loaded strip-line, shorted at one end and connected to the impedance mismatched port, is analyzed in section 8.7.2. In sections 8.7.3, 8.7.4 and 8.7.5 a differential phase-shift as a function of structural parameters was examined. Section 8.7.6 was devoted to the analysis of the electric field loading of such a structure in order to ensure proper operation without RF breakdown.

The constraints of the ferrite loaded strip-line structure are a very broad compromise between the RF parameters, phase tuning speed and the power required to perform this tuning. A simple variable impedance line configuration is not necessarily always the most appropriate solution, so another configuration with a second transmission line was also analyzed.

Inserting an additional transmission line with different electrical parameters (fixed line) may help to overcome disadvantages of the simple line phase-shifter, as well as providing other useful characteristics. With this additional degree of freedom, a better compromise between

the structure parameters of the phase-shifter may be achieved; this has been shown in section 8.8.

The transmission type of coaxial phase-shifter represented by the ferrite loaded strip-line working in the transmission mode is analysed in section 8.9. The differential phase-shift and the impedance mismatch caused by the phase tuning have been calculated.

Finally, an introduction to the problem of thermal loading of the ferrite loaded strip-line was presented in section 8.10. An analytical form of the equation describing the temperature distribution has been derived and computer simulations with real structure parameters have been performed.

The CERN fast ferrite phase-shifter is introduced in chapter 9. Aspects regarding the phase tuning speed and the power needed to perform this tuning are explained.

The phase tuning speed, as a parameter of the phase-shifter is discussed in chapter 9. It has been shown that the variable permeability ferrite region of the phase-shifter must be properly DC biased in order to achieve the correct working point and hence low RF losses. The ferrite region must also be properly penetrated by the tuning magnetic field in order to achieve a good tuning performance. As the RF structure has to be entirely surrounded by the “RF tight” housing using a highly conductive material, the penetration quality and efficiency of the variable tuning field is strongly influenced by the eddy currents in the strip-line structure and the magnetic circuit.

In order to minimize the eddy currents, the inner and outer conductor of the strip-line structure is slotted. The number of slots, and their position was optimized by computer simulations for the best compromise between the electrical performance and the manufacturing effort. As the tuning frequency increases, less and less of the magnetic field penetrates into the ferrite region and the distribution of the magnetic field is not uniform. The tuning field distribution as a function of tuning frequency is shown in Fig. 9.2, Fig. 9.3, Fig. 9.4 and Fig. 9.5. The variable tuning field is produced by a pair of coils. By numerical simulations a total current of 2x200A was found to produce the required tuning field of ± 200 Gauss. From the same simulation the total stored energy in the system was found and the power requirements for the phase tuning were estimated. The power requirements for the phase tuning, when the phase-shifter is supplied by the ideal sinusoidal current source of $I_{\text{peak}}=12\text{A}$ are calculated in the Table 9.2. In the low frequency region, the DC losses of the coil dominate, and only very little power is needed to tune the phase. For high frequencies the

eddy current losses are dominant and a significant part of the delivered power is dissipated in the structure.

Two prototype phase-shifters were constructed. Their measured RF and tuning parameters are presented in Fig 9.8, Fig 9.9, and Fig 9.10. The low level and high power tests proved that both of the phase-shifters that were built fulfil the required specifications listed in Table 9.3. The measurements show that there is still about 75% of full-scale phase-shift available at 1kHz tuning frequency.

A complete unit of the phase and amplitude modulator shown in Fig. 6.13 has been built and tested in order to prove the theoretical principles analysed in chapters 6 and 8. The measured transmission coefficient of the modulator as a function of the tuning currents is shown in Fig. 10.1. In order to achieve a higher amplitude reduction, a permanent offset of about 20° was installed in series with the phase-shifter number two, as can be seen from the shifted system of transmission curves in Fig. 10.1.

Outcomes of this thesis:

- A proposal for a system to drive several superconducting cavities by a single large transmitter while keeping control of amplitude and phase of the field in all individual cavities. This is a financially competitive alternative to the classical system of “one cavity per transmitter”.
- The necessary technical solution for compensation of dynamic detuning effects in superconducting cavities due to high internal electromagnetic fields (Lorentz force detuning) by a transmission controlling device using RF hybrids and fast ferrite phase-shifters.
- The mathematical analysis, design and optimization of adequate fast ferrite phase-shifters for a high power RF application, controlled by limited ferrite biasing power.

Original results:

- Based on [35] a proposal of the required transmission controlling device allowing separate control of the field in each individual cavity when all cavities are powered by one transmitter.

- Mathematical analysis and detailed study of different types of phase and power modulators, which can be used under the specific conditions of high power accelerator RF system.
- Analysis of the phase and power modulator's behaviour when working with a fully reflective load represented by a superconducting cavity resonator.
- Detailed study and mathematical analysis of different types of phase-shifting structures suitable for use in such a system, both reflection and transmission types.
- Design and optimization of the phase-shifter's structure with respect to eddy currents. Minimization of their effects in order to obtain high tuning speeds with only limited ferrite biasing power.
- Development and optimization of a special slotted structure lowering the eddy current effects that are present in the phase-shifter device.

Benefits of the work:

The proposed, analysed, designed and built device will allow the feeding of several superconducting cavities by a more economical single large transmitter while keeping individual control of field amplitudes and phases of all cavities. The phase and amplitude modulator will allow compensation of the dynamic detuning effects of the superconducting cavity resonators caused by the high internal electromagnetic fields.

CERN is the first laboratory world-wide where such a device was designed and built. It will be tested in a real RF accelerator system with a superconducting cavity in the coming months.

Apart of scientific accelerators, phase-shifter devices are interesting for other high power RF applications such as:

- Fast impedance matching systems for nuclear fusion reactors.
- Medical accelerators for cancer treatment
- Tuning and matching devices for industrial microwave heating systems.
- Plasma applications.

Theses for future work:

- Detailed analysis of the dynamic performance of a system equipped with the transmission controlling devices.
- Analysis of the stability of a full system equipped by one transmitter and multiple (4 or 8) superconducting cavities working in the pulsed mode.
- Implementation of the feed-forward algorithms in order to shorten the field stabilisation time in the cavity.
- Further improvements in the phase-tuning performance (speed, lowering the power needs).

References

- [1] Experimental High Energy Physics, Ohio State University web page, http://www.physics.ohio-state.edu/research/he_experiment.html
- [2] CERN, laboratory's internet homepage, www.cern.ch
- [3] DESY, laboratory's internet homepage, www.desy.de
- [4] Fermilab, laboratory's internet homepage, www.fnal.gov
- [5] SLAC, laboratory's internet homepage, www.slac.stanford.edu
- [6] KEK, laboratory's internet homepage, www.kek.jp
- [7] Brüning O.: Accelerators IV, web archive of the CERN Summer Student Lectures 2003, <http://bruening.home.cern.ch/bruening/>
- [8] Brüning O.: Accelerators II, web archive of the CERN Summer Student Lectures 2003, <http://bruening.home.cern.ch/bruening/>
- [9] Tirpák A.: Elektrina a magnetizmus II, UK Bratislava 1997, ISBN 80-223-1103-0
- [10] English translation of the Einstein A.: Zur Elektrodynamik bewegter Körper. Annalen der Physik. 17:891, 1905
- [11] Bottura L.: From the LEP Warm Magnets to the LHC Superconducting Magnets, CERN Chamonix conference, January 2000
- [12] M. Letournel and the Vivitron Group: The Strasbourg Project. A 35MV Vivitron Tandem. In IEEE 1987 Particle Accelerator Conference, Washington D.C., March 1987, pp. 346-348
- [13] Colin, Robert E.: Foundations for Microwave Engineering, second edition. McGraw-Hill 1992, ISBN 0-07-112569-8
- [14] Krusche A., Paoluzzi M.: The new low frequency accelerating systems for the CERN PS Booster. In 6th European Particle Accelerator Conference, June 22 - 26, 1998, Stockholm, Sweden
- [15] Cheng, David K.: Field and Wave Electromagnetics, second edition. Addison-Wesley publishing company 1992, ISBN 0-201-12819-5.
- [16] Pozar, David M.: Microwave Engineering. Addison-Wesley Publishing Company 1993, ISBN 0-201-50418-9.
- [17] Gardiol F.: Introduction to microwaves. Artech House inc. 1984, ISBN 0-89006-134-3.
- [18] Gilmour A.S. (jr.): Microwave tubes. Artech House inc. 1986, ISBN 0-89006-181-5.
- [19] Computer simulation technology GmbH, Darmstadt, Germany. www.cst.de
- [20] SUPERFISH
- [21] Wilson, P.: High Energy Electron Linacs: Applications to Storage Ring RF Systems and Linear Colliders. SLAC-PUB-2882, 1982

- [22] Slater, J.C.: Microwave electronics. *Reviews of Modern Physics*, October 1946, Volume 18, Issue 4
- [23] Tückmantel J., Haebel E.: Electromagnetic surface forces in RF cavities. CERN internal note CERN-AT-RF-91-99. Was never officially published.
- [24] Multiple authors: Accelerator design report for J-PARC. KEK Japan, March 2003, <http://hadron.kek.jp/member/onishi/tdr2003/>. Chapter 3.1.2.6
- [25] Whittum D.H.: Introduction to Electrodynamics for Microwave Linear Accelerators. Stanford Linear Accelerator Center, internal publication SLAC-PUB-7802, April 1998
- [26] Whittum D.H.: Introduction to Microwave Linacs. Stanford Linear Accelerator Center, internal publication SLAC-PUB-8026, December 1998
- [27] Proudlock P.: LEP200 Design report. SL-PC-Tech-Note-91-87, CERN, Geneva, Jun 1991
- [28] CEBAF – The Continuous Electron Beam Accelerator Facility. Jefferson National Laboratory, www.jlab.org
- [29] Edwards D. A.: TESLA Test Facility Linac - Design Report. DESY Laboratory Report TESLA 95-01, March 1995.
- [30] Garoby R., Vretenar M.: Proposal for a 2 GeV Linac Injector for the CERN PS. CERN PS/RF/Note 96-27.
- [31] Frischholz H.: The LEP RF power plant. In: 7th LEP Performance Workshop, Chamonix, France, January 1997
- [32] Boussard D.; Brown P.; Tückmantel J.: Electroacoustic oscillations in the LEP superconducting cavities. In: 5th European Particle Accelerator Conference EPAC'96 , Sitges, Barcelona, Spain, Jun 1996. Pp: 2097-2099
- [33] Tückmantel J.: 'SPLinc', A Program to Simulate SC Linac RF System with Beam. CERN SL Note 2000-053-HR
- [34] Tückmantel J.: Control Instabilities in a Pulsed Multi-Cavity RF System with Vector Sum Feedback (A Mathematical Analysis). CERN-SL-Note-2001-023 HRF and CERN NUFACT Note 082
- [35] Frischholz H.: private communications
- [36] Tückmantel J.: Proposal for the Control of a Multi-Cavity RF System with One Transmitter. CERN note AB-Note-2003-055 (SPL)
- [37] Culshaw W.: Resonators for Millimeter and Submillimeter Wavelengths. 1961 *Transactions on Microwave Theory and Techniques* 9.2 (Mar. 1961 [T-MTT]): 135-144.
- [38] A. Chatterjee, J.M. Jin and J.L. Volakis. "Computation of Cavity Resonances Using Edge-Based Finite Elements (Short Papers)." 1992 *Transactions on Microwave Theory and Techniques* 40.11 (Nov. 1992 [T-MTT]): 2106-2108.
- [39] Padamsee, H.: Review of experience with HOM damped cavities. Laboratory of Nuclear Studies, Cornell University, Ithaca, NY 14853, U.S.A, Presented at the 1998 European Particle Accelerator Conference.

- [40] R.M. Kurzkro: Loaded Q of a Waveguide Cavity Resonator (Comments). 1967 Transactions on Microwave Theory and Techniques 15.3 (Mar. 1967 [T-MTT]): 192-193.
- [41] Kenji Saito: Lecture Notes: Superconducting RF Cavity for Linacs, KEK, Accelerator Lab. Lecture course given at Nagoya Univeristy, July, 2004
- [42] Ilyinski A.S., Slepyan G. Ya: Propagation, Scattering and Dissipation of Electromagnetic Waves. P. Perigrinus on behalf of the Institution of Electrical Engineers, London, 1993. ISBN: 0 86341 283 1
- [43] Jakes W.C., Jr.: Analysis of Coupling Loops in Waveguide and Application to the Design of a Diode Switch. 1966 Transactions on Microwave Theory and Techniques 14.4 (Apr.1966 [T-MTT]): 189-200.
- [44] Ghose R.N.: Excitation of Higher Order Modes in Spherical Cavities. 1957 Transactions on Microwave Theory and Techniques 5.1 (Jan. 1957 [T-MTT]): 18-22.
- [45] H.P. Kindermann, et al.: Status of RF Power Couplers for Superconducting Cavities at CERN. Proceedings of the 5th European Particle Accelerator Conference, Sitges, Barcelona, Spain, June 1996, pp. 2091-2093.
- [46] Zhao, Z T, et al.: Design of a Copper Cavity for HLS. In: IEEE Particle Accelerator Conference PAC '01, Chicago, IL, USA , 18 - 22 Jun 2001 - pages e-proc. 1201
- [47] Achard, C; Braun, H H; Döbert, S; Syratchev, I; Taborelli, M; Wilson, I; Wunsch, W: A Demonstration of High-Gradient Acceleration. Presented at: Particle Accelerator Conference PAC 2003 , Portland, OR, USA , 12 - 16 May 2003
- [48] Tsuyoshi Tajima: Superconducting Cavities for High Power Accelerators. Los Alamos National Laboratory, web link: laacg1.lanl.gov/scrflab/pubs/APT/LA-UR-01-4058.pdf
- [49] R.L. Geng, A. Crawford, G. Ereemeev, H. Padamsee, J. Sears: A 1500 MHz Niobium Cavity Made of Electropolished Half-cells, Presented at: Particle Accelerator Conference PAC 2003 , Portland, OR, USA , 12 - 16 May 2003. Pp. 1312-1314
- [50] P. Sekalsky, S. Simrock, L. ilje, C. Albrecht: Lorentz Force detuning compensation system for accelerating filed gradients up to 35 MV/M for superconducting XFEL and Tesla nine-cell cavities. CARE-Conf-04-001-SRF,
- [51] Ayer D.R., Wheeler C.A.: The evolution of strip transmission line. Microwave journal, Vol. 12, No. 5, May 1969, pp. 31-40
- [52] Barrett R. M.: Microwave printed circuits – A historical survey. IRE Transactions on microwave theory and techniques, Vol. MTT-3, No. 2, March 1955, pp. 1-9
- [53] Wheeler H.A.: Transmission-Line Properties of Parallel Strips Separated by a Dielectric Sheet. 1965 Transactions on Microwave Theory and Techniques 13.2 (Mar. 1965 [T-MTT]): 172-185.
- [54] Ansoft corporation: Maxwell 2D, Maxwell 3D codes. www.ansoft.com
- [55] Wheeler H.A.: Transmission-Line Properties of Parallel Wide Strips by a Conformal-Mapping Approximation. 1964 Transactions on Microwave Theory and Techniques 12.3 (May 1964 [T-MTT]): 280-289.
- [56] Wheeler H.A.: Transmission-Line Properties of a Strip Line Between Parallel Planes. 1978 Transactions on Microwave Theory and Techniques 26.11 (Nov. 1978 [T-MTT]): 866-876.

- [57] Cohn S.B.: Characteristic Impedance of the Shielded-Strip Transmission Line. 1954 Transactions on Microwave Theory and Techniques 2.2 (Jul. 1954 [T-MTT]): 52-57.
- [58] Chen T.S.: Determination of the Capacitance, Inductance, and Characteristic Impedance of Rectangular Lines. 1960 Transactions on Microwave Theory and Techniques 8.5 (Sep. 1960 [T-MTT]): 510-519.
- [59] Cruz J.E., Brooke R.L.: A Variable Characteristic Impedance Coaxial Line (Correspondence). 1965 Transactions on Microwave Theory and Techniques 13. 4 (Jul. 1965 [T-MTT]): 477-478.
- [60] Hubing T.H.: Survey of Numerical Electromagnetic Modeling Techniques (Report TR91-1-001.3). September 1991, <http://www.emclab.umr.edu/pdf/TR91-1-001.pdf>
- [61] AFT company web page, www.aftgmbh.de
- [62] Aulock W. H., Fay C.E.: Linear Ferrite Devices for Microwave Applications, Supplement to Advances in Electronics and Electron Physics. Academic Press, New York, 1968
- [63] Kang Y.: Fast RF Ferrite Phase Shifter for High Power Applications. Argonne National Laboratory, Argonne, IL, U.S.A.
- [64] Aulock W.H.: Handbook of Microwave Ferrite Materials. Academic Press, New York, 1965.
- [65] Colin W., Davidson: Transmission Lines for Communications. John Wiley & Sons, 1978. ISBN 0-47099-160-7.
- [66] Bowick, Chris: RF circuit design. Newnes 1997, ISBN 0750699469
- [67] Chang K.: Handbook of Microwave and Optical Components. Wiley-Interscience, December 2001, ISBN: 0471210099
- [68] Ragan, George L.: Microwave Transmission Circuits. McGraw-Hill Book Company, New York, 1948
- [69] Nantista C.D., Fowkes N.M, et al.: Planar Waveguide Hybrids for Very High Power RF. Stanford Linear Accelerator Center, Stanford, CA
- [70] Pozar D. M.: Microwave and RF Design of Wireless Systems. Wiley Text Books, November 2000, ISBN: 0471322822
- [71] The NLC Design Group: Zeroth-Order Design Report for the Next Linear Collider, LBNL-PUB 5424, SLAC Report 474, and UCRL-ID 124161, May 1996.
- [72] S.G. Tantawi et al.: A Multi-Moded RF Delay Line Distribution System (MDLDS) for the Next Linear Collider. To be published in Physical Review-Special Topics.
- [73] Harwood L.: Improved Energy Efficiency Initiatives for Programmatic Equipment at Jlab.
- [74] Incropera F. P., DeWitt D. P.: Fundamentals of Heat and Mass Transfer. 5th Edition, Wiley Text Books, August 9, 2001. ISBN 0471386502
- [75] StarCD, simulation code for fluid dynamics (Simulation of Turbulence in Arbitrary Regions). <http://www.adapco-online.com/>
- [76] Copley Controls switching amplifier, model 220. Manufacturer's web site http://www.copleycontrols.com/high_power/downloads/pdf/220-230specs.pdf

- [77] Kraus, J. D., Fleisch D. A.: Electromagnetics with Applications, WCB/McGraw-Hill, 1999. ISBN 0-07-289969-7

Appendices

A. The ferrite material parameters	ii
B. Calculated transmission line parameters for the ferrite loaded line	iv
C. The rectangular resonant cavity.....	viii
D. The cylindrical resonant cavity	x
E. Photos of the phase-shifter that has been built	xiv
F. Photos of the phase and power modulator that has been built.....	xvi
G. Measured transmission controlling capabilities	xviii

Appendix A

The ferrite material parameters

B [Gauss]	μ'	μ''	$\tan \delta$
1560	4.43	0.049	0.0111
1600	4.20	0.044	0.0105
1700	3.62	0.031	0.0086
1800	3.09	0.019	0.0061
1900	2.75	0.011	0.0040
1992	2.53	0.0075	0.0030
2100	2.35	0.0058	0.0025
2280	2.12	0.005	0.0024

Table A.1: Ferrite material permeability as a function of the bias field

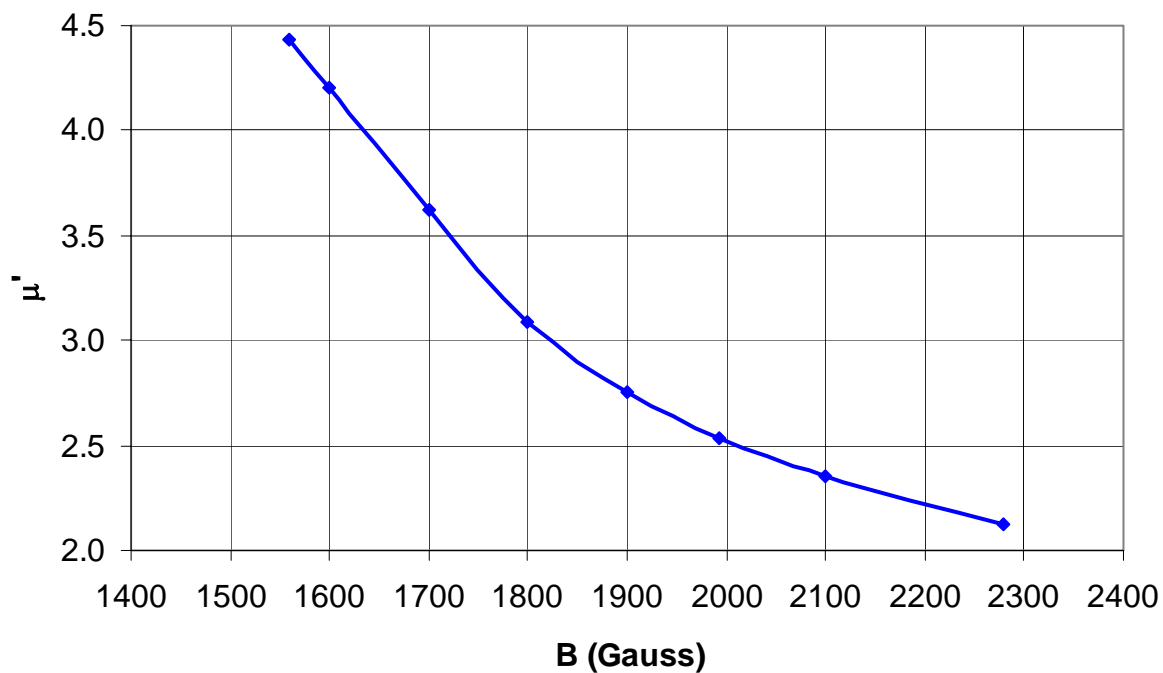


Fig. A.1: Real part of the permeability as a function of the bias field

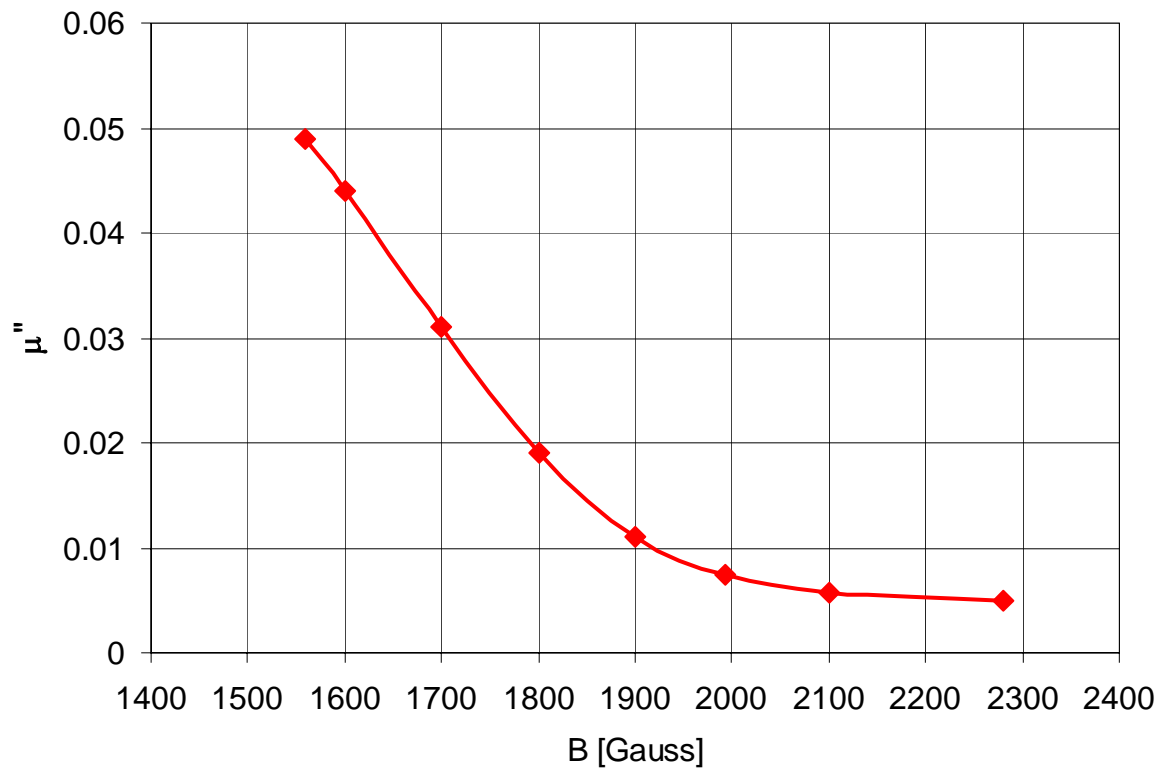


Fig. A.2: Imaginary part of the ferrite permeability as a function of the bias field

Appendix B

Calculated transmission line parameters for the ferrite loaded line

Fixed dimensions of the strip-line transmission line are $w=150\text{mm}$, $b=20\text{mm}$, $a=180\text{mm}$. The changing parameters are the thickness of the ferrite layer and the central conductor, as noted under each of the tables.

B (Gauss)	L (H/m)	C (F/m)	Z_0 (Ohm)	β (rad/m)	v_p (m/s)	v_p/c
1560	4.0660E-08	1.8030E-08	1.502	59.853	36933329	0.1231
1700	3.7097E-08	1.8030E-08	1.434	57.170	38666311	0.1289
1800	3.4434E-08	1.8030E-08	1.382	55.080	40133626	0.1338
1900	3.2690E-08	1.8030E-08	1.347	53.667	41190274	0.1373
1992	3.1549E-08	1.8030E-08	1.323	52.722	41928501	0.1398
2100	3.0593E-08	1.8030E-08	1.303	51.917	42578573	0.1419
2280	2.9391E-08	1.8030E-08	1.277	50.887	43440514	0.1448

Table B.1: Ferrite thickness $f=1.5\text{mm}$, metal conductor thickness $m=8\text{mm}$

B (Gauss)	L (H/m)	C (F/m)	Z_0 (Ohm)	β (rad/m)	v_p (m/s)	v_p/c
1560	4.8632E-08	1.3625E-08	1.889	56.903	38848180	0.1295
1700	4.3444E-08	1.3625E-08	1.786	53.782	41102368	0.1370
1800	3.9936E-08	1.3625E-08	1.712	51.565	42869603	0.1429
1900	3.7652E-08	1.3625E-08	1.662	50.069	44150713	0.1472
1992	3.6154E-08	1.3625E-08	1.629	49.062	45056097	0.1502
2100	3.4919E-08	1.3625E-08	1.601	48.217	45845936	0.1528
2280	3.3324E-08	1.3625E-08	1.564	47.103	46930284	0.1564

Table B.2: Ferrite thickness $f=2.0\text{mm}$, metal conductor thickness $m=7\text{mm}$

B (Gauss)	L (H/m)	C (F/m)	Z ₀ (Ohm)	β (rad/m)	v _p (m/s)	v _p /c
1560	5.6151E-08	1.0957E-08	2.264	54.831	40315813	0.1344
1700	4.9769E-08	1.0957E-08	2.131	51.621	42822766	0.1427
1800	4.5453E-08	1.0957E-08	2.037	49.332	44809788	0.1494
1900	4.2610E-08	1.0957E-08	1.972	47.764	46280538	0.1543
1992	4.0755E-08	1.0957E-08	1.929	46.713	47322069	0.1577
2100	3.9222E-08	1.0957E-08	1.892	45.826	48238001	0.1608
2280	3.7241E-08	1.0957E-08	1.844	44.654	49504366	0.1650

Table B.3: Ferrite thickness $f=2.5\text{mm}$, metal conductor thickness $m=6\text{mm}$

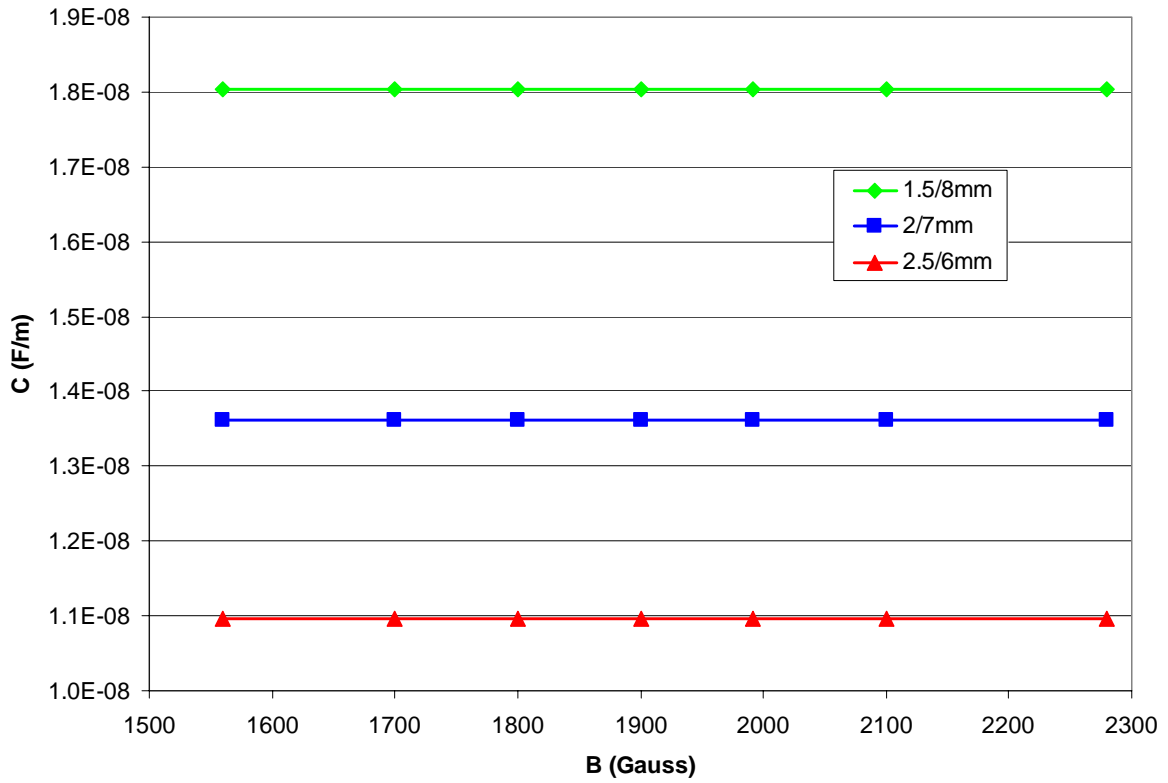


Fig. B.1: Capacity per unit length of the analysed strip-line

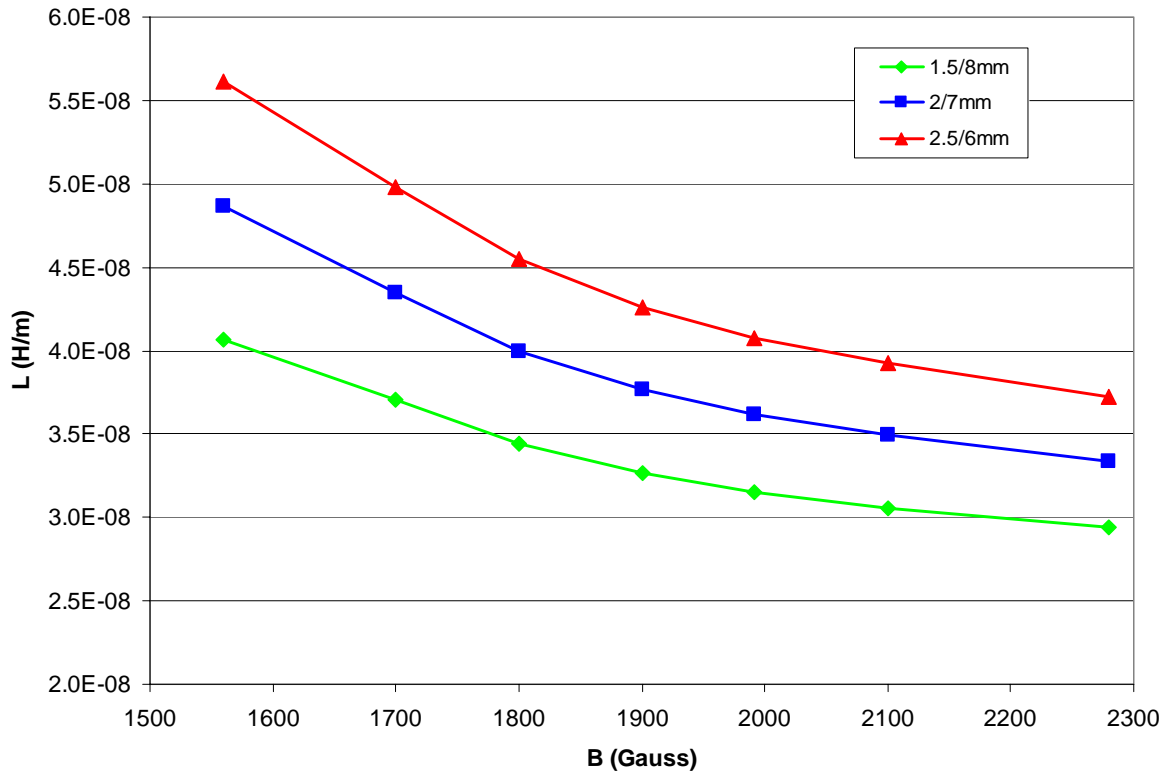


Fig. B.2: Inductance per unit length of the analysed strip-line

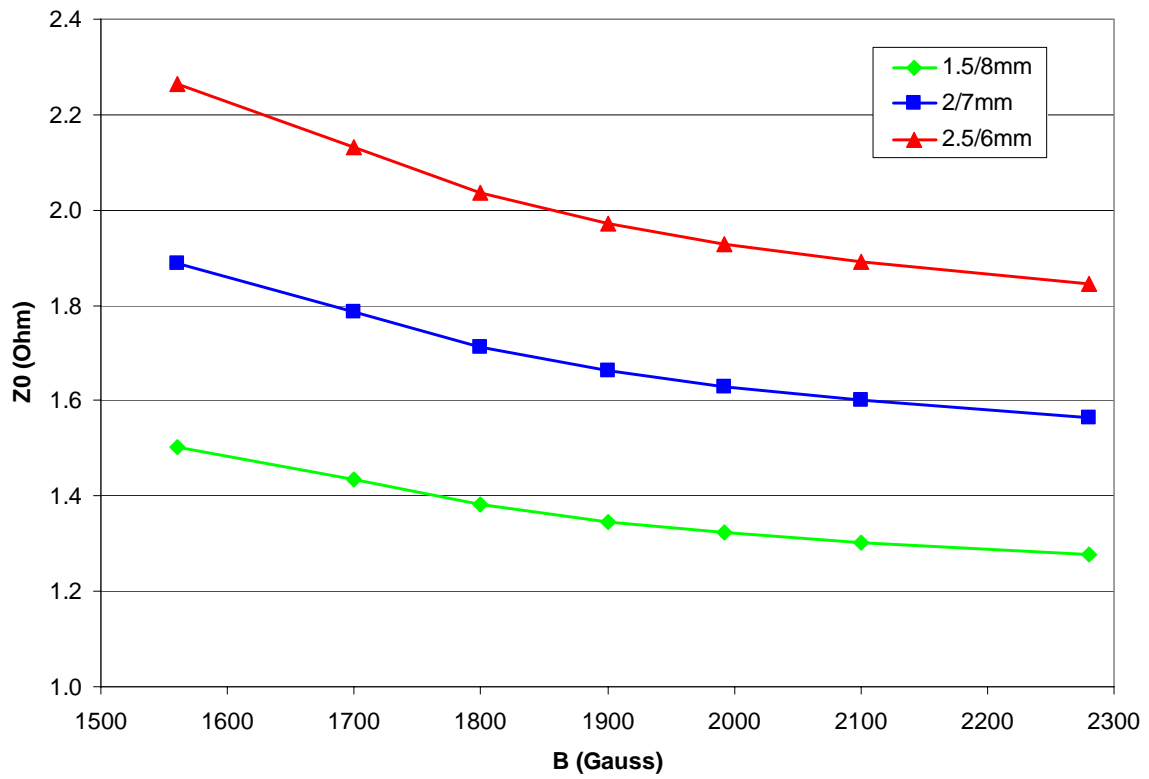


Fig. B.3: Impedance of the analysed strip-line

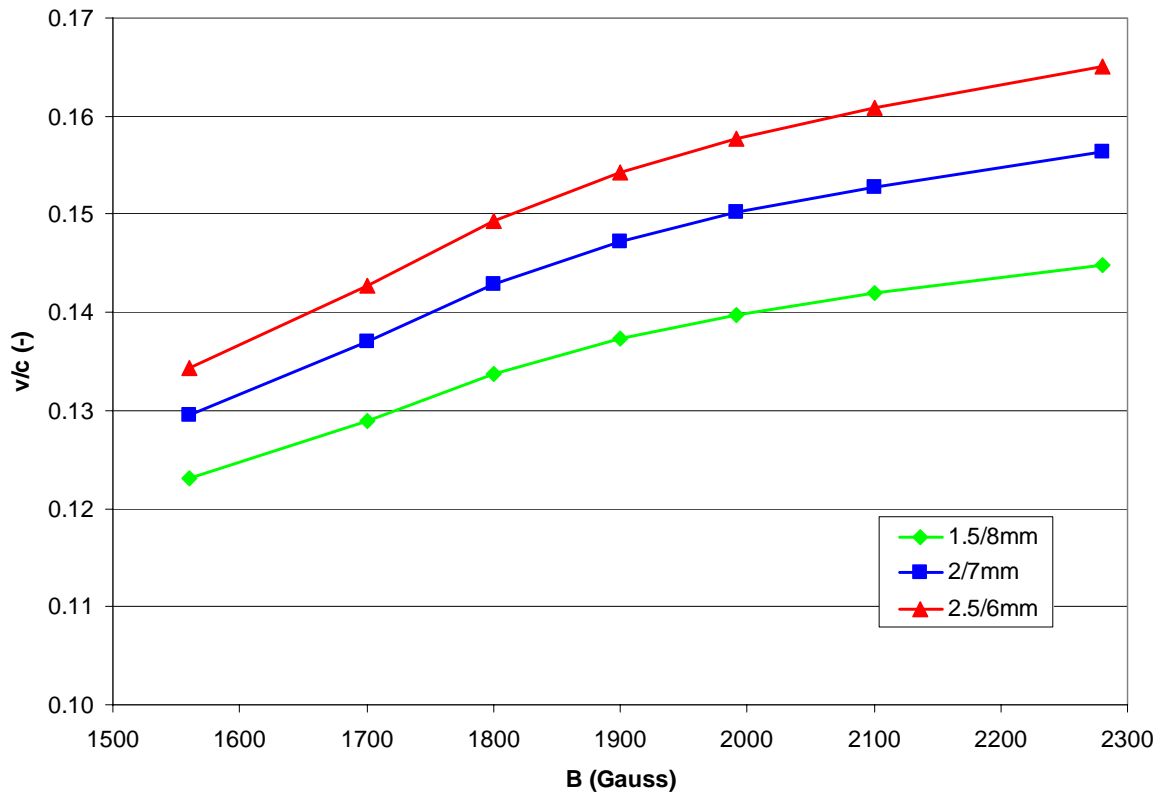


Fig. B.4: Relative propagation velocity on the analysed strip-line

Appendix C

The rectangular resonant cavity

The TM_{mnp} modes

From [16] we can write the following phasors of the field components for TM_{mnp} modes:

$$E_x(x, y, z) = -\frac{1}{h^2} \left(\frac{m\pi}{a} \right) \left(\frac{p\pi}{d} \right) E_0 \cos\left(\frac{m\pi}{a} x \right) \sin\left(\frac{n\pi}{b} y \right) \sin\left(\frac{p\pi}{d} z \right) \quad (C.13)$$

$$E_y(x, y, z) = -\frac{1}{h^2} \left(\frac{n\pi}{b} \right) \left(\frac{p\pi}{d} \right) E_0 \sin\left(\frac{m\pi}{a} x \right) \cos\left(\frac{n\pi}{b} y \right) \sin\left(\frac{p\pi}{d} z \right) \quad (C.14)$$

$$E_z(x, y, z) = E_0 \sin\left(\frac{m\pi}{a} x \right) \sin\left(\frac{n\pi}{b} y \right) \cos\left(\frac{p\pi}{d} z \right) \quad (C.15)$$

$$H_x(x, y, z) = \frac{j\omega\epsilon}{h^2} \left(\frac{n\pi}{b} \right) E_0 \sin\left(\frac{m\pi}{a} x \right) \cos\left(\frac{n\pi}{b} y \right) \cos\left(\frac{p\pi}{d} z \right) \quad (C.16)$$

$$H_y(x, y, z) = -\frac{j\omega\epsilon}{h^2} \left(\frac{m\pi}{a} \right) E_0 \cos\left(\frac{m\pi}{a} x \right) \sin\left(\frac{n\pi}{b} y \right) \cos\left(\frac{p\pi}{d} z \right) \quad (C.17)$$

where

$$h^2 = \left(\frac{m\pi}{a} \right)^2 + \left(\frac{n\pi}{b} \right)^2 \quad (C.18)$$

As for the rectangular waveguides, the integer numbers m , n and p define the number of half-wave variations of the field in the x , y and z direction.

A resonant frequency of the rectangular resonator is defined by the formula:

$$f_{mnp} = \frac{1}{2\pi\sqrt{\mu\epsilon}} \sqrt{\left(\frac{m\pi}{a} \right)^2 + \left(\frac{n\pi}{b} \right)^2 + \left(\frac{p\pi}{d} \right)^2} \quad (C.19)$$

The TE_{mnp} modes

From [14] we can write the phasors of the field components for TE_{mnp} modes:

$$E_x(x, y, z) = \frac{j\omega\mu}{h^2} \left(\frac{n\pi}{b} \right) H_0 \cos\left(\frac{m\pi}{a} x \right) \sin\left(\frac{n\pi}{b} y \right) \sin\left(\frac{p\pi}{d} z \right) \quad (\text{C.20})$$

$$E_y(x, y, z) = -\frac{j\omega\mu}{h^2} \left(\frac{m\pi}{a} \right) H_0 \sin\left(\frac{m\pi}{a} x \right) \cos\left(\frac{n\pi}{b} y \right) \sin\left(\frac{p\pi}{d} z \right) \quad (\text{C.21})$$

$$H_x(x, y, z) = -\frac{1}{h^2} \left(\frac{m\pi}{a} \right) \left(\frac{p\pi}{d} \right) H_0 \sin\left(\frac{m\pi}{a} x \right) \cos\left(\frac{n\pi}{b} y \right) \cos\left(\frac{p\pi}{d} z \right) \quad (\text{C.22})$$

$$H_y(x, y, z) = -\frac{1}{h^2} \left(\frac{n\pi}{b} \right) \left(\frac{p\pi}{d} \right) H_0 \cos\left(\frac{m\pi}{a} x \right) \sin\left(\frac{n\pi}{b} y \right) \cos\left(\frac{p\pi}{d} z \right) \quad (\text{C.23})$$

$$H_z(x, y, z) = H_0 \cos\left(\frac{m\pi}{a} x \right) \cos\left(\frac{n\pi}{b} y \right) \sin\left(\frac{p\pi}{d} z \right) \quad (\text{C.24})$$

The value of h^2 is given by C.18. The resonant frequency is defined by the same formula C.19 as for the TM_{mnp} modes.

From the formulas C.13 to C.17 it can be shown, that for the TM_{mnp} modes neither m nor n can be zero, but p can be zero. Then the lowest order TM mode possible will be TM_{110} . From the formulas C.20 to C.24 it can be shown that for the TE_{mnp} modes either m or n (but not both m and n) can be zero, but p cannot be zero. So lowest order TE mode possible will be the TE_{101} or the TE_{011} .

Appendix D

The cylindrical resonant cavity

The TE_{mnl} modes

For the field phasors of the TE_{mnl} modes in the cylindrical resonant cavities we can write [17]:

$$H_r = -A_{mn} \frac{l\pi}{d} \frac{p'_{mn}}{a} J'_m \left(\frac{p'_{mn}r}{a} \right) \cos(m\phi) \cos\left(\frac{l\pi z}{d}\right) \quad (D.36)$$

$$H_\phi = A_{mn} \frac{l\pi}{d} \frac{m}{r} J_m \left(\frac{p'_{mn}r}{a} \right) \sin(m\phi) \cos\left(\frac{l\pi z}{d}\right) \quad (D.37)$$

$$H_z = -A_{mn} \left(\frac{p'_{mn}}{a} \right)^2 J_m \left(\frac{p'_{mn}r}{a} \right) \cos(m\phi) \sin\left(\frac{l\pi z}{d}\right) \quad (D.38)$$

$$E_r = -j\mu\omega A_{mn} \frac{m}{r} J_m \left(\frac{p'_{mn}r}{a} \right) \sin(m\phi) \cos\left(\frac{l\pi z}{d}\right) \quad (D.39)$$

$$E_\phi = -j\mu\omega A_{mn} \frac{p'_{mn}}{a} J'_m \left(\frac{p'_{mn}r}{a} \right) \cos(m\phi) \sin\left(\frac{l\pi z}{d}\right) \quad (D.40)$$

$$E_z = 0 \quad (D.41)$$

Where, the A_{mn} is excitation constant for TE_{mn} mode. The propagation constant for the TE_{mn} mode is

$$\beta_{mn} = \sqrt{k^2 - \left(\frac{p'_{mn}}{a} \right)^2} \quad (D.42)$$

The $J_m(x)$ is the Bessel function of the first kind of the m -th order. $J'_m(x)$ is the first derivative of $J_m(x)$ with respect to its argument x . Values of the coefficients p'_{mn} for the TE_{mn} modes and the coefficients p_{mn} for the TM_{mn} modes are given in the table D.1.

m	p'_{m1}	p'_{m2}	p'_{m3}
0	3.832	7.016	10.174
1	1.841	5.331	8.536
2	3.054	6.706	9.970

m	p_{m1}	p_{m2}	p_{m3}
0	2.405	5.520	8.654
1	3.382	7.016	10.174
2	5.135	8.417	11.620

Table D.1: Roots of Bessel functions J'_m (left) and J_m (right)

The resonant frequency of the TE_{mnl} mode in the cylindric cavity is:

$$f_{mnl} = \frac{c}{2\pi\sqrt{\mu_r\epsilon_r}} \sqrt{\left(\frac{p'_{mn}}{a}\right)^2 + \left(\frac{l\pi}{d}\right)^2} \quad (D.43)$$

It can be shown that for the TE_{mnl} modes m might have a value of 0, 1, 2... (order of the Bessel function), n might have a value of 1, 2, 3... (roots of the Bessel functions). For the TE modes, l cannot be a zero. Then the lowest possible TE mode will have an indices 011, but the lowest cutoff frequency belongs to the TE_{111} mode. A mode chart for a circular cylindrical cavity is given at figure D.8.

The TM_{mnl} modes

Continuing from [15], phasors of the field components of the TM_{mnl} modes in the cylindrical resonant cavities are:

$$H_r = j\omega\epsilon B_{mn} \frac{m}{r} J'_m\left(\frac{p_{mn}r}{a}\right) \sin(m\phi) \cos\left(\frac{l\pi z}{d}\right) \quad (D.44)$$

$$H_\phi = -j\omega\epsilon B_{mn} \left(\frac{p_{mn}}{a}\right) J'_m\left(\frac{p_{mn}r}{a}\right) \cos(m\phi) \cos\left(\frac{l\pi z}{d}\right) \quad (D.45)$$

$$E_r = -B_{mn} \frac{l\pi}{d} \left(\frac{p_{mn}}{a}\right) J'_m\left(\frac{p_{mn}r}{a}\right) \cos(m\phi) \sin\left(\frac{l\pi z}{d}\right) \quad (D.46)$$

$$E_\phi = B_{mn} \frac{l\pi}{d} \frac{m}{r} J_m\left(\frac{p_{mn}r}{a}\right) \sin(m\phi) \sin\left(\frac{l\pi z}{d}\right) \quad (D.47)$$

$$E_z = B_{mn} \left(\frac{p_{mn}}{a}\right)^2 J_m\left(\frac{p_{mn}r}{a}\right) \cos(m\phi) \cos\left(\frac{l\pi z}{d}\right) \quad (D.48)$$

Where, the B_{mn} is excitation constant for TM_{mn} mode. The propagation constant for the TM_{mn} mode is

$$\beta_{mn} = \sqrt{k^2 - \left(\frac{p_{mn}}{a}\right)^2} \quad (D.49)$$

The resonant frequency of the TM_{mnl} mode in the cylindric cavity is:

$$f_{mnl} = \frac{c}{2\pi\sqrt{\mu_r\epsilon_r}} \sqrt{\left(\frac{p_{mn}}{a}\right)^2 + \left(\frac{l\pi}{d}\right)^2} \quad (D.50)$$

For the TM_{mnl} modes m might have the values 0, 1, 2... (order of the Bessel function), n might be 1, 2, 3... (roots of the Bessel functions). In contrast to the TE modes, l can be a zero. The lowest possible TM mode will be then TM_{010} (see the mode chart Fig. D.1).

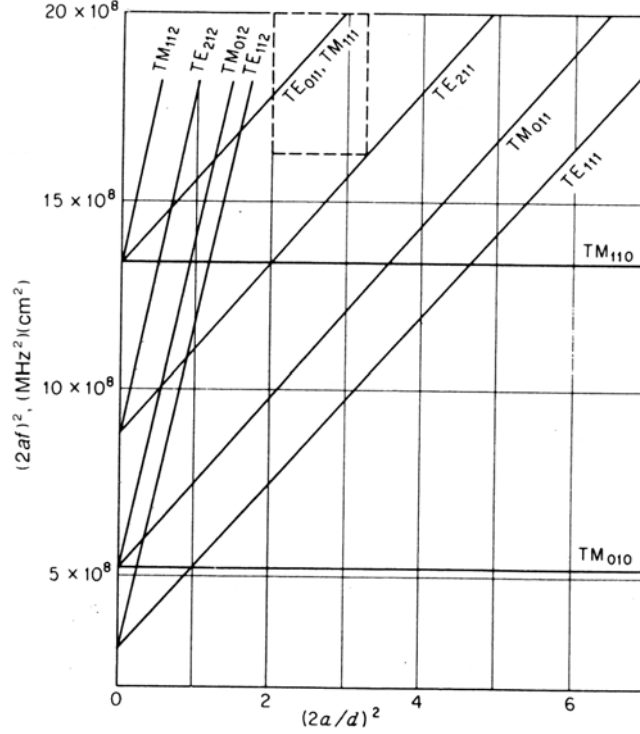


Fig. D.1: Mode chart of a circular cylindrical cavity (courtesy of [13])

The TM_{010} mode has very favorable properties for the particle acceleration purposes. Consequently in accelerators this mode is nearly exclusively used. In a pure pill-box cavity, there are only two field components of the TM_{010} mode inside the cavity:

$$E_z = E_0 J_0 \left(\frac{2.405}{a} r \right) \quad (\text{D.51})$$

$$H_\phi = -j \frac{E_0}{Z_0} J_1 \left(\frac{2.405}{a} r \right) \quad (\text{D.52})$$

A cavity with rounded shape has an E_r component in the TM_{010} like mode. Since mode number $l=0$, the resonant frequency given by D.50 is independent of the longitudinal dimensions of the resonant cavity. It is not possible to tune such a cylindrical resonator by changing its length. A cavity operating with the TM_{010} mode can be tuned by introducing an obstacle into the cavity (small conductive or dielectric entity).

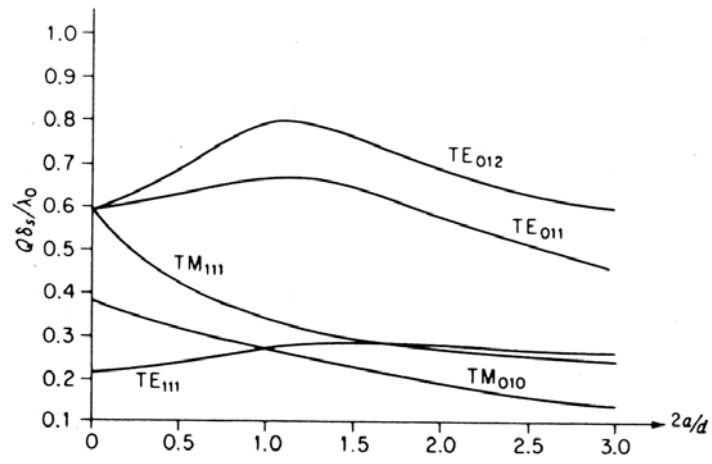


Fig. D.2: Q for circular cylindrical cavity modes (courtesy of [13])

Appendix E

Photos of the phase-shifter that has been built

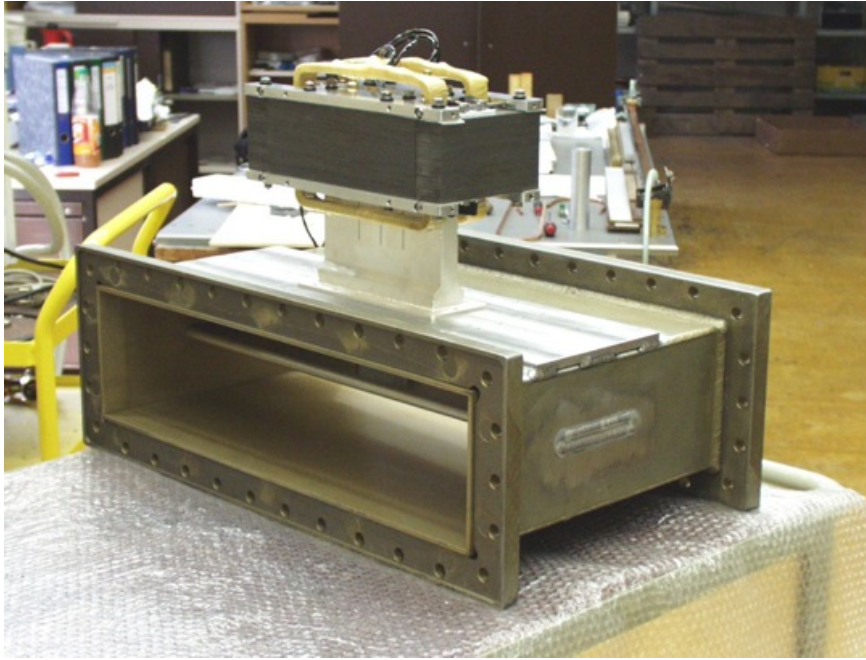


Fig. E.1: The phase-shifter mounted to the strip-line to waveguide transition

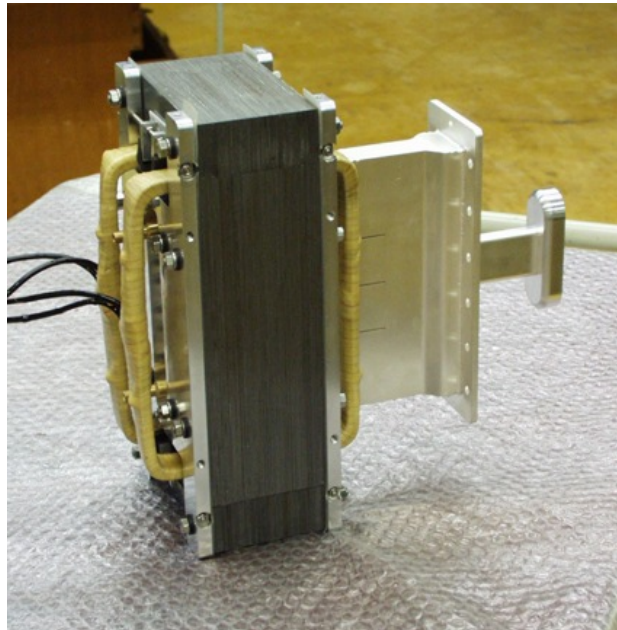


Fig. E.2: The phase shifter strip-line structure with the magnetic circuit

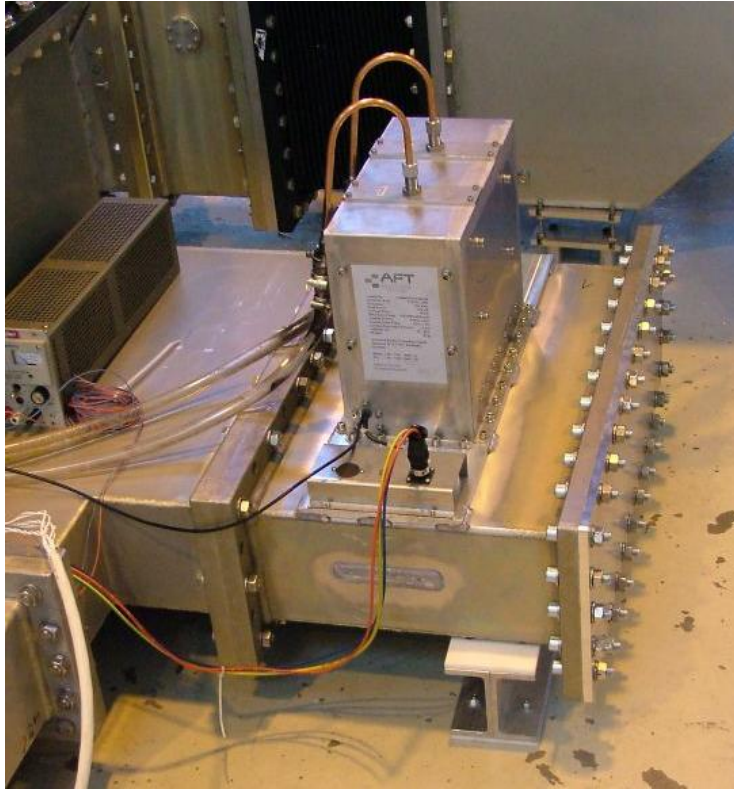


Fig. E.3: Completely assembled phase-shifter connected to the Magic Tee, including the water cooling system, arc detectors and all necessary cabling

Appendix F

Photos of the phase and power modulator that has been built

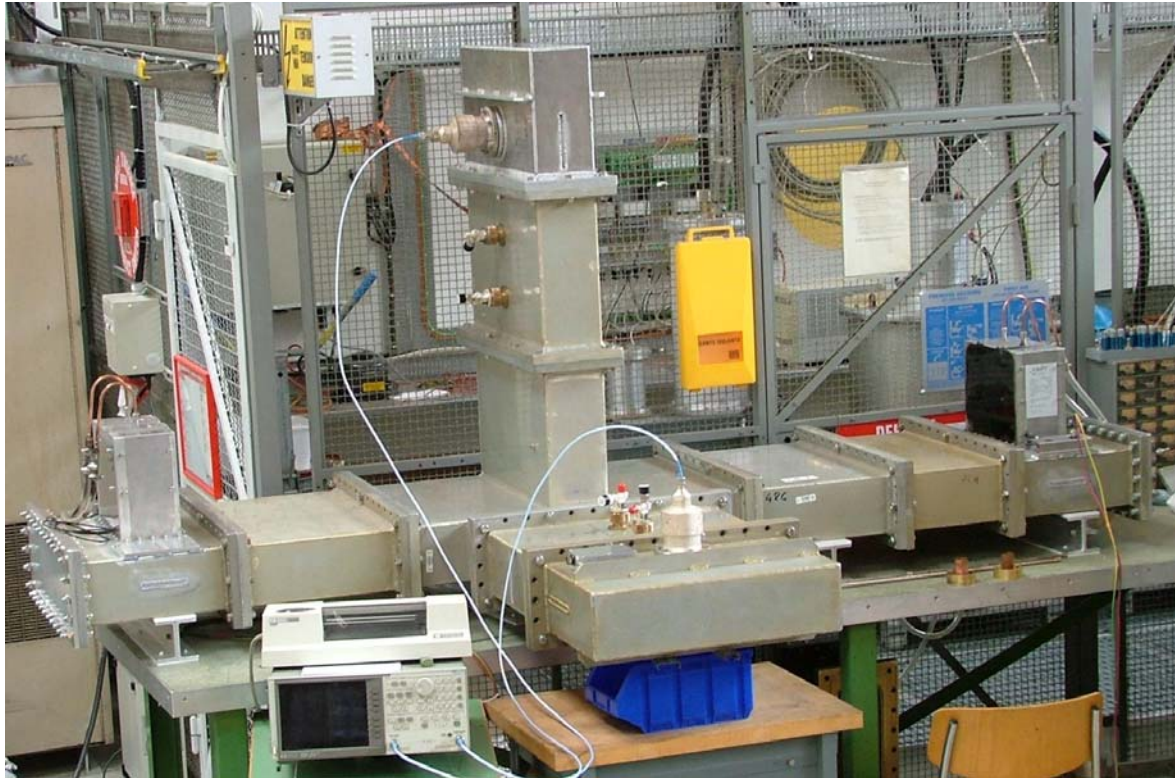


Fig. F.1: Low level tests of the fully assembled phase and power modulator from Fig. 6.13

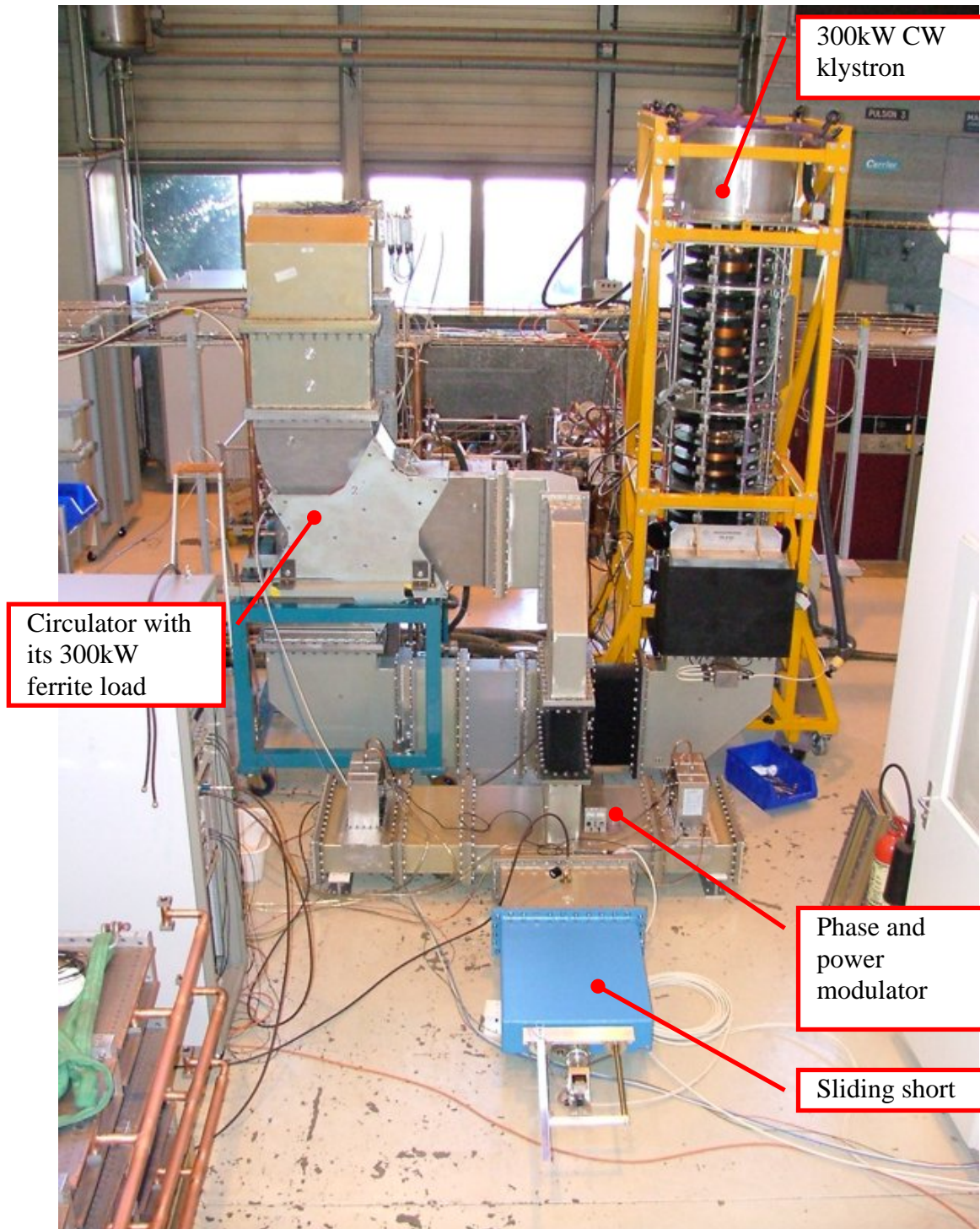


Fig. F.2: High power tests of the modulator, using 300kW/400MHz LHC klystron and a sliding waveguide short circuit as a load.

Appendix G

Measured transmission controlling capabilities

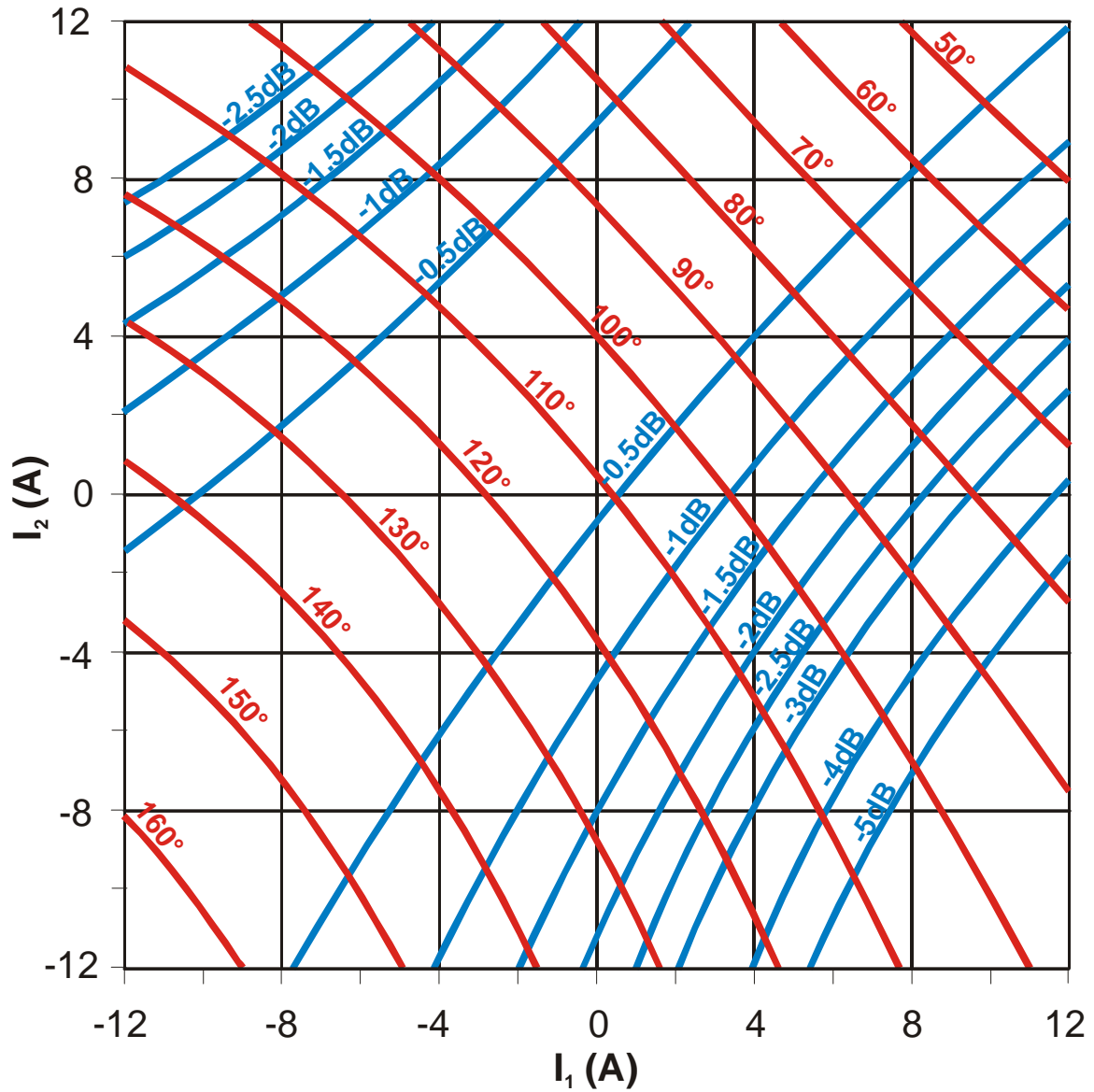


Fig. G.1: Measured transmission controlling capabilities